EXTRACELLULAR VESICLES AS THERAPEUTIC DELIVERY VECTORS FOR NEUROLOGICAL DISORDERS

by

BRIAN JOSEPH JURGIELEWICZ

(Under the Direction of Steven Stice and Yao Yao)

ABSTRACT

Extracellular vesicles (EVs) are nanosized (40-1,000nm in diameter) lipid bound vesicles released from most cell types responsible for delivery of functional biologic material to mediate intercellular communication. Physiologically, EVs deliver cargo including RNA, DNA, proteins, and lipids that can functionally modulate recipient cells. Due to their innate characteristics, EV research is a burgeoning field, as therapeutics and delivery vectors of exogenous biomolecules including small interfering RNA, antisense oligonucleotides, and stapled peptides have shown immense promise. EVs possess advantages including low immunogenicity, low toxicity, increased bioavailability, and ability to cross physiological barriers. However, there is limited understanding of EV uptake kinetics and specificity, which may slow therapeutic development. We optimized an imaging flow cytometry platform to assess dose, time, and recipient cell specificity effects on EV internalization. We found that EV uptake is dose and time dependent and that EVs exhibit an inherent specificity to cells of similar origin. To advance the utility of EVs, a novel therapeutic peptide to decrease dopaminergic cell death in Parkinson's Disease was loaded into EVs via a passive and scalable technique. Herein, EVs can be efficiently loaded with peptides to enhance the peptide uptake kinetics which enabled a more efficient inhibition of the

death pathway in Parkinson's Disease. Lastly, a highly translational porcine stroke model was characterized by identifying lesion topology and assessing its effect on functional outcome post stroke. We found that lesion location impacted stroke recovery as it highly correlated with acute functional outcome. The characterization of lesion topology will advance the understanding of EV therapeutics in the porcine stroke model as a novel mechanism to assess EV biodistribution and function as an alternative biomarker to lesion volume. Together, these studies quantified EV uptake kinetics and specificity, showed that EVs can be harnessed to load with and deliver synthetic peptides, and characterized a translational porcine stroke model to advance the translational potential of extracellular vesicles.

INDEX WORDS: Extracellular vesicles, drug delivery, imaging flow cytometry, Parkinson's Disease, Ischemic Stroke

EXTRACELLULAR VESICLES AS THERAPEUTIC DELIVERY VECTORS FOR NEUROLOGICAL DISORDERS

by

BRIAN JOSEPH JURGIELEWICZ

B.S., Cornell University, 2015

M.S., University of Georgia, 2017

A Dissertation Submitted to the Graduate Faculty of The University of Georgia in Partial Fulfillment of the Requirements for the Degree

DOCTOR OF PHILOSOPHY

ATHENS, GEORGIA

2021

EXTRACELLULAR VESICLES AS THERAPEUTIC DELIVERY VECTORS FOR NEUROLOGICAL DISORDERS

by

BRIAN JOSEPH JURGIELEWICZ

Major Professor:	Steven Stice
	Yao Yao
Committee:	Jarrod Call
	Franklin West

Electronic Version Approved:

Ron Walcott
Vice Provost for Graduate Education and Dean of the Graduate School
The University of Georgia
May 2021

DEDICATION

To my fiancé, Chelsey Green, for your unwavering love and support.

ACKNOWLEDGEMENTS

I would like to thank my major professor, Steven Stice for providing me with the opportunity to work on the amazing projects that I have participated in throughout my time at the University of Georgia. Steve has been a role model beyond the lab bench and has always supported me to expand my interests, network, and understanding of the biotechnology industry. I would also like to thank my co-major professor Yao Yao for being the most supportive and calming mentor for me, no matter if writing for days on end or facing new challenges in the lab, Yao always kept me on track with positive support. I would like to extend my thanks to my committee members, Jarrod Call and Franklin West for offering their time and insights whenever necessary. Thank you to Frank for all of the life experiences working with the pig model!

This dissertation is more than an extension of my own work, but evidence of the collaborative nature of the Regenerative Bioscience Center. Firstly, thank you to all of the current and past Stice and Yao Lab members for your various expertise. Specifically, I would like to thank Ty Maughon for always bringing some laughter with a good story or two into our office on any given day. Outside of our lab, I could not have done it without the help and teamwork from members of the West Lab, notably Kelly Scheulin. Kelly has been a great friend and collaborator during the study and throughout the writing process. Lastly, a special thanks to Hardy Rideout and Eileen Kennedy lab for a great collaborative effort of developing therapeutics for Parkinson's Disease. I am confident the study will continue forward for the betterment of patients.

I am deeply grateful for the never ending support, inspiration, and love from my parents, my brothers, and all other family members. I appreciate all of your questions, but most importantly, the ultimate question, “When are you going to be graduating?” I owe immense appreciation to Thomas Hallowell for taking the time to edit, read, and provide honest feedback about my dissertation. I would also like to thank Pierre Naufal for being a great tennis partner, friend, and voice reminding me to not rush through my PhD and enjoy the process. Lastly, I absolutely have the most utmost gratitude for the love, support, patience, and understanding from Chelsey Green. I could not have gotten through my MS and my PhD without everything you have done for me and I am excited to see where life brings us in the future.

TABLE OF CONTENTS

Page

LIST OF TABLES

Page

LIST OF FIGURES

Page

CHAPTER 1

INTRODUCTION AND LITERATURE REVIEW[1]

[1] Brian J. Jurgielewicz, Yao, Yao, Steven L. Stice. Extracellular Vesicles: Loading and Delivery of Nucleic Acid Therapies. To be submitted in Nanomedicine.

1.1 ABSTRACT

Extracellular vesicles (EVs), endogenous nanocarriers of proteins, lipids, and genetic material, have been harnessed as intrinsic delivery vectors for nucleic acid therapies. EVs are nanosized lipid bilayer bound vesicles released from most cell types responsible for delivery of functional biologic material to mediate intercellular communication and to modulate recipient cells. Due to their innate biological role and composition, EVs possess several advantages as delivery vectors for nucleic acid based therapies including low immunogenicity, low toxicity, increased bioavailability, and ability to be engineered to enhance targeting. In this review, the current understanding of the biological role of EVs as well as the advancements in harnessing EVs to load and deliver nucleic acid therapies are summarized. We discuss the current methods and associated challenges in loading EVs and the future prospects of utilizing the inherent characteristics of EVs as a delivery vector of nucleic acid therapies for genetic based diseases.

1.2 INTRODUCTION

Nucleic acid based therapeutics including small interfering RNA (siRNA), microRNA (miRNA), and antisense oligonucleotides (ASOs) are promising disease altering modalities because they target disease causing genes in a sequence specific manner. The specificity of these therapies allows for targeted approach for treatment of various diseases including hereditary amyloidogenic transthyretin amyloidosis, spinal muscular atrophy, Duchenne's Muscular Dystrophy Disease, amyotrophic lateral sclerosis among others [1,2]. By introducing a nucleic acid modality to the targeted cells, gene expression can be downregulated, augmented or corrected via siRNA, miRNA or inhibitory ASOs, plasmid DNA, mRNA, small activating RNA, splicing modulatory ASOs, and CRISPR sgRNA [1–3]. However, nucleic acid based therapies are severely limited due to inefficient biodistribution and susceptibility to breakdown creating a need for the

development of safe and efficient delivery vectors [4–8]. In this review we will focus solely on EV mediated delivery of siRNA, ASO, and miRNAs, but the common tenants of delivery remain accurate other gene therapy and small molecule modalities (See more in [9–13]).

The natural defense mechanism, RNA interference (RNAi), specifically siRNA and miRNA, knocks down target gene expression by binding to specific mRNA for 1) degradation or 2) repression [1–3,14,15]. siRNAs, 21-23 base pair double stranded oligonucleotides, bind to target mRNA via Watson and Crick pairings and guide the Argonaute 2 protein responsible for mRNA cleavage and inhibition of translation [16,17]. Similarly, microRNAs are small non-coding RNAs around 19-25 nucleotides in length derived from short stem-loop RNAs. Physiologically, miRNAs interact with the 3'UTR of target mRNAs and suppress expression by induction of translation repression and mRNA deadenylation or decapping [1,3,18,19]. In a non-RNAi dependent pathway, antisense oligonucleotides, act on target mRNA by three major distinct mechanisms, 1) altering splicing 2) target degradation 3) translational arrest [8,15,20–22]. ASOs are synthetic single stranded 'DNA-like' oligonucleotides ranging between 8-50 base pairs that bind to specific RNA sequences [20]. ASOs can be synthesized to skip or include an exon by targeting specific 5' or 3' splice junction and exonic/intronic splicing enhancer/silencer sites [23]. This technique can restore mRNA reading frames, promote inclusion of skipped exons, or introduce an out-of-frame deletion [8,24]. Secondly, target degradation occurs by the recruitment of RNase H, a ubiquitous enzyme that identifies DNA: RNA hybrid complexes and cleaves the RNA [25]. (For a more detailed overview please refer to [8,26]. (See Table 1.1)

Nucleic acid therapies are limited by systemic instability and poor delivery to targeted cells [5,6,8]. Thus, due to their innate biological roles in intercellular communication, EVs have been engineered as delivery vectors. In the preclinical setting, EVs have been employed to

deliver siRNA, miRNA, and ASOs to targeted disease inducing genes including BACE1 for Alzheimer's, HTT for Huntington's Disease, and various oncogenic targets [27–30]. Despite this, there remains a divergence between preclinical and clinical success in utilizing EVs as a delivery vector. Here, we aim to provide a comprehensive overview on the current utilization of exosomes as nucleic acid vectors. In this review, we

1) Examine the current delivery strategies of gene therapies

2) Discuss the biological framework of extracellular vesicles

3) Assess the loading procedures of gene therapies into or onto exosomes

4) Consider the current opportunities and future potential of exosome based gene therapy delivery.

1.3 CURRENT DELIVERY STRATEGIES OF NUCLEIC ACID THERAPIES

An efficient and safe delivery system is integral to the development and large scale utility of siRNAs, ASOs, and miRNAs. After systematic administration and entry into circulation, endonucleases or exonucleases degrade nucleic acids into fragments preventing the accumulation of the therapeutic in the intended tissue [1,5]. An ideal vector must be safe with low toxicity and immunogenicity, protect the therapeutic cargo from external breakdown, and to successfully target the specific tissue or cell population of interests [5,19,31]. Specifically, for systemic administration of siRNAs, ASOs, and miRNAs, an optimal delivery vehicle must provide stability against serum nucleases, evade the immune system, prevent immediate renal clearance, exit the vasculature, enter the correct target cells, and lastly escape the endolysosomal system [1,2,32,33]. Commonly used delivery approaches can be classified into two categories 1) modification of the gene therapy itself or 2) use of a delivery vector [1].

1.3.1 CHEMICAL MODIFICATIONS OF NUCLEIC ACIDS

Several chemical modifications have advanced systemic utility of nucleic acids to improve stability, decrease immunoreactivity, increase concentration, and increase cellular uptake. The most common modifications include a substitution of the 2′-OH with a 2′-O-methyl (2′-OMe)27 or 2′-methoxyethyl (2′-MOE) group or the substitution of certain nucleotides with locked nucleic acid (LNA), unlocked nucleic acid (UNA) or glycol nucleic acid (GNA) [4,34]. The backbone is typically engineered as a Phosphorothioate (PS) backbone, which improves stability in circulation and enhances binding to blood proteins to decrease renal clearance [35,36]. Several disadvantages include significant toxicities associated with the protein binding capabilities of PS oligonucleotides [37]. Similarly, conjugation with small molecules like cholesterol, peptides, polymers and others has shown early delivery enhancement, *in vivo*. Conjugation to cholesterol or alpha-tocopherol changes the hydrophobicity and thus solubility of the molecule, but may alter the RNA functionality [38]. Cell penetrating peptides, 30 amino acid chains of arginine and lysine, have been tagged to siRNA and ASOs [33]. CPPs have high efficacy on anionic cell membranes and potential lysosome escape with an additional hemagglutinin molecule. However, CPPs do elevate cytotoxicity and immunogenicity and the cargo may disrupt the CPP efficacy [33,39]. Other advanced conjugate systems include dynamic polyconjugates and GalNac conjugates are promising for delivery but limited to liver localization [40]. Overall, these modifications provide advancements in therapeutic utility, but challenges hinder wide range applications making delivery vectors a more viable option. For further review of chemical modifications refer to [41–43].

1.3.2 VIRAL VECTORS

Viral vectors, specifically adeno-associated vectors are a non-enveloped virus that can be engineered to deliver nucleic acids to target cells [44]. Viral vector advantages include their relatively high efficiency of gene transfer, vector tropism to targeted tissue, and ability to provide long term therapy when applicable [19,31]. Nucleotide therapeutics have been inserted into the backbone of the viral vectors targeting SOD1 ALS, spinocerebellar ataxia, and tumor oncogenes [45,46]. However, viral vectors often have high immunogenicity and develop resistance due to the high probability of encountering pre-existing immunity in humans [19,31]. Other necessary precautions using viral based methods include analyses of repeated dosing, tolerability, long-term expression, efficacy, the ability to regulate expression, and off target effects [19,31]. For further review of viral vector refer to [44,47,48]**.**

1.3.3 NANOPARTICLES

Nanoparticles, both synthetic or lipid based (liposomes), have been the most commonly used non-viral delivery vector for siRNA, and most recently mRNA vaccines, based on their manufacturing scalability, small size, shape, engineered for targeting or enhanced circulation time, and ability to protect entrapped nucleotides [6,49,50]. Most of the lipid-based particles, liposomes, include a cationic or ionizable lipid to enhance RNA entrapment, but the positive net charge may lead to increased toxicity [51,52]. Liposomes may activate complement through the absorption of opsonins and coagulation factors which ultimately leads to phagocytosis, cell stress, inflammation, and apoptosis [51]. Often, a PEG molecule is lipid anchored to increase nanoparticle half-life *in vivo*, reduce particle size, prevent aggregation during storage, and reduce uptake by unintended targets such as red blood cells and macrophages [51,53]. However, PEGylation reduces cellular uptake and silencing efficacy of the siRNA by sterically blocking liposome and endosomal membrane interaction [53,54]. Overall, current delivery modifications and

vectors have limitations, and further advancements are necessary for efficient systemic administration of nucleotide therapies. For further view of nanoparticles [51,52].

1.4 EVs: NATURAL DELIVERY VECTORS OF NUCLEIC ACIDS

Extracellular vesicles are a heterogenous class including three major subtypes, apoptotic bodies (50nm-5,000nm), microvesicles (100nm to 1μm) and exosomes (50nm-150nm) differentiated by size, content and mechanism of formation [55–58]. Due to the heterogeneity of EVs and the expanding utility as therapeutics and delivery vectors, we will use the term EVs as an encompassing characterization for the use of exosomes as delivery vectors [59]. During EV biogenesis, EVs are loaded with functional genetic components including DNA, RNA, and proteins that modulate the phenotypes of recipient cell lines [58,60]. Not only are EVs natural communicators and suitable for delivery, EVs have been sourced from various cell lines including neural stem cells, mesenchymal stromal cells, dendritic cells, and others as acellular therapeutics for diseases like stroke, myocardial infarction, and others [30,61–64].

1.4.1 INHERENT LOADING OF GENETIC MATERIAL

The biogenesis of EVs, specifically exosomes (Figure 1), is initiated by the formation of endocytic vesicles from the inward budding of plasma membrane. This process is followed by subsequent inward budding of the early endosome and acidification of the endosome resulting in multivesicular bodies (MVBs) containing intraluminal vesicles [65–67]. There are two main pathways that form multivesicular bodies and internalized intraluminal vesicles, endosomal sorting complex required for transport (ESCRT) dependent and independent [68,69]. Upon the maturation of the multivesicular body, the ILVs are shuttled to the plasma membrane and released into the extracellular environment—at which point they are termed exosomes [65].

During the EV biogenesis process, cellular machinery packages nucleic acids, specifically, RNA into the lumen of EVs for intercellular delivery[68]. RNA are highly enriched into EVs due to their small size, high abundance, ability to associate with membranes and cytoplasmic location [58]. Initial studies have shown that EVs contained mRNAs, miRNAs, small nuclear RNAs, tRNAs, and others, with a peak size of 200 nucleotides and extending out to 5kb or more [58]. Several mechanisms have been connected with RNA packaging including RNA sequence motifs, secondary configuration, differential affinity for membrane lipids and association with RNA binding proteins including ALIX, annexin A2, major vault protein MVP and others [58,70]. Similarly, other sorting motifs include RNA or RBP modifications including ubiquitylation, sumoylation, phosphorylation and uridylation [71]. It is evident that several mechanisms play a role in the complex process of cargo loading into EVs and further understanding the endogenous system may provide insights into loading EVs with therapeutics.

1.4.2 NATURAL MEMBRANE PROTECTION AND TROPISM

The EV lipid bilayer protects nucleic acid cargo from serum nuclease degradation, similar to nanoparticle delivery [60]. Evidence of EV protection was apparent when EVs have been administered into harsh *in vitro* environments with nucleases, proteases, and various proteolytic enzymes or into circulation and cargo remained functional [28]. The EV membrane resembles the parent cell with a similar lipid profile, integrins, and adhesion proteins that may influence target cell uptake [72,73] which determines possible interaction with similar cells to parent cell, where for instance, a HEK293T EV is internalized by HEK293T cells [74]. Mesenchymal cell derived EVs have enhanced retention compared to liposomes, in the circulation of mice due to CD47-mediated protection, ‘don't eat me’ signal, against phagocytic cells [75]. Alike nanoparticles, EVs may get trapped in the liver and kidney, but targeting can be enhanced through EV surface

modification [76]. For instance, RVG peptides have been engineered onto a common EV marker, Lamp2B to enhance targeting to neurons [30,77]. Other groups have used similar techniques to target specific tumors and cancer cells [29,73]. EVs have natural protective and targeting capacity making them an ideal vector to protect nucleic acids in the extracellular space.

1.4.3 ABILITY TO CROSS PHYSICAL BARRIERS

The appeal of harnessing EVs as gene therapy delivery systems stems from their inherent ability to transfer functional biological molecules from cell to cell. Physical barriers including 1) tissue, 2) cellular, and 3) intracellular barriers impede conventional delivery systems. Although the blood brain barrier, monolayer of tightly joined endothelial cells, is impermeable to over 98% of small molecules, EVs traverse the BBB via a transcytosis mechanism of the neurovascular cell types [11,30,78–81]. The majority of EV uptake in recipient cells occurs via an active endocytosis mechanisms, thus allowing EVs to shuttle cargo past the plasma membrane [82–84]. Notably, EVs can be internalized by cells in as little as 30 minutes [74], without surface aggregation, whereas in a head to head comparison of loaded synthetic nanoparticles have 1.7 times lower uptake and aggregate on the surface [85]. Though uptake occurs via endocytosis, EVs were shown to bind with the endosome and release their active cargo into the cytoplasm prior to transcytosis (recycling into extracellular milieu), or degradation by the lysosome [86]. These recent studies indicate that EVs are natural protective and delivery vectors of endogenous genetic cargo making them an alluring alternative to synthetic vectors.

1.4.4. LOW IMMUNOGENICITY AND TOXICITY PROFILE

While demonstrating efficacy to deliver therapeutic payloads, EVs have also been assessed for safety. In contrast to most conventional delivery vectors, EVs have low immunogenicity and toxicity due to their natural characteristics [28,75,87,88]. In a comprehensive

cross species study, HEK293T EVs dose response safety and toxicity were assessed in C57BL/6 mice, showing minimal immune responses and no signs of toxicity [89]. Since EVs are sourced from various cell types, other groups have shown that tumor derived "microparticles" were feasible and safe [90]. Even at high doses, there were no detected signs of hepatotoxicity or loss of function [91]. Importantly, EVs have been repeatedly dosed in pre-clinical models with no reported signs of rejection after an initial dose [30,61,89]. Essentially, EVs have been sourced from various cell types and all support the encouraging safety profile.

1.4.5 SYNERGISTIC THERAPEUTIC BENEFITS

Despite the immense potential of EVs as delivery vectors, it is important to acknowledge that EVs sourced from various therapeutic cells specifically stem (and progenitor) cells have innate therapeutic capacity for a multitude of diseases. EVs have been isolated from neural stem cells (NSCEVs) and mesenchymal stem/stromal cells (MSCEVs), demonstrating the therapeutic potential of their parent cell lines, anti-inflammatory properties and enrichment of specific miRNAs [92]. NSCEVs have been shown to improve tissue and functional recovery in both a mouse and porcine ischemic stroke model [61,62]. Similarly, cardiosphere and MSC derived EVs have moderating stroke induced neurodegeneration, inflammation, and neurological deficits [93–95]. Other targeted areas with early efficacy of EVs as acellular therapeutics include myocardial infarction [96,97], utilization in cancer vaccines [98], and immune disorders [99]. Thus, depending on the EV source for delivery utility, researchers can capitalize on the synergistic ability of delivery.

1.5 TECHNIQUES FOR LOADING EVS

EVs provide an immense potential as delivery vectors but loading nucleic acids into EVs is not an easy task. Loading of nucleic acids into EVs can be subdivided into two main categories 1) Pre-Isolation and 2) Post-isolation (Table 1.2). As a relatively nascent field, there are advantages

and disadvantages to each method that must be accounted for depending on the therapeutic indication.

1.5.1 PRE-ISOLATION LOADING METHODS

Loading prior to isolating EVs, often referred to as endogenous loading, hijacks inherent EV loading machinery and processes. Whether it be overexpression via chemical transfection of the exogenous cargo or harnessing the RNA loading machinery of EV donor cells, the therapeutic RNA is loaded into EVs through its intrinsic mechanisms.

Over expression of Exogenous Nucleic Acids

Overexpression a nucleic acid of interest has been commonly used to load therapeutic miRNA into EVs. Briefly, the parent cells are chemically transfected with commercial transfection agents to increase the amount of cytosolic miRNA that may get into EVs prior to being released from these cells [29]. In the parent cell, free floating miRNA are non-selectively engulfed by the invagination of the multivesicular bodies along with the other genetic contents [58,100]. Several proof of principle studies have overexpress miRNA or mRNA in hMSC lines, CD34+ stem cells, U87 Glioblastoma cells, T-regulatory cells, and HEK293T cells (Table 1.2) to treat Huntington's Disease, Schwann Cell Cancers, breast cancers, and other indications [29,101,102]. For instance, MSC EVs loaded with miR-146 decreased targeted EGFR and NFK-B protein levels in a mouse tumor model along with miR-124 delivery to promote neuroprotection after a brain infarct [103]. Using similar methods, siRNA was transfected into mouse fibroblasts resulting in suppression of tumor growth in mice [104].

There was encouraging early evidence in delivering miRNA and siRNA: however, several challenges remain, specifically potential contamination of transfection agents. Not only is possible contamination an issue, but the overexpression model is not applicable to miRNAs that

are detrimental to the donor cell thereby inhibited proliferation, homeostasis, or general EV biogenesis [88]. Further, overexpression of miRNA loading efficiencies may relatively variable depending on the treatment conditions and state of the parent cell, but many studies lack quantifiable metrics of loading efficiencies [104,105]. Due to these challenges, there have been advancements in engineering the cargoes to hijack the loading machinery for therapeutic proteins [69].

Recently, an alternative method was adopted to produce therapeutic mRNA loaded in EVs derived from various cell lines. Using a cellular nanoporation method, plasmid DNA was transfected into donor cells and the secreted EVs then contained therapeutic mRNA. This novel technique resulted in a significant increase of specific mRNA transcripts in the EVs which in turn inhibited tumor growth and increase survival in a glioma murine model [106]. Nanoporation may be an alternative to chemical transfection, but more studies need to be done to support its reproducibility and efficacy. The authors claimed that cellular nanoporation produced up to 50-fold more exosomes and a greater than 10^3 fold increase in exosomal mRNA transcripts compared to bulk electroporation [106]. Though this study has been done in mRNA, the fundamentals should be translatable to and explored in other therapeutic modalities.

Engineering Cargo to Enhance Loading Selectivity

To enhance loading of EVs prior to isolation, the natural loading machinery in the donor cell has been exploited. 'Designer exosomes' were created by binding L7Ae, a ribosomal protein to CD63 to hijack delivery into CD63 expressing EVs. From there, therapeutic mRNA was co-expressed in the producer cell which binds to the L7Ae protein and subsequently delivered into EVs for downstream therapeutic applications [107]. Similarly, Lamp2B, a common exosomal protein was tagged with the MS2 bacteriophage coat protein dimer, a well characterized RNA

binding protein, to enhance EV mRNA loading in HEK293FT cells [108]. This platform resulted in a 6-fold increase of RNA compared to cells without MS2 revealing that loading of RNA up to 1.5KB is feasible. However, when loaded EVs were internalized by recipient cells, the RNA was inactive [108]. Further to enhance miRNA loading, pre-miR199a attached to Lamp2A, with a modified TAR RNA loop to exploit the TAT peptide/HIV-1 transactivation response (TAR) RNA interacting peptide. This motif resulted in a 65-fold enrichment of the miR-199a-3p in the EVs compared to cells without the TAT construct, but the EV delivered miRNA also remained functionally inactive in recipient cells [109]. Despite these shortcomings in functional efficacy, engineering the parent cells does result in loading of EVs with therapeutic cargo.

1.5.2 POST-ISOLATION LOADING TECHNIQUES

Post-isolation or exogenous loading encompasses a variety of techniques to load nucleic acid therapeutics into extracellular vesicles. As compared to pre-isolation methods, post-isolation permits for a wider array of therapeutics to be loaded without the detriment of altering the parent cell line. Another major advantage of using post-isolation techniques is the wide range of EV producer cells since it is not limited to cell types that are easily transfected or efficient intrinsic cell machinery. Post loading can be standardized and controlled whereas the pre-isolation is EV biogenesis and cell state dependent and may vary [105].

Electroporation

Initially designed to disrupt the cellular membrane for transfection by creating small pores for cargo to enter (or exit) electroporation has been used to load nucleic acids into EVs secreted from murine dendritic cell, HEK293T bovine milk, N2A, red blood cells, among others [28,30,58,110]. Electroporation functions by passing volts throughout the isolated EVs in suspension to form small pores in the lipid bilayer allowing for entry/exit of cargo [111]. Using electroporation,

glyceraldehyde 3-phosphate dehydrogenase, GAPDH and beta-secretase 1, BACE1 siRNA were loaded into engineered dendritic cell-derived EVs and delivered to the brain in a rodent model. This study showed significant dose dependent knockdown of target mRNA and protein, with 25% loading efficiently and can deliver functional siRNA across the blood brain barrier [30]. Similarly, bovine milk EVs electroporated with siRNA targeting VEGF, EGFR, and other cancer biomarkers had low loading efficiency of around 4-5%, but showed anti-proliferative effects *in vitro* and *in vivo* [110]. Another study assessed electroporation in red blood cell EVs, antisense oligonucleotides, Cas9 mRNA, and Plasmid DNA emphasizing the applicability of loading EVs with various modalities [28]. Electroporation resulted in 20-24% of ASO and 18% of Cas9 mRNA loaded into EVs with high functional effects, but with decreased effects when delivering larger plasmid DNA [28]. These studies support the wide applicability of electroporation to load EVs and modulate recipient cells.

Electroporation has fundamental pitfalls in data interpretation, potential decreases in EV integrity, and cargo aggregation [112,113]. Under various conditions of various voltages, concentrations of EV and RNA cargo, and medium, siRNA aggregated [112]. Though this may seem innocuous, aggregation of siRNA can be mistakenly calculated as loaded EVs thereby creating false positive conclusions [112]. Conversely, others have continued to use electroporation and have not reported siRNA aggregation nor disruption of the therapeutic cargo [114]. Electroporation may also result in EV aggregation, but these aggregates can be broken up by pipetting [28]. Though cargo and EV integrity may be hindered, the majority of studies have shown efficacious cargo delivery and functional efficacy in target cells.

Sonication

To generate micropores in the EV membrane, sonication applies sound energy through the EVs and nucleic acids in suspension [115]. HEK293T EVs loaded with siRNA, miRNA, and ssDNA by sonication showed an efficient target knockdown and expression of HER2 for treatment of breast cancer [116]. This study showed sonication efficiently loaded siRNA into EVs at a 325% increase compared to passive loading, preserved the integrity of the cargo, and had significantly lower amount of siRNA aggregation compared to electroporation [116]. When optimizing protocols, sonication did not induce significant EV or siRNA aggregation and resulted in ~12-fold less large aggregates than those induced by electroporation [116]. Importantly, sonicated EVs had higher cellular uptake than electroporated EVs under the same conditions, which further supports the need to assess sonication as an alternative loading mechanism.

Chemical Transfection

Chemical transfection uses an agent to encapsulate the therapeutic cargo or interrupts the EV membrane to deliver cargo through the lipid bilayer membrane. Chemical transfection has shown promise in loading siRNA and miRNA into HeLa, brain endothelial, and macrophage derived EVs [110,117,118]. As proof of principle, HeLa EVs were transfected with siRNA and displayed efficient delivery into recipient cells, but did not report loading efficiency [117]. Similar results supported this notion where EVs loaded with VEGF siRNA for the treatment of glioblastoma increased the cell uptake more than four times compared to siRNA alone *in vitro* and decreased tumor proliferation *in vivo* [119]. In a direct comparison to electroporation, milk EVs were transfected with siRNA resulting in around 30% efficient loading, whereas electroporation resulted in merely 5% efficiency [110]. Similar to transfection f parent cells, the major drawback in using chemical transfection agents is the risk potential contamination in the EV sample, where lipofectamine micelles may be indistinguishable from EVs [117]. There have been reports of the

lipofectamine merging with the EV membrane thus increasing the size of the EVS and potentially altering their uptake potential [120]. With this evidence, groups have harnessed these hybidosome (hybrid liposome/exosomes) to deliver larger cargoes [120]. In summary, transfection provides a viable alternative to sonication and electroporation, but extensive cleanup after loading is required to eliminate the possibility of micelle contamination rather than a homogenous EV sample.

Passive Loading – Co-Incubation

Passive loading does not involve invasive loading methods nor engineering of parent cell line, but rather co-incubation of therapeutic cargo and isolated EVs in a highly scalable manner. siRNA and miRNA have been successfully loaded into various types of EVs via the co-incubation method by altering the siRNA chemistry, but functional efficacy has been varied among studies. An initial study of loading melanoma cell derived 'exosome like vesicles' (ELVs) with cholesterol tagged siRNA resulted in a reported 80% of siRNA associated with EVs equating to 73 molecules of siRNA associate with EVs whereas non-conjugated siRNA had no EV association [121]. However, the loaded siRNA lacked functional effects on gene expression in target cells [121]. Other reports supported the efficient association of cholesterol siRNA to the EVs with increased efficiencies by increasing the siRNA hydrophobicity [27,122]. EV mediated delivery of siRNA targeting the HTT gene had a dose dependent silencing of HTT mRNA and protein and when administered via a bolus intrastriatal injection loaded EVs had bilateral functional knockdown of targeted genes [27]. Compared to previous studies, 10-50% of siRNA added was associated with EVs equating to 1,000-3,000 hsiRNA molecules associated per EV which is significantly greater than previous studies mentioned above [27,122]. In fact, increasing siRNA to EV ratios yielded higher loading efficiencies with saturation kinetics: at a 1:25,000 sEV-to-

hsiRNA ratio which resulted in 24% loading efficiency or between 3-6,000 molecules of siRNA associated with EVs [122]. Additionally, overloading EVs above 3,000 molecules of siRNA decreased functional efficiency [123]. However, the hsiRNA may not be incorporated in the lumen of the EV but rather associated to the surface [27]. In a separate study, CP05, an anchor peptide that binds to CD63, was tagged to an antisense oligonucleotide and mixed with EVs resulting in ASO association with the EV membrane at a binding efficiency of 82.5%. Furthermore, the EV associated CP05 anchored ASO was functionally active in increasing dystrophin in a muscular dystrophy mouse mode [124] which provides another avenue of passive EV loading. Passive loading provides a high-throughput and non-invasive method of loading EVs and further assays need to be done to elucidate the protection capacity of EVs when the therapeutics are associated to the external surface of the EVs.

1.6 EVS IN THE CLINIC

Given the promising results from the preclinical studies, loaded EVs have made it into the clinic. Although when searching ‘exosome’ and ‘extracellular vesicle’ on clinical trials . gov, there are 205 and 73 registered trials respectively, there are few focused on EV delivery.

In a Phase 1/2 study of ischemic stroke currently underway, allogeneic MSC EVs, enriched by miR-124 will be assessed for safety in efficacy in a small population (NCT03384433). Secondly, a trial using MSC-derived EVs loaded with KrasG12 siRNA for the treatment of pancreatic cancer is currently recruiting patients (As of March 4, 2020, NCT03608631). This Phase 1 trial aims to evaluate dosing regiments and safety of loaded MSC EVs for patients with pancreatic cancer with KrasG12D mutation that spread to other places in the body. As the seminal clinical study using EVs as a delivery vector, safety and tolerability will be the main focus, while secondarily pharmacokinetics and disease control rates will also provide valuable insights. The

limited number of clinically grade EVs may be a result of good manufacturing practice challenges including upstream cell cultivation, downstream purification or general quality control during the EV generation and loading processes [125]. However, there is no shortage of EV mediated delivery studies in the preclinical pipeline advancing the translation of EVs into the clinic. For more information on clinical trials see [126]. For more information on clinical trials refer to the International Society of EVs (ISEV) position paper [127].

1.7 CURRENT CHALLENGES AND FUTURE DIRECTIONS

Harnessing EVs as delivery vectors of nucleic acid cargoes, though promising, has areas to improve before widespread translation into the clinic. Overall, there remains a need for a scalable and sustainable source of homogeneous loaded extracellular vesicles.

The field lacks consensus on the best method for obtaining high yields of pure extracellular vesicles [128]. This may be due to relatively low yields of production by mammalian cells, cumbersome isolation methods, and lack of characterization or quantification techniques [129]. Further, an ISEV position paper supports this notion by stating that EV isolation is not standardized which leads to heterogenous samples creating possible confounding artefacts and misleading information in EV loading, scalability, and manufacturing [59,130,131]. Another potential obstacle to overcome is the targeting of EVs to recipient cells, *in vivo.* Though we and others have shown EVs to have inherent tropism to specific cells, EVs when administered intravenously can become trapped in the liver, kidney, and lungs [74,76]. To overcome this challenge, EV membranes have been engineered with targeting modalities including ligands, peptides, and antibodies to enhance organo- and cellular tropism to specific tumors, neurons, and other specific cells [29,30,73]. Further work in engineering EVs can be done to increase its utility across EV and recipient cells of interest.

Although there are a variety of possible techniques to load EVs with nucleic acids, loading efficiency is highly variable and each method has specific flaws as discussed above. In post isolation loading techniques, a major challenge is to separate free nucleic acid from loaded. Commonly the sample mixtures are ultracentrifuged or filtered which may disrupt EV membrane integrity, decrease EV sample yield, and is a low throughput technique [132]. Though efficacious, EV loading efficiency remains low and often variable due to the loading methodology and post sample cleanup [105,133]. In passive loading assays where the therapeutic cargo may merely be associated and not internalized by the EVs, studies need to be done to assess the protective capacity of the EVs. Though cholesterol tagged siRNA remained functional *in vivo*, the intrastriatal injection was devoid of common systemic catalytic enzymes [27]. By optimizing these challenges, increasing the understanding of inherent EV loading, and continuously exploring novel loading techniques, loading efficiency can be increased without corrupting the inherent benefits of EVs. With the early preclinical success, consistent improvement in loading since the initial attempts in the early 2010's, and progress into the clinic, EVs hold immense potential in becoming a next generation class of delivery vectors for therapeutic nucleic acids.

1.8 CONCLUSION

EV-based delivery of nucleic acid gene therapy is a promising approach to delivering new precision medicine treatments for various genetic diseases. Since EVs are natural delivery vectors, they are highly advantageous. EVs advantages include, but not limited to their intrinsic ability to protect nucleic acid cargo, cross physiological barriers including the blood brain barrier, and are highly stable, non-toxic, non-immunogenic with increase circulation retention. These characteristics make them highly suitable for drug delivery purposes as seen in various preclinical models. Though there are a variety of loading mechanisms divided into two

categories, pre and post isolation, loading must continuously be optimized to bridge the translational gap of EVs as delivery vectors. Overall, the nascent field of EV based delivery of nucleic acids has made immense progress and further studies will be required to support the preclinical findings to advance EVs through the clinic.

1.9 REFERENCES

1. Setten, R. L., Rossi, J. J. & Han, S. ping. The current state and future directions of RNAi-based therapeutics. *Nature Reviews Drug Discovery* vol. 18 421–446 (2019).
2. Dammes, N. & Peer, D. Paving the Road for RNA Therapeutics. *Trends in Pharmacological Sciences* vol. 41 755–775 (2020).
3. Bajan, S. & Hutvagner, G. RNA-Based Therapeutics: From Antisense Oligonucleotides to miRNAs. doi:10.3390/cells9010137.
4. Kaczmarek, J. C., Kowalski, P. S. & Anderson, D. G. Advances in the delivery of RNA therapeutics: From concept to clinical reality. *Genome Medicine* vol. 9 (2017).
5. Juliano, R. L. The delivery of therapeutic oligonucleotides. *Nucleic Acids Research* vol. 44 6518–6548 (2016).
6. Tatiparti, K., Sau, S., Kashaw, S. K. & Iyer, A. K. siRNA delivery strategies: A comprehensive review of recent developments. *Nanomaterials* vol. 7 (2017).
7. Xue, H. Y., Liu, S. & Wong, H. L. Nanotoxicity: A key obstacle to clinical translation of sirna-based nanomedicine. *Nanomedicine* vol. 9 295–312 (2014).
8. Gurav, B. & Srinivasan, G. Antisense oligonucleotides as therapeutics and their delivery. *Curr. Sci.* **112**, 490–498 (2017).
9. Johnsen, K. B. *et al.* A comprehensive overview of exosomes as drug delivery vehicles - Endogenous nanocarriers for targeted cancer therapy. *Biochimica et Biophysica Acta* -

Reviews on Cancer vol. 1846 75–87 (2014).

10. Gomari, H., Forouzandeh Moghadam, M. & Soleimani, M. Targeted cancer therapy using engineered exosome as a natural drug delivery vehicle. *Onco. Targets. Ther.* **Volume 11**, 5753–5762 (2018).
11. Zheng, M., Huang, M., Ma, X., Chen, H. & Gao, X. Harnessing Exosomes for the Development of Brain Drug Delivery Systems. *Bioconjugate Chemistry* vol. 30 994–1005 (2019).
12. Lai, R. C., Yeo, R. W. Y., Tan, K. H. & Lim, S. K. Exosomes for drug delivery — a novel application for the mesenchymal stem cell. *Biotechnol. Adv.* **31**, 543–551 (2013).
13. Pinheiro, A. *et al.* Extracellular vesicles: intelligent delivery strategies for therapeutic applications. *Journal of Controlled Release* vol. 289 56–69 (2018).
14. Ahmadzada, T., Reid, G. & McKenzie, D. R. Fundamentals of siRNA and miRNA therapeutics and a review of targeted nanoparticle delivery systems in breast cancer. *Biophysical Reviews* vol. 10 69–86 (2018).
15. Magen, I. & Hornstein, E. Oligonucleotide-based therapy for neurodegenerative diseases. *Brain Res.* **1584**, 116–128 (2014).
16. Wittrup, A. & Lieberman, J. Knocking down disease: a progress report on siRNA therapeutics HHS Public Access. *Nat Rev Genet* **16**, 543–552 (2015).
17. Dana, H. *et al.* Molecular Mechanisms and Biological Functions of siRNA. *Int. J. Biomed. Sci.* **13**, 48–57 (2017).
18. Ge, W. *et al.* Overview of MicroRNA Biogenesis, Mechanisms of Actions, and Circulation. *Front. Endocrinol.* | *www.frontiersin.org* **1**, 402 (2018).
19. Couto, L. B. & High, K. A. Viral vector-mediated RNA interference.

doi:10.1016/j.coph.2010.06.007.

20. Scoles, D. R., Minikel, E. V & Pulst, S. M. Antisense oligonucleotides A primer. *Neurol Genet* **5**, 323 (2019).

21. Sardone, V., Zhou, H., Muntoni, F., Ferlini, A. & Falzarano, M. S. Antisense oligonucleotide-based therapy for neuromuscular disease. *Molecules* **22**, (2017).

22. Bishop, K. M. Progress and promise of antisense oligonucleotide therapeutics for central nervous system diseases. (2017) doi:10.1016/j.neuropharm.2016.12.015.

23. Singh, N. N., Shishimorova, M., Lu, C. C., Gangwani, L. & Singh, R. N. A short antisense oligonucleotide masking a unique intronic motif prevents skipping of a critical exon in spinal muscular atrophy. *RNA Biol.* **6**, 341–350 (2009).

24. Hua, Y. & Krainer, A. R. Antisense-mediated exon inclusion. doi:10.1007/978-1-61779-767-5_20.

25. Vickers, T. A. *et al.* Efficient Reduction of Target RNAs by Small Interfering RNA and RNase H-dependent Antisense Agents A COMPARATIVE ANALYSIS*. (2002) doi:10.1074/jbc.M210326200.

26. Frazier, K. S. Antisense Oligonucleotide Therapies:The Promise and the Challenges from a Toxicologic Pathologist's Perspective. *Toxicol. Pathol.* **43**, 78–89 (2015).

27. Didiot, M. C. *et al.* Exosome-mediated delivery of hydrophobically modified siRNA for huntingtin mRNA silencing. *Mol. Ther.* **24**, 1836–1847 (2016).

28. Usman, W. M. *et al.* Efficient RNA drug delivery using red blood cell extracellular vesicles. *Nat. Commun.* **9**, 2359 (2018).

29. Ohno, S. I. *et al.* Systemically injected exosomes targeted to EGFR deliver antitumor microrna to breast cancer cells. *Mol. Ther.* **21**, 185–191 (2013).

30. Alvarez-Erviti, L. *et al.* Delivery of siRNA to the mouse brain by systemic injection of targeted exosomes. *Nat. Biotechnol.* **29**, 341–345 (2011).

31. Shirley, J. L., de Jong, Y. P., Terhorst, C. & Herzog, R. W. Immune Responses to Viral Gene Therapy Vectors. *Molecular Therapy* vol. 28 709–722 (2020).

32. Wang, L. *et al.* In Vivo Delivery Systems for Therapeutic Genome Editing. 86–371 doi:10.3390/ijms17050626.

33. Juliano, R. L. & Carver, K. Cellular uptake and intracellular trafficking of oligonucleotides. *Advanced Drug Delivery Reviews* vol. 87 35–45 (2015).

34. Chery, J. *RNA therapeutics: RNAi and antisense mechanisms and clinical applications*. *Postdoc Journal Journal of Postdoctoral Research* vol. 4 www.PostdocJournal.Com (2016).

35. Crooke, S. T., Wang, S., Vickers, T. A., Shen, W. & Liang, X. H. Cellular uptake and trafficking of antisense oligonucleotides. *Nature Biotechnology* vol. 35 230–237 (2017).

36. Geary, R. S., Norris, D., Yu, R. & Bennett, C. F. Pharmacokinetics, biodistribution and cell uptake of antisense oligonucleotides. *Advanced Drug Delivery Reviews* vol. 87 46–51 (2015).

37. Eckstein, F. Phosphorothioates, essential components of therapeutic oligonucleotides. *Nucleic Acid Therapeutics* vol. 24 374–387 (2014).

38. Nishina, T. *et al.* Chimeric antisense oligonucleotide conjugated to α-Tocopherol. *Mol. Ther. - Nucleic Acids* **4**, (2015).

39. Wang, J., Lu, Z., Wientjes, M. G. & Au, J. L. S. Delivery of siRNA therapeutics: Barriers and carriers. *AAPS Journal* vol. 12 492–503 (2010).

40. Nair, J. K. *et al.* Multivalent N -acetylgalactosamine-conjugated siRNA localizes in

hepatocytes and elicits robust RNAi-mediated gene silencing. *J. Am. Chem. Soc.* **136**, 16958–16961 (2014).

41. Hu, B. *et al.* Therapeutic siRNA: state of the art. *Signal Transduction and Targeted Therapy* vol. 5 (2020).

42. Chernikov, I. V., Vlassov, V. V. & Chernolovskaya, E. L. Current development of siRNA bioconjugates: From research to the clinic. *Frontiers in Pharmacology* vol. 10 (2019).

43. Selvam, C., Mutisya, D., Prakash, S., Ranganna, K. & Thilagavathi, R. Therapeutic potential of chemically modified siRNA: Recent trends. doi:10.1111/cbdd.12993.

44. Naso, M. F., Tomkowicz, B., Perry, W. L. & Strohl, W. R. Adeno-Associated Virus (AAV) as a Vector for Gene Therapy. *BioDrugs* vol. 31 317–334 (2017).

45. Tosolini, A. P., Ferraiuolo, L., Stoica, L. & Sena-Esteves, M. Adeno Associated Viral Vector Delivered RNAi for Gene Therapy of SOD1 Amyotrophic Lateral Sclerosis. *Front. Mol. Neurosci.* | *www.frontiersin.org* **1**, 56 (2016).

46. Tomar, R. S., Matta, H. & Chaudhary, P. M. Use of adeno-associated viral vector for delivery of small interfering RNA. doi:10.1038/sj.onc.1206733.

47. Wang, D., L Tai, P. W. & Gao, G. Adeno-associated virus vector as a platform for gene therapy delivery. *Nat. Rev. Drug Discov.* doi:10.1038/s41573-019-0012-9.

48. John Bunker, D. L. Delivery Techniques in Gene Therapy: A Brief Overview. *J. Phys. Chem. Biophys.* **4**, 1–3 (2014).

49. Wang, Y., Miao, L., Satterlee, A. & Huang, L. Delivery of oligonucleotides with lipid nanoparticles ☆. *Adv. Drug Deliv. Rev.* **87**, 68–80 (2015).

50. Jackson, L. A. *et al.* An mRNA Vaccine against SARS-CoV-2 — Preliminary Report. *N. Engl. J. Med.* **383**, 1920–1931 (2020).

51. Sercombe, L. *et al.* Advances and challenges of liposome assisted drug delivery. *Frontiers in Pharmacology* vol. 6 286 (2015).

52. Moss, K. H., Popova, P., Hadrup, S. R., Astakhova, K. & Taskova, M. Lipid Nanoparticles for Delivery of Therapeutic RNA Oligonucleotides. *Molecular Pharmaceutics* vol. 16 2265–2277 (2019).

53. Mohamed, M. *et al.* PEGylated liposomes: immunological responses. *Science and Technology of Advanced Materials* vol. 20 710–724 (2019).

54. Verhoef, J. J. F. & Anchordoquy, T. J. Questioning the use of PEGylation for drug delivery. *Drug Delivery and Translational Research* vol. 3 499–503 (2013).

55. Simons, M. & Raposo, G. Exosomes--vesicular carriers for intercellular communication. *Curr. Opin. Cell Biol.* **21**, 575–581 (2009).

56. Colombo, M., Raposo, G. & Théry, C. Biogenesis, Secretion, and Intercellular Interactions of Exosomes and Other Extracellular Vesicles. *Annu. Rev. Cell Dev. Biol.* **30**, 255–289 (2014).

57. Raposo, G. & Stoorvogel, W. Extracellular vesicles: Exosomes, microvesicles, and friends. *Journal of Cell Biology* vol. 200 373–383 (2013).

58. O'Brien, K., Breyne, K., Ughetto, S., Laurent, L. C. & Breakefield, X. O. RNA delivery by extracellular vesicles in mammalian cells and its applications. *Nature Reviews Molecular Cell Biology* vol. 21 585–606 (2020).

59. Russell, A. E. *et al.* Biological membranes in EV biogenesis, stability, uptake, and cargo transfer: an ISEV position paper arising from the ISEV membranes and EVs workshop. in *Journal of Extracellular Vesicles* vol. 8 1684862 (2019).

60. Valadi, H. *et al.* Exosome-mediated transfer of mRNAs and microRNAs is a novel

mechanism of genetic exchange between cells. *Nat. Cell Biol.* **9**, 654–659 (2007).

61. Webb, R. L. *et al.* Human Neural Stem Cell Extracellular Vesicles Improve Recovery in a Porcine Model of Ischemic Stroke. *Stroke* **49**, 00–00 (2018).

62. Webb, R. L. *et al.* Human Neural Stem Cell Extracellular Vesicles Improve Tissue and Functional Recovery in the Murine Thromboembolic Stroke Model. *Transl. Stroke Res.* **9**, 530–539 (2018).

63. Spellicy, S. E. *et al.* Neural Stem Cell Extracellular Vesicles Disrupt Midline Shift Predictive Outcomes in Porcine Ischemic Stroke Model. *Transl. Stroke Res.* (2019) doi:10.1007/s12975-019-00753-4.

64. Huang, L. *et al.* Exosomes in mesenchymal stem cells, a new therapeutic strategy for cardiovascular diseases? *Int. J. Biol. Sci.* **11**, 238–245 (2015).

65. Zhang, Y., Liu, Y., Liu, H. & Tang, W. H. Exosomes: Biogenesis, biologic function and clinical potential. *Cell and Bioscience* vol. 9 1–18 (2019).

66. Yue, B. *et al.* Exosome biogenesis, secretion and function of exosomal miRNAs in skeletal muscle myogenesis. *Cell Prolif.* **53**, e12857 (2020).

67. Keller, S., Sanderson, M. P., Stoeck, A. & Altevogt, P. Exosomes: From biogenesis and secretion to biological function. *Immunol. Lett.* **107**, 102–108 (2006).

68. Colombo, M. *et al.* Analysis of ESCRT functions in exosome biogenesis, composition and secretion highlights the heterogeneity of extracellular vesicles. *J. Cell Sci.* **126**, 5553–65 (2013).

69. Sterzenbach, U. *et al.* Engineered Exosomes as Vehicles for Biologically Active Proteins. *Mol. Ther.* **25**, 1269–1278 (2017).

70. Villarroya-Beltri, C., Baixauli, F., Gutiérrez-Vázquez, C., Sánchez-Madrid, F. &

Mittelbrunn, M. Sorting it out: Regulation of exosome loading. *Seminars in Cancer Biology* vol. 28 3–13 (2014).

71. Abels, E. R. & Breakefield, X. O. Introduction to Extracellular Vesicles: Biogenesis, RNA Cargo Selection, Content, Release, and Uptake. *Cellular and Molecular Neurobiology* vol. 36 301–312 (2016).

72. Sancho-Albero, M. *et al.* Exosome origin determines cell targeting and the transfer of therapeutic nanoparticles towards target cells. *J. Nanobiotechnology* **17**, 16 (2019).

73. Murphy, D. E. *et al.* Extracellular vesicle-based therapeutics: natural versus engineered targeting and trafficking. *Experimental and Molecular Medicine* vol. 51 1–12 (2019).

74. Jurgielewicz, B., Yao, Y. & Stice, S. Kinetics and Specificity of HEK293T Extracellular Vesicle Uptake using Imaging Flow Cytometry. *Nanoscale Res. Lett.* **15**, (2020).

75. Kamerkar, S. *et al.* Exosomes facilitate therapeutic targeting of oncogenic KRAS in pancreatic cancer. *Nature* **546**, 498–503 (2017).

76. Wiklander, O. P. B. *et al.* Extracellular vesicle in vivo biodistribution is determined by cell source, route of administration and targeting. *J. Extracell. vesicles* **4**, 26316 (2015).

77. Yang, J., Zhang, X., Chen, X., Wang, L. & Yang, G. Exosome Mediated Delivery of miR-124 Promotes Neurogenesis after Ischemia. *Mol. Ther. - Nucleic Acids* **7**, 278–287 (2017).

78. Pardridge, W. M. Drug transport across the blood-brain barrier. *J. Cereb. Blood Flow Metab.* **32**, 1959–1972 (2012).

79. Chen, C. C. *et al.* Elucidation of Exosome Migration Across the Blood–Brain Barrier Model In Vitro. *Cell. Mol. Bioeng.* **9**, 509–529 (2016).

80. Saint-Pol, J., Gosselet, F., Duban-Deweer, S., Pottiez, G. & Karamanos, Y. Targeting and Crossing the Blood-Brain Barrier with Extracellular Vesicles. *Cells* **9**, 851 (2020).

81. Ye, Z. *et al.* Methotrexate-Loaded Extracellular Vesicles Functionalized with Therapeutic and Targeted Peptides for the Treatment of Glioblastoma Multiforme. *ACS Appl. Mater. Interfaces* **10**, 12341–12350 (2018).

82. Mulcahy, L. A. *et al.* Routes and mechanisms of extracellular vesicle uptake. *J. Extracell. Vesicles* **3**, (2014).

83. Horibe, S., Tanahashi, T., Kawauchi, S., Murakami, Y. & Rikitake, Y. Mechanism of recipient cell-dependent differences in exosome uptake. *BMC Cancer* **18**, 47 (2018).

84. McKelvey, K. J., Powell, K. L., Ashton, A. W., Morris, J. M. & McCracken, S. A. Exosomes: Mechanisms of Uptake. *J. Circ. biomarkers* **4**, 7 (2015).

85. Millard, M. *et al.* mTHPC-loaded extracellular vesicles outperform liposomal and free mTHPC formulations by an increased stability drug delivery efficiency and cytotoxic effect in tridimensional model of tumors. *Drug Deliv.* **25**, 1790–1801 (2018).

86. Joshi, B. S., de Beer, M. A., Giepmans, B. N. G. & Zuhorn, I. S. Endocytosis of Extracellular Vesicles and Release of Their Cargo from Endosomes. *ACS Nano* **14**, 4444–4455 (2020).

87. Sancho-Albero, M., Ana Medel-MartínezMartínez ac, ab & MartínMartín-Duque, P. Use of exosomes as vectors to carry advanced therapies. (2020) doi:10.1038/s41929-019-0333-4.

88. Zhou, Y. *et al.* Exosome-mediated small RNA delivery for gene therapy. *Wiley Interdisciplinary Reviews: RNA* vol. 7 758–771 (2016).

89. Zhu, X. *et al.* Comprehensive toxicity and immunogenicity studies reveal minimal effects in mice following sustained dosing of extracellular vesicles derived from HEK293T cells. (2017) doi:10.1080/20013078.2017.1324730.

90. Guo, Y. *et al.* Effects of exosomes on pre-metastatic niche formation in tumors. *Mol. Cancer* **18**, 39 (2019).

91. Saleh, A. F. *et al.* Extracellular vesicles induce minimal hepatotoxicity and immunogenicity. *Nanoscale* **11**, 6990–7001 (2019).

92. Vogel, A., Upadhya, R. & Shetty, A. K. Neural stem cell derived extracellular vesicles: Attributes and prospects for treating neurodegenerative disorders. *EBioMedicine* vol. 38 273–282 (2018).

93. Lapchak, P. A., Boitano, P. D., De Couto, G. & Marbán, E. Intravenous xenogeneic human cardiosphere-derived cell extracellular vesicles (exosomes) improves behavioral function in small-clot embolized rabbits. (2018) doi:10.1016/j.expneurol.2018.06.007.

94. Otero-Ortega, L. *et al.* White matter repair after extracellular vesicles administration in an experimental animal model of subcortical stroke. *Sci. Rep.* **7**, (2017).

95. Xin, H. *et al.* MiR-17-92 cluster in exosomes enhance neuroplasticity and functional recovery after stroke in rats. doi:10.1161/STROKEAHA.116.015204.

96. Mathiyalagan, P. *et al.* Angiogenic Mechanisms of Human CD34 + Stem Cell Exosomes in the Repair of Ischemic Hindlimb. doi:10.1161/CIRCRESAHA.116.310557.

97. Wang, X. *et al.* Engineered Exosomes With Ischemic Myocardium-Targeting Peptide for Targeted Therapy in Myocardial Infarction. doi:10.1161/JAHA.118.008737.

98. Yamashita, T., Takahashi, Y. & Takakura, Y. *Possibility of Exosome-Based Therapeutics and Challenges in Production of Exosomes Eligible for Therapeutic Application*. *Biol. Pharm. Bull* vol. 41 https://www.jstage.jst.go.jp/article/bpb/41/6/41_b18-00133/_pdf/-char/en (2018).

99. Anderson, J. D. *et al.* Comprehensive Proteomic Analysis of Mesenchymal Stem Cell

Exosomes Reveals Modulation of Angiogenesis via Nuclear Factor-KappaB Signaling SIGNIFICANCE STATEMENT. *Stem Cells* **34**, 601–613 (2016).

100. Janas, T., Janas, M. M., Sapoń, K. & Janas, T. Mechanisms of RNA loading into exosomes. *FEBS Letters* vol. 589 1391–1398 (2015).

101. Lee, S.-T. *et al.* Exosome-Based Delivery of miR-124 in a Huntington's Disease Model. *J. Mov. Disord.* **10**, 45–52 (2017).

102. Mizrak, A. *et al.* Genetically engineered microvesicles carrying suicide mRNA/protein inhibit schwannoma tumor growth. *Mol. Ther.* **21**, 101–108 (2013).

103. Xin, H. *et al.* Exosome-Mediated Transfer of miR-133b from Multipotent Mesenchymal Stromal Cells to Neural Cells Contributes to Neurite Outgrowth. *Stem Cells* **30**, (2012).

104. Zhang, Y. *et al.* Microvesicle-mediated delivery of transforming growth factor β1 siRNA for the suppression of tumor growth in mice. *Biomaterials* **35**, 4390–4400 (2014).

105. Jiang, L., Vader, P. & Schiffelers, R. M. Extracellular vesicles for nucleic acid delivery: Progress and prospects for safe RNA-based gene therapy. *Gene Ther.* **24**, 157–166 (2017).

106. Yang, Z. *et al.* Large-scale generation of functional mRNA-encapsulating exosomes via cellular nanoporation. *Nat. Biomed. Eng.* **4**, 69–83 (2020).

107. Kojima, R. *et al.* Designer exosomes produced by implanted cells intracerebrally deliver therapeutic cargo for Parkinson's disease treatment. *Nat. Commun.* **9**, (2018).

108. Hung, M. E. & Leonard, J. N. A platform for actively loading cargo RNA to elucidate limiting steps in EV-mediated delivery. *J. Extracell. Vesicles* **5**, (2016).

109. Sutaria, D. S. *et al.* Low active loading of cargo into engineered extracellular vesicles results in inefficient miRNA mimic delivery. *J. Extracell. Vesicles* **6**, 1333882 (2017).

110. Aqil, F. *et al.* Milk exosomes - Natural nanoparticles for siRNA delivery. *Cancer Lett.*

449, 186–195 (2019).

111. Nasiri Kenari, A., Cheng, L. & Hill, A. F. Methods for loading therapeutics into extracellular vesicles and generating extracellular vesicles mimetic-nanovesicles. *Methods* vol. 177 103–113 (2020).

112. Kooijmans, S. A. A. *et al.* Electroporation-induced siRNA precipitation obscures the efficiency of siRNA loading into extracellular vesicles. *J. Control. Release* **172**, 229–238 (2013).

113. Johnsen, K. B. *et al.* Evaluation of electroporation-induced adverse effects on adipose-derived stem cell exosomes. *Cytotechnology* **68**, 2125–2138 (2016).

114. Pomatto, M. A. C. *et al.* Improved Loading of Plasma-Derived Extracellular Vesicles to Encapsulate Antitumor miRNAs. *Mol. Ther. - Methods Clin. Dev.* **13**, 133–144 (2019).

115. Haney, M. J. *et al.* Exosomes as drug delivery vehicles for Parkinson's disease therapy. *J. Control. Release* **207**, 18–30 (2015).

116. Lamichhane, T. N. *et al.* Oncogene Knockdown via Active Loading of Small RNAs into Extracellular Vesicles by Sonication. *Cell. Mol. Bioeng.* **9**, 315–324 (2016).

117. Shtam, T. A. *et al.* Exosomes are natural carriers of exogenous siRNA to human cells in vitro. *Cell Commun. Signal.* **11**, 88 (2013).

118. Lin, Y. *et al.* Exosome–Liposome Hybrid Nanoparticles Deliver CRISPR/Cas9 System in MSCs. *Adv. Sci.* **5**, 1700611 (2018).

119. Yang, T. *et al.* Delivery of Small Interfering RNA to Inhibit Vascular Endothelial Growth Factor in Zebrafish Using Natural Brain Endothelia Cell-Secreted Exosome Nanovesicles for the Treatment of Brain Cancer. *AAPS J.* **19**, 475–486 (2017).

120. Lin, Y. *et al.* Exosome–Liposome Hybrid Nanoparticles Deliver CRISPR/Cas9 System in

MSCs. *Adv. Sci.* **5**, 1700611 (2018).

121. Stremersch, S. *et al.* Comparing exosome-like vesicles with liposomes for the functional cellular delivery of small RNAs. *J. Control. Release* **232**, 51–61 (2016).

122. Biscans, A. *et al.* Hydrophobicity of Lipid-Conjugated siRNAs Predicts Productive Loading to Small Extracellular Vesicles. *Mol. Ther.* **26**, 1520–1528 (2018).

123. Haraszti, R. A. *et al.* Optimized Cholesterol-siRNA Chemistry Improves Productive Loading onto Extracellular Vesicles. *Mol. Ther.* **26**, 1973–1982 (2018).

124. Gao, X. *et al.* Anchor peptide captures, targets, and loads exosomes of diverse origins for diagnostics and therapy. *Sci. Transl. Med.* **10**, 195 (2018).

125. Chen, Y. S., Lin, E. Y., Chiou, T. W. & Harn, H. J. Exosomes in clinical trial and their production in compliance with good manufacturing practice. *Tzu Chi Medical Journal* vol. 32 113–120 (2020).

126. Cully, M. Exosome-based candidates move into the clinic. *Nature reviews. Drug discovery* vol. 20 6–7 (2021).

127. Lener, T. *et al.* Applying extracellular vesicles based therapeutics in clinical trials - an ISEV position paper. *J. Extracell. Vesicles* **4**, 1–31 (2015).

128. Théry, C. *et al.* Minimal information for studies of extracellular vesicles 2018 (MISEV2018): a position statement of the International Society for Extracellular Vesicles and update of the MISEV2014 guidelines. *J. Extracell. Vesicles* **7**, (2018).

129. Jiang, X. C. & Gao, J. Q. Exosomes as novel bio-carriers for gene and drug delivery. *International Journal of Pharmaceutics* vol. 521 167–175 (2017).

130. Konoshenko, M. Y., Lekchnov, E. A., Vlassov, A. V & Laktionov, P. P. Isolation of Extracellular Vesicles: General Methodologies and Latest Trends. (2018)

doi:10.1155/2018/8545347.

131. Willis, G. R., Kourembanas, S. & Mitsialis, S. A. Toward Exosome-Based Therapeutics: Isolation, Heterogeneity, and Fit-for-Purpose Potency. *Front. Cardiovasc. Med.* **4**, 63 (2017).

132. Ludwig, N., Whiteside, T. L. & Reichert, T. E. Challenges in exosome isolation and analysis in health and disease. *International Journal of Molecular Sciences* vol. 20 (2019).

133. Zhou, Y. *et al.* Exosome-mediated small RNA delivery for gene therapy. *Wiley Interdisciplinary Reviews: RNA* vol. 7 758–771 (2016).

FIGURES

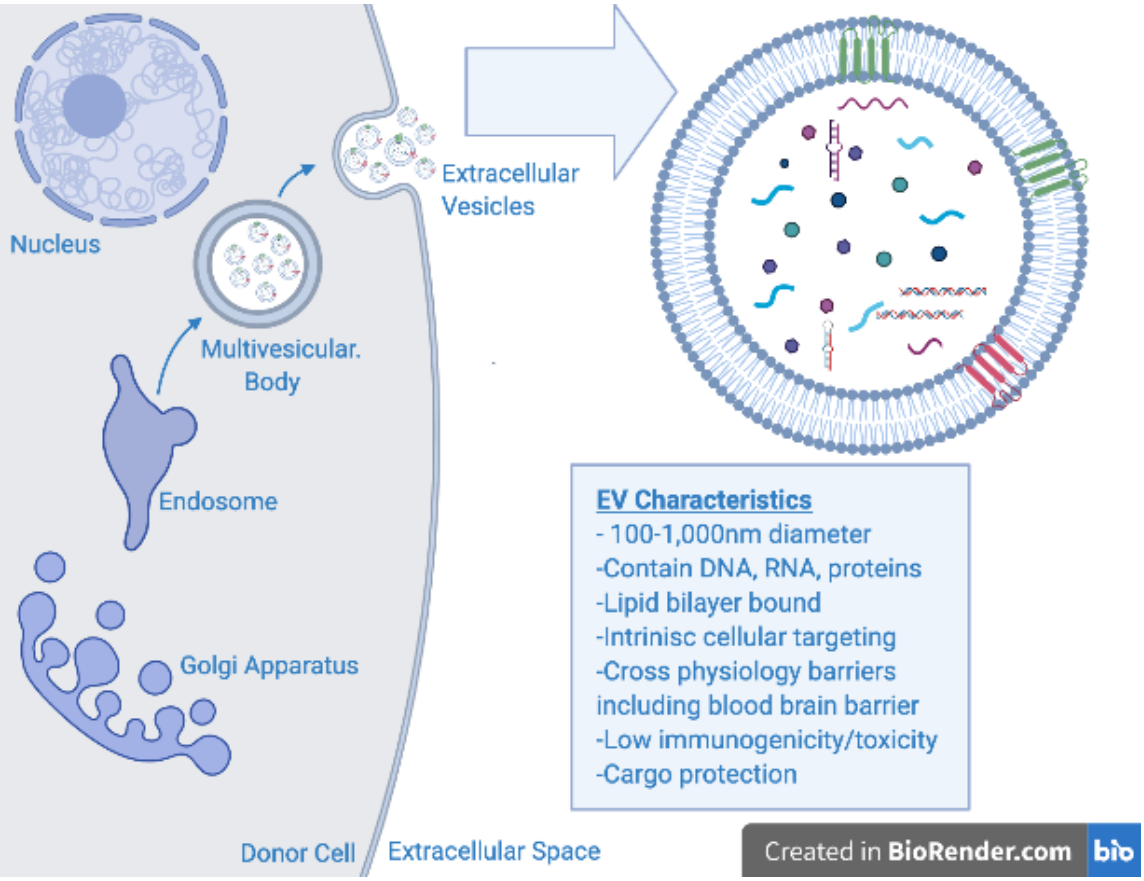

FIGURE 1.1 Schematic of EV Biogenesis and Contents. EVs are formed by the invagination of the early endosome to form the multivesicular body. In the MVB, the vesicles are intraluminal vesicles, and shuttled to be released by the plasma membrane. Once released, the ILVs are coined exosomes or generally extracellular vesicles. EV cargo consists of DNA, RNA, proteins, lipids. The EV membrane contains common tetraspanin proteins including CD9, CD63, and CD81.

Table 1.1 An overview of nucleic acid based therapies including their function, composition, and example disease targets.

Nucleic Acid Based Therapies			
	Function	**Composition**	**Disease Targets**
RNA Interference:			
Small Interfering RNA	1) Cleave mRNA 2) Inhibit translation via RISC	20-27 base pair double stranded oligonucleotides	hATTR, AHP
MicroRNA	Induce translation repression via mRNA deadenylation or decapping	19-25 nucleotides in length derived from short stem-loop RNA	Cancer, Hepatitis
Non-RNA Interference:			
Antisense Oligonucleotide - Splicing	1) Restore mRNA reading frames. 2) Promote inclusion of skipped exons 3) introduce an out-of-frame deletion	8-50 base pair single stranded oligonucleotides	Spinal Muscular Atrophy, Duchenne's Muscalar Dystrophy
Antisense Oligonucleotide - Degradation	Recruit Endonulcease breakdown due to DNA:RNA complex formation	8-50 base pair single stranded oligonucleotides	Cancer

Table 1.2 An overview of Pre-Isolation methods of EV loading of nucleic acids. Techniques include overexpression via transfection, electroporation, TAMEL, and EXOtic systems to exploit endogenous loading of nucleic acids into EVs.

Pre-Isolation EV Loading						
Author (source)	**Method**	**EV Source**	**Cargo**	**Target**	**Disease**	**Result**
Hung 2016	TAMEL Platform	HEK293T	mRNA	Non-Specific	Prostate Cancer	Loading of mRNA was efficient, but minimal fucntional efficacy in recipeint cells.
Katakowski 2012	Transfected Cell Line	hMSC	miRNA	miR-146	Glioma	Decreased EGFR and NF-KB protein levels and significant reduction in xenotransplanted tumor volume
Kojima 2018	EXOtic Device	HEK293T	mRNA	Catalase	Parkinson's Disease	Attenuation of neurotoxicity and neuroinflammation in in vitro and in vivo
Kosaka 2012	Stable Cell Line	HEK293T Cell Media (not isolated EVs)	miRNA	miR-143	Prostate Cancer	50% decrease in cell proliferation and decrease in tumor size with knockdown of KRAS
Lee 2017	Stable Cell Line* (Lipofectamine)	HEK293T	miRNA	miR-124	Huntington's Disease	Decreased REST protein expression, but minimal behavioral changes in mice
Mathiyalagan (protocol) 2017	Transfected Cell Line	CD34+ Stem Cells	miRNA	Non-Specific	N/A	Significant uptake of Cy3 siRNA into HUVECs
Mizrak 2013	Transfected Cell Line	HEK293-T	mRNA/Protei n	CD-UPRT Pathway (cell Death)	Schwann Cell Cancer	Inhibition of schwannoma tumor growth in mice 99
Munoz 2013	Stable Cell Line	U87, T98G	miRNA	miR-9	Glioblastoma	50% decrease in miR9 levels
Ohno 2013	Transfected Cell Line	HEK293T	miRNA	Let7	Breast Cancer	Inhibited targeted luciferase gene and decrease luciferase activity of tumor cells in xenotransplanted mice, suppressed cancer
Okoye	Transfected Cell Line	T-Regulatory Cells	miRNA	Let7-D	Systemic Disease	Th1 cell suppression
Pan 2014	Transfected Cell Line	Hela -229	miRNA	miR-130B	Obesity	Down regulation of of PPAR-y Expression, inhibited adipogenesis and lipogenesis
Sutaria 2017	Transfected Cell Line	HEK293T	miRNA	pre-miR-199a	N/A	Minimal therapeutic efficacy
Yang	Electroporation	Murine BM-MSC	miRNA	miR-124	Brain Infarct	Promoted cortical neural progenitors to obtain neuronal identity and protect against ischemic injury by robust cortical neurogenesis.
Zhang 2014	Transfected Cell Line	Mouse fibroblast L929 cells	siRNA	TGF-Beta1	Tumor Cancer	Suppression of S180 tumor growth in mice

Table 1.3 An overview of Post-Isolation Methods of EV loading of Nucleic Acids. Techniques include electroporation, sonication, co-incubation, transfection, and peptide tagging.

Post-Isolation Loading						
Author (source)	**Method**	**EV Source**	**Cargo**	**Target**	**Disease**	**Result**
Alvarez-Erviti 2011	Electroporation	Murine Dendritic Cells	siRNA	BACE1 and GAPDH	Alzheimer's Disease	Dose dependent knnockdown ~50% and iRNA delivery was demonstrated by the strong mRNA (60%) and protein (62%) knockdown of BACE1, a therapeutic target in Alzheimer's disease
Andaloussi 2012	Electroporation	Dendritic and HEK293T	siRNA	BACE1	Alzheimer's Disease	Significant target gene knockdown
Aqil 2018	Electroporation, Chemical Transfection	Bovine Milk	siRNA	VEGF, EGFR, AKT< MAPK, KRAS	Cancer	a dose-dependent anti-proliferative activity against A549 cells with 5-fold reduction of EGFR levels compared to vehicle and significant reduction in tumor xenografts. Chemical transfection > electroporation
Bai 2019	Electroporation	HEK293T	siRNA	SOX2	Lung Cancer	Increased knockdwon of SOX2 mRNA compared to lipofectamine
Cooper 2014	Electroporation	Murine Dendritic Cells	siRNA	Alpha-Syn	Parkinson's Disease	Downregulation of endogenous α-synuclein in normal mouse brain and human phospho-mimic human S129D α-Syn in transgenic mouse
Faruqu 2018	Electroporation	HEK293	siRNA	Non-Specific	Pancreatic Cancer	SiRNA was internalized into 40% of cells.
Gujrati 2014	Electroporation	E. Coli (K12 W3110 with msbB mutation)	siRNA	Kinesin Spindle Protein	Her2 Cancer	targeted gene silencing and induced highly significant tumor growth regression
Kamerkar 2017	Electroporation	hMSC	siRNA	KRAS	Pancreatic Cancer	Suppression of cancer in multiple mouse models of pancreatic cancer and significant increase in survival.
Koojimans 2013	Electroporation	N2A and HEK293T	siRNA	Non-Specific	N/A	Induction of strong aggregation of siRNA
Lamichhane 2015	Electroporation	HEK293T	dsDNA	Ser(CGA) Gene	N/A	Functional gene delivery was not observed.
Liu	Electroproation	HEK293T	siRNA	Opiod Receptor Mu		Downregulating MOR expression levels in mouse brain
Pomatto 2019	Electroporation, Co-Incubation	Plasma	miRNA	Cel39, miR31, miR-451A	Hepatocarcinoma	Increase cancer cell apoptosis (higher effect following electroporation vs. co-incubation)
Usman 2018	Electroporation	Red Blood Cells	ASO	MiR-125	cute Myeloid Leukemi	Dose dependent knockdown of miR-125A/B and decreased tumor size with suppression of AML progression
Usman 2018	Electroporation	Red Blood Cells	Cas9 mRNA	N/A	N/A	Cas9 protein was efficiently expressed in the nuclei of ~50% MOLM13
Usman 2018	Electroporation	Red Blood Cells	Plasmid DNA	GFP Marker	N/A	EGFP knockout was observed in only ~10% cells
Wahlgren 2012	Electroporation	Plasma, Lung cancer, and HeLA Cells	siRNA	MapK1	N/A	Cell death of targeted monocytes, Silencing of MAPK1 in monocytes and lymphocytes Suppression
Shtam 2013	Electroproation	HeLA	siRNA	Rad51/52	Cancer	siRNA against RAD51 was functional and caused the massive reproductive cell death of recipient cancer cell
Lamichanne 2016	Sonication	MCF-7	siRNA	Her2	Breast Cancer	Knockdown of HER2 mRNA
Shtam 2013	Chemical Transfection	HeLa	siRNA	Rad51/52	Cancer	siRNA against RAD51 was functional and caused the massive reproductive cell death of recipient cancer cell
Yang 2017	Chemical Transfection	Brain Endothelial	siRNA	VEGF	Glioblastoma	Cells treated with siRNA alone demonstrated a knockdown of 40% of VEGF and decreased tumor proliferation in vitro
Zhang 2017	Calcium Transfection	THP-1, RAW 264.7, MH-S, Bone Marrow macrophage (BMDM), or BALF	miRNA	miR-15A	N/A	Efficient overexpression or deletion of the designated miRNAs in the recipient cells both in vivo and in vitro.
Biscans 2018	Co-Incubation	Umbilical MSCs	siRNA	Htt Gene	Huntingon's Diseae	20-80% knockdown of target gene
Didiot 2017	Co-Incubation	U87	siRNA	Htt Gene	Huntingon's Diseae	dose-dependent silencing of Htt mRNA, up to 75% reductionand HTT protein up to 68% reduction and bilateral silencing of up to 35% of Huntingtin mRNA.
Gao 2-18	Co-Incubation (Peptide Tagging)		ASO	Dystrophin Gene	Muscular Dystrophy	18-fold Increase in dystrophin expression in muscular dystrophy mouse model compared to naked ASO
Haraszti 2018	Co-incubation	U87	siRNA	Htt Gene	Huntingon's Diseae	50% knockdown of target gene
Stremersch 2016 (EV Like)	Co-Incubation	B16F10 Melanoma Cells and JAWSII	siRNA	CD45	N/A	Only liposome delivery provided knockdwon of target gene..Anionic fusogenic liposomes outperform ELVs in chol-siRNA delivery in vitro

CHAPTER 2

KINETICS AND SPECIFICITY OF HEK293T EXTRACELLULAR VESICLE UPTAKE USING IMAGING FLOW CYTOEMTRY[2]

[2] Brian J. Jurgielewicz, Yao Yao, Steven L. Stice. 2020. *Nanoscale Research Letters*. 10.11.86/s11671-020-0339-6. Reprinted here with permission of the publisher.

2.1 ABSTRACT

Extracellular vesicles (EVs) are nanosized lipid bilayer-bound vesicles that are naturally secreted from most cell types as a communication mechanism to deliver proteins, lipids, and genetic material. Despite the therapeutic potential of EVs, there is limited information on EV uptake kinetics and specificity. Here, we optimized an imaging flow cytometry (IFC)-based platform to quantitatively assess dose, time, and recipient cell specificity effects on human embryonic kidney cell (HEK293T) EV internalization in a high-throughput manner. We found that HEK293T EV uptake is an active process that is dose and time dependent. Further, the selectivity of EV uptake was quantified *in vitro*, and we found that HEK293T EVs were internalized at higher quantities by cells of the same origin. Lastly, neural stem cells internalized significantly more HEK293T EVs relative to mature neurons, suggesting that stem cells or progenitors, which are more metabolically active than terminally differentiated cells, may have higher rates of active EV internalization. The characterization of EV uptake, notably specificity, dose and time dependence, and kinetic assays will help inform and develop targeted and efficient EV-based therapeutics.

2.2 INTRODUCTION

Extracellular vesicle research is a burgeoning field due to the therapeutic and diagnostic utility of natural and engineered EVs. EVs range from 50-1000 nm in diameter, are produced from all cell types, and enriched with transmembrane proteins including CD63, CD81 and CD9, lipids, proteins, and DNA, RNA, mRNA and microRNA (1–5). EV content, notably active mRNA and miRNA, has been implicated in modulation of recipient cells via de-novo translation and post translational regulation of target cells (4,6). Understanding and then modifying kinetic

EV uptake and internalization will eventually lead to optimized delivery of EV contents to target cells with high enough concentrations to have a therapeutic benefit.

Once thought to be "the garbage of the cells," EVs have been harnessed as an alternative to cell therapies due to many advantages including their biocompatibility, low immunogenicity and toxicity, ability for repeated dosing, various routes of administration, and potential to deliver drugs and genetic therapies (3). Our group has previously reported positive effects of neural stem cell derived EVs in stroke and traumatic brain injury. In both murine and porcine stroke models, EVs improved tissue and functional recovery post stroke (3,7,8). We have also shown EVs to be neuroprotective with functional benefits in a rodent traumatic brain injury model (9). Despite these observed effects and future potential of EVs, there is little understanding of EV uptake specificity and kinetics, which may hinder translation of EV therapeutics into the clinic.

EVs have also been engineered as transference vectors and loaded with therapeutic agents including gene therapies and chemical compounds as an alternative to nanoparticle therapeutics and delivery vectors (4,10–12). HEK293T cells have been widely used as EV producer cells due to their inherent rapid proliferation, high EV yield, and ease of genetic manipulation (13–17). HEK293T EVs delivered gene therapies including miRNA therapeutics for breast cancer (12) and have been used to deliver chemotherapeutics and therapeutic protein constructs in a Schwannoma model (18). Similar to synthetic nanoparticle studies assessing cytotoxicity *in vitro*, MTT toxicity assays displayed low toxicity of unloaded HEK293T EVs and subsequent high cytotoxicity when loaded with chemotherapeutics (10,18–21). Due to this abundant utilization of HEK293T EVs, we analyzed their kinetics and specificity in this study.

Selective or specific uptake refers to an EV's natural ability to target specific cell types. There is abundant evidence on the mechanisms of EV internalization with little consensus on

uptake specificity (22). Often EVs exhibit selective uptake by similar recipient cells as their parent cells, epithelial cells internalize more epithelial derived EVs than other recipient cells (23,24) and mesenchymal stem cells (MSC) internalize a significantly greater amount of MSC derived EVs compared to other cell lines *in vitro* (24). However, other studies found that EVs are internalized by all cell types and display a non-selective biodistribution when administered i*n vivo* (22,25). Despite the immense therapeutic potential and interest of EVs, there is a deficiency in the understanding of EV uptake specificity. By better understanding EV uptake specificity, we can appropriately choose EV producer cells that are selectively internalized by recipient cells of interest and thus improve the therapeutic applicability of EVs.

A potential reason for conflicting EV uptake results is the lack of standardization in measurement platforms, including analyses of dose and time effects. Recently, an International Society for Extracellular Vesicles (ISEV) group of experts, released a position paper emphasizing the need for analysis of dose and time, amongst other confounding factors on EV uptake (26). The group stated that 'one dose does not fit all,' and that dose may affect EV uptake or selectivity (26). Elevating doses of HEK293T EVs shifts the biodistribution pattern *in vivo* (27). Uptake profiles of serum derived EVs were significantly altered by dose (28). Additionally, co-incubation times of EVs with recipient cells ranging from 15 minutes to 48 hours (24,29–33) may alter uptake measurements. If adopted by EV researchers and industry, a quantifiable and reliable process to determine standard dose and time curves, to help identify the minimum effective dose may lead to more robust and useful studies.

Previously, researchers have used standard flow cytometry along with various forms of low throughput microscopy including confocal microscopy to analyze EV uptake (32–34). However, these technologies have several limitations. Confocal microscopy can be time

consuming and subjective. Traditional flow cytometers have been designed to measure biological particles in the cellular range, cannot differentiate EV swarm or coincidence, and have increased noise due to triggering (35–38). As mentioned by the ISEV group, there is growing awareness of the physical limitations of traditional flow cytometry and highlight the demand for specialized flow cytometry with detection limits in the 100 nm range (26,38). Imaging flow cytometry (IFC) combines the high throughput quantitative nature of flow cytometry along with fluorescence imaging technology which can resolve inherently small fluorescent particles, down to 100nm in diameter (38). IFC capabilities lead to low noise/background, decreased swarming, and charged coupled devices for image clarity (37,39). These characteristics assist in developing a gating strategy for characterizing EVs and uptake with visual confirmation in a high throughput manner as an accurate and quantifiable EV uptake platform (36,37,40).

In this study, CD63-eGFP expressing HEK293T cells were utilized as the donor cell line for EV production due to their common usage in therapeutic development. The isolated fluorescent EVs were co-cultured with recipient cell lines including neural and endothelial cells. Uptake was quantified using IFC, resulting in a standardized platform to measure the important kinetic EV uptake and internalization features for *in vitro* cell systems. Further we provide data on a process to quantify uptake of fluorescent EVs uptake in differing conditions and cultured cell lines to elucidate selective EV uptake.

2.3 MATERIALS AND METHODS

Cell Culture

Human embryonic kidney cells (HEK293T) were purchased from ATCC and cultured in DMEM containing 10% fetal bovine serum, 100 units/mL penicillin, 100 ug/mL streptomycin. Human neural stem cells (hNSC), SH-SY5Y neural cells, C3A liver epithelial cells, human umbilical

vein endothelial cells (HUVEC), and neurons were all cultured under standard conditions at 37°C, 5% CO_2 prior to extracellular vesicle uptake assays.

EV Labeling and Isolation

CD63-eGFP plasmid DNA was obtained from Addgene (#62964). CD63-pEGFP C2 was a gift from Paul Luzio (Addgene plasmid #62964). HEK293T cells were cultured to 70% confluency in 10 cm dishes and 10 ug plasmid DNA was transfected using Lipofectamine 2000 according to the manufacturer's instructions. 24 hours post transfection media was changed to standard HEK293T media devoid of fetal bovine serum and collected for 3 consecutive days. As previously described (3), HEK293T media was filtered through a 0.22 µm filter and enriched by ultrafiltration using a 100 kDa regenerated cellulose Amicon centrifugal filter units and washed twice with PBS++. EVs were concentrated to one mL and concentration and size distributions were measured on Nanosight NS300 by the manufacturer's protocol (Malvern, United Kingdom). EVs were isolated from different HEK293T culture vessels, each vessel considered separate biological replicates, with three technical replicates within each biological replicate (Minimum of nine samples total for each condition).

Uptake Assays

Recipient cell lines were seeded at 60% confluency in a 6-well plate for 24 hours under standard culture conditions at 37°C. Standard media was changed to fetal bovine serum free (FBS-) media prior to extracellular vesicle co-culture. GFP-tagged EVs were administered to cells at varying doses and time points. After co-culture, cells were resuspended in 5% trypsin and concentrated to around one million cells per 50 uL for flow cytometry. 37°C is the standard for EV uptake experiments in our assays as it has been the standard used for both cell culture and *in vitro* EV uptake platforms (31,41–44).

Inhibitory Assays

Cold Assay - EVs were co-cultured with recipient cells at 4°C to effectively 'pause' cell culture growth and inhibit active processes (45). 4°C inhibits all active forms of EV uptake (31,41–44).

Fixed Assay - Recipient cells were fixed in 4% paraformaldehyde for 30 minutes on ice and washed with PBS immediately before co-culture with EVs to inhibit all active forms of EV uptake.

ImageStreamX Acquisition

Acquisition was performed on the ImageStreamX Mark II Imaging Flow Cytometer (Luminex Corporation, Seattle, Washington) using the INSPIRE software. A minimum of 5,000-10,000 cell events were acquired. Each biological sample was replicated in three technical replicates wells and individually acquired on the ISx. Brightfield images were collected on channel one and side scatter (785 nm) on channel six. Green fluorescent protein (GFP) was excited by 488 nm argon laser at 200 mW and fluorescence was collected on channel two (505 560 nm). 60x magnification was used on every sample along with a low acquisition rate for high sensitivity.

IDEAS Analysis

Data and image analyses were conducted using the IDEAS software (Luminex). The gating strategy is the following:

1. Focus gate was determined to eliminate cells that were not in the field of focus using the Gradient RMS value. 2. The focused cells were gated to eliminate doublets and debris using area brightfield vs. aspect ratio brightfield. Gated data was used to create histograms and generate statistic references measuring fluorescence intensity (sum of all pixels in an image), maximum pixel intensity (intensity of the brightest pixels in an image), along with spot count values via internal algorithms for every sample. Spot count features were generated using the applicable

IDEAS Wizards. Spot count, mean intensity, and maximum pixel ratio are calculated by (Output value with EVs/Output value without EVs).

Statistics:

All quantitative data was analyzed via GraphPad Prism 8.1.2 (San Diego, California) and done in triplicates. The data are presented as mean ± standard error of the mean (S.E.M.). Statistical significance was determined using an unpaired T-test or a One-way analysis of variance (ANOVA) with Tukey's or Dunnett's multiple comparison post-hoc compared to controls when appropriate. $p < 0.05$ was considered significant.

2.4 RESULTS

CD63eGFP tagged HEK293T Extracellular Vesicle Properties.

To generate fluorescently labeled EVs for analyzing the kinetics and uptake of extracellular vesicles, HEK293T cells were transfected with a plasmid carrying CD63-eGFP fusion protein. CD63 is a tetraspanin protein commonly enriched in the membrane of exosomes making it an optimal target for EV fluorescent tagging (46,47). Spent media was collected from HEK293T cell culture and EVs were isolated as previously reported (8). We compared the size and distribution of EVs isolated from CD63-eGFP transfected HEK293T cells to non-transfected HEK293T cells. Control and CD63-eGFP transfected HEK293T EVs displayed an average median diameter of 110.28 nm and 103.616 nm respectively, as measured by nanotracking software (Figure 2.1A), which is consistent with the reported size of HEK293T EVs (13,15,27,48). No significant differences in median diameter ($p=0.1615$) and distribution ($p=0.4225$) of EVs isolated from non-transfected and CD63-eGFP transfected HEK293T cells were observed. eGFP labeling did not alter size of HEK293T EVs (Figure 2.1B).

IFC assay was conducted to determine if the CD63-eGFP was associated with EVs. As a fluorescent negative control, 1.34 μM beads in buffer solution (Figure 2.1C top), lacked fluorescence when exposed to the 488 nm excitation wavelength, but were visible in brightfield (BF) and side scatter (SSC). Untagged HEK293T EVs were negative in the BF, GFP, and SSC, suggesting a small size below the BF threshold and lack of fluorescence (Figure 2.1D, middle). The absence in BF signifies an EV size smaller than 300 nm, which suggests minimal swarming of EVs. Lastly, CD63-eGFP tagged EVs are negative in BF and positive in the GFP channel signifying positive fluorescence of the HEK293T EVs (Figure 2.1C, bottom). The positive signal in the GFP channel may be indicative of a single EV or a group of fluorescent EVs. Collectively, these results show that the isolated HEK293T EVs have standard size and protein marker profiles consistent with previous reports of HEK293T exosomes and eGFP labeling does not alter the size of HEK293T EVs (5,27).

Using a commercially available flow cytometry-based method to measure common EV markers, we determined the overall EV tetraspanin profile (5). Isolated HEK293T EVs from control and CD63-eGFP expressing HEK293T cells were positive for standard EV markers including CD9, CD63, and CD81 as measured in relative fluorescence units (Figure 2.1D). As previously reported, CD29 was also found on the surface of HEK293T EVs and CD63-eGFP transfected HEK293T EVs (5). These results indicate that the isolation and tagging methods for HEK293T EV result in EVs with common HEK293T exosome markers.

2. Active uptake of HEK293T EVs

Two inhibitory internalization assays were performed. HEK293T EVs were co-cultured with recipient cells at 4°C (cold) or with recipient cells previously fixed with paraformaldehyde (fixed). The treatments decreased the presence of eGFP-labelled EVs in the recipient cells

compared to recipient cells co-cultured with EVs under physiological conditions (Figure 2.2A). Cold and fixed inhibitory assays reduced the spot count (Cold: p=0.0127, Fixed: p=0.0078), intensity (Cold: p=0.0105, Fixed: p=0.0374), and maximum pixel (Cold: p=0.0159, Fixed: p=0.0149) of fluorescence signals in recipient cells without treatments, indicating inhibition of EV uptake. These results infer that eGFP localization and increases in output parameters signify that HEK293T EVs are internalized for the following uptake assays.

3. Dose dependent HEK293T EV uptake

To develop a standard dose curve for the IFC platform, HEK293T EVs were co-cultured with HEK293T recipient cells at increasing doses ranging from 0 to 20,000 EVs per cell at 37°C. Representative IFC images exhibited a visual increase of eGFP fluorescence with elevated doses of EVs (Figure 2.3A). The lowest number of EVs that could be detected was 6,000 EVs per co-cultured HEK293T cell. At this level, spot count (p=0.0012), intensity (p=0.0075), and maximum pixel (p=0.0005), measurements were significantly greater than recipient cells without EVs (Figure 2.3B-D). Therefore, doses of 6,000 HEK293T EVs is the low threshold for uptake in our experimental condition. Similarly, doses of 10,000 and 20,000 EVs had higher spot count (10,000: p=0.0009; 20,000: p<0.0001), intensity (10,000: p<0.0001; 20,000: p<0.0001), and maximum pixel (10,000: p<0.0001; 20,000: p<0.0001) compared to cells without EVs. Comparing between the higher doses, there are no significant differences in spot count (6,000 vs. 10,000: p=0.999, 10,000 vs. 20,000: p=0.0927), intensity (6,000 vs. 10,000: p=0.8482, 10,000 vs. 20,000: p=0.999), and maximum pixel count (6,000 vs. 10,000: p=0.6056, 10,000 vs. 20,000: p=0.5281) between 6,000 and 10,000, along with 10,000 vs. 20,000. Similarly, comparing between 6,000 and 20,000, there is no statistical difference in spot count (p=0.0787) and intensity (p=0.8083). There is a significant difference in maximum pixel between 6,000 and

20,000 ($p=0.0140$). Overall, the yield curve displays a significant dose dependence in all parameters (Spot, Intensity, Max Pixel, $p<0.0001$). These results indicate that HEK293T EV uptake is dose dependent with a minimum threshold of 6,000 HEK293T EVs per cell.

4. **HEK293T EV temporal uptake**

Using 6,000 EVs per cell, HEK293T EVs were co-cultured with HEK293T cells for increasing lengths of time prior to IFC, ranging from 5 minutes to 24 hours. Length of EV exposure played a key role in the amount of visible fluorescence in the recipient cells, declining after 12 hours (Figure 2.4A). Initially, 30 minutes of co-culture displayed a significant increase in spot count ($p=0.0081$) suggesting a possible trend towards EV uptake, but not in other uptake parameters (Intensity: $p=0.3073$, Max Pixel: $p=0.0952$) (Figure 2.4B-D). At two hours of co-culture, significantly higher spot count ($p=0.0028$), intensity ($p=0.0420$), and maximum pixel ($p=0.0006$) were recorded compared to the recipient cells without EVs. Again, at 4 hours of co-culture all parameters were greater than controls (Spot count: $p=0.0003$, Intensity: $p<0.0001$, Max pixel: $p<0.0001$). Intensity and maximum pixel continued to be higher than controls at 4, 12, and 24 hours of co-culture. There were no differences in any uptake parameters between 4 hours and 12 hours of co-culture (Spot: $p=0.999$, Intensity: $p=0.5797$ Maximum Pixel: $p=0.2489$). However, intensity ($p=0.0191$), and maximum pixel ($p=0. 0027$) decreased between 12 and 24 hours of co-culture (Figure 2.4C-D). Similar to the dose curve, HEK293T EV uptake is time dependent with consistent EV uptake at 4 hours of incubation and a peak at 12 hours. Collectively, a dose of 6,000 EVs per cell seeded and a co-culture of 4 hours has been standardized for the following uptake assays.

5. **Comparative uptake of HEK293T EVs by Multiple Cell Lines**

The hypothesis that EV uptake is a selective process where EVs are preferentially taken up by cells of their own origin was tested using IFC. HEK293T EVs were co-cultured with HEK293T cells or other cell lines: epithelial (C3A liver cells), endothelial (Human Umbilical Vein Endothelial Cells), and neural (SH-SY5Y Glioblastoma Cells.). eGFP fluorescence is more abundant in HEK293T cells as compared to the other cell types (Figure 2.5A). Compared to C3A and HUVECs, HEK293T cells had significantly higher fluorescence intensity (C3A: p=0.0321; HUVEC: p=0.0055) (Figure 2.5C), when co-cultured with HEK293T EVs. Additionally, HEK293T cells had higher maximum pixel (C3A: p=0.0221; HUVEC p=0.0079; SH-SY5Y: p=0.0486) (Figure 2.5D) as compared to all other recipient cell lines (Figure 5B). Regarding intensity, SH-SY5Y cells was significantly higher than HUVECs when co-cultured with HEK293T EVs (p=0.0304). These results support HEK293T EV selective uptake up by HEK293T cells compared to other cell lines *in vitro*.

6. **Differentiation status of neural cells and HEK293T EV internalization**

Since EVs have been implicated for therapeutic and delivery purposes targeting neural diseases, human neural stem cells (hNSCs) and mature human neurons were used as recipient cell lines in our system to examine if the differentiation status of the recipient cell plays a role in selective uptake of EVs. Representative images from IFC displayed visual evidence of uptake in both cell types, but with the greatest eGFP localization in hNSCs (Figure 2.6A). hNSCs co-cultured with HEK293T EVs have higher spot count (p=0.0082) and max pixel (p=0.0083) as compared to mature neurons. Together, these results suggest that differentiation status of neural cells affects uptake of HEK293T EVs.

2.5 DISCUSSION

EV in vitro uptake standardization process

A group of international experts on EVs emphasized a need to effectively determine the minimal effective dose of EVs for uptake assays and here we have developed a system that can be effectively adopted by the field (26). There are challenges when analyzing EV uptake. For example, as we and others observed, results can differ if the EV dose and exposure time are altered (26). We addressed HEK293T EV dose and concentration as a kinetic variable. Also, an *in vitro* minimum effective dose may more uniformly predict *in vivo* biodistribution of EVs and be used to develop more consistent *in vivo* dosing parameters for EV therapeutics and delivery. In an *in vivo* mouse EV biodistribution study, increasing dose of HEK293T EVs resulted in a shift of the relative EV distribution in organs (27). Similar to findings in a prior *in vitro* study using bladder cancer EVs (39), HEK293T EVs displayed a strong dose dependence with a minimal effective dose at 6,000 EVs in our study. We are the first to use particles per cell as a sensitive dose measurement *in vitro*, which better correlates with *in vivo* models using particles per body weight. Our data also indicated a dose saturation limit after 6,000 EVs, potentially informing future *in vivo* dose ranging studies by indicating that higher doses may have limited benefits.

Another potential confounding variable of measuring EV uptake is the potential temporal effects on EV uptake. In our system, we found strong time dependence with uptake as early as 2 hours with a potential decrease between 12 and 24 hours. Similar to our findings, time dependence was reported in few studies using bladder cancer cells, tumor cells, and others with uptake as early as 15 minutes through 24 hours (29–33,39,43,49). As seen with HEK293T EVs, the lower values at 24 hours of co-culture may be a result of cell division or

recycling/degradation of EVs internalized at early time points (50). Specifically, since EVs have been shown to be internalized then broken down or internalized then released after 24 hours, longer incubations may generate inaccurate internalization readouts (31,50). Our study is the first to use IFC to provide visual and quantitative evidence of a time dependent yield curve on HEK293T EV uptake.

As the ISEV position paper suggests, the choice of an EV label may affect uptake, necessitating less disruptive techniques such as the GFP tagging methods used in our study. Specifically, 72% of researchers participating in a survey claim that lipid dye experiments are unreliable unless proper controls are used (26). EV dyes do not reliably correlate with small EV content and may even increase vesicle size. Contamination of mislabeled lipoproteins and protein content and dye aggregation contributed to false positives (51,52). Therefore, we fused CD63 with an eGFP to label the HEK293T EVs. Similar to other reports of protein tagging, HEK293T EVs were GFP positive with no observed differences in diameter and maintained standard EV surface protein composition (38,46). Despite this, it is important to note that labeling EVs with specific EV proteins may limit the tracking to only a few subtypes of EVs expressing the respective markers. Other potential limitations may be that the fluorescence intensity is dependent on protein expression level, the efficiency of EV membrane labeling, and excitation strength of the light source (53). However, IFC is sensitive, detecting low fluorescence intensity with accurate visualization of CD63-GFP particles at the 100nm range (38,54).

Selective uptake

EVs display proteins and other signals that may confer selective uptake (22,23,55). Since the first step of EV biogenesis is the invagination of the plasma membrane, the EV membrane contains similar proteins, receptors, adhesion molecules, and integrins when compared with the

donor cell membrane (22,24,55). The lipid composition and tetraspanin proteins on EV membranes regulated by donor cells may contribute to EV tropisms with recipient cells (23,34,56). MSC EVs selectively transported contents into MSCs, despite closer proximity to monocytes (24). In contrast others report that natural EVs were taken up equally by any cell type, regardless of EV origin (11,22,25,57) when utilizing imaging or functional knockdown assays. Using the IFC platform, we found that HEK293T extracellular vesicles are taken up at greater quantities by HEK293T cells than other reported cell lines, thus suggesting an inherent EV uptake specificity. Through this outcome and the versatility of IFC, EV sources can be appropriately selected and analyzed for targeting specific recipient cells. To our knowledge this is the first study utilizing imaging flow cytometry to analyze the specificity of HEK293T EVs.

In addition to self-selectivity, differentiation status of recipient cells has been hypothesized to play a role in uptake of EVs (32,58,59). As our group and others have shown, EVs have therapeutic effects in the central nervous system and are known to modulate cell functions in neuronal development and adults (3,7–9,60). Here for the first time, differentiation status of neurons affected EV uptake, where human neural stem cells had significantly greater uptake of HEK293T EVs compared to mature neurons. Immature hNSCs more actively internalize exogenous EVs than quiescent mature neurons. Since hNSCs are highly proliferative cells in culture, they may nonspecifically internalize nutrients and EVs. Similarly, immature dendritic cells internalized EVs at higher levels than mature dendritic cells (32,59). However, another study with myeloid precursor cells found that the mature dendritic cells and macrophages internalized more EVs than immature dendritic cells and monocytes (58). The observed differences can be attributed to the phagocytic activity of further differentiated myeloid

cells. Due to the *in vitro* evidence supporting selective uptake, HEK293T EVs can be used to modulate undifferentiated neurons in future therapeutic applications.

Conclusions:

In summary, we have further developed a quantitative and high throughput platform for analyzing HEK293T EV uptake kinetics. This platform can be extended to other donor EVs and recipient cell types, and assays for liposomes and synthetic nanoparticle delivery vectors. Significantly, we found that HEK293T EV uptake is a selective process, with specificity towards HEK293T cells. The IFC assays developed here can be used to better define parameters used in *in vivo* dose escalation and biodistribution studies and provide instrumental information for a predictive model of EV uptake outcomes *in vivo.*

2.6 REFERENCE**S**

1. Raposo G, Stoorvogel W. Extracellular vesicles: Exosomes, microvesicles, and friends. J. of Cell Bio: Review. 2013;2000(4):373-383.
2. Colombo M, Raposo G, Théry C. Biogenesis, Secretion, and Intercellular Interactions of Exosomes and Other Extracellular Vesicles. Annu Rev Cell Dev Biol. 2014 Oct 11;30(1):255–89.
3. Webb RL, Kaiser EE, Jurgielewicz BJ, Spellicy S, Scoville SL, Thompson TA, et al. Human Neural Stem Cell Extracellular Vesicles Improve Recovery in a Porcine Model of Ischemic Stroke. Stroke. 2018;49.
4. Marcus ME, Leonard JN. FedExosomes: Engineering Therapeutic Biological Nanoparticles that Truly Deliver. Pharmaceuticals. 2013;6:659–80.
5. Wiklander OPB, Bostancioglu RB, Welsh JA, Zickler AM, Murke F, Corso G, et al. Systematic methodological evaluation of a multiplex bead-based flow cytometry assay for

detection of extracellular vesicle surface signatures. Front Immunol. 2018 Jun 13;9(JUN):1326.

6. Valadi H, Ekström K, Bossios A, Sjöstrand M, Lee JJ, Lötvall JO. Exosome-mediated transfer of mRNAs and microRNAs is a novel mechanism of genetic exchange between cells. Nat Cell Biol. 2007 Jun;9(6):654–9.

7. Webb RL, Kaiser EE, Scoville SL, Thompson TA, Fatima S, Pandya C, et al. Human Neural Stem Cell Extracellular Vesicles Improve Tissue and Functional Recovery in the Murine Thromboembolic Stroke Model. Transl Stroke Res. 2018;9(5):530–9.

8. Spellicy SE, Kaiser EE, Bowler MM, Jurgielewicz BJ, Webb RL, West FD, et al. Neural Stem Cell Extracellular Vesicles Disrupt Midline Shift Predictive Outcomes in Porcine Ischemic Stroke Model. Transl Stroke Res. 2019. doi.org/10.1007/s12975-019-00753-4.

9. Sun MK, Passaro AP, Latchoumane C-F, Spellicy SE, Bowler M, Goeden M, et al. Extracellular vesicles mediate neuroprotection and functional recovery after traumatic brain injury. J Neurotrauma. 2020;37(11):1358-1369.

10. Parthiban C, Pavithra M, Vinod Kumar Reddy L, Sen D, Melvin Samuel S, Singh NDP. Visible-Light -Triggered Fluorescent Organic Nanoparticles for Chemo-Photodynamic Therapy with Real-Time Cellular Imaging. ACS Appl Nano Mater. 2018;1(11):6281–8.

11. Alvarez-Erviti L, Seow Y, Yin H, Betts C, Lakhal S, Wood MJA. Delivery of siRNA to the mouse brain by systemic injection of targeted exosomes. Nat Biotechnol. 2011;29(4):341–5.

12. Ohno SI, Takanashi M, Sudo K, Ueda S, Ishikawa A, Matsuyama N, et al. Systemically injected exosomes targeted to EGFR deliver antitumor microrna to breast cancer cells. Mol Ther. 2013;21(1):185–91.

13. Ferguson S, Kim S, Lee C, Deci M, Nguyen J. The Phenotypic Effects of Exosomes Secreted from Distinct Cellular Sources: A Comparative Study based on miRNA Composition. AAPS J. 2019;20(4).

14. Johnsen KB, Gudbergsson JM, Skov MN, Pilgaard L, Moos T, Duroux M. A comprehensive overview of exosomes as drug delivery vehicles - Endogenous nanocarriers for targeted cancer therapy. Biochimica et Biophysica Acta - Reviews on Cancer. 2014. 1846:75–87.

15. Faruqu FN, Xu L, Al-Jamal KT. Preparation of exosomes for siRNA delivery to cancer cells. J Vis Exp. 2018;2018(142):58814.

16. Liu Y, Li D, Liu Z, Zhou Y, Chu D, Li X, et al. Targeted exosome-mediated delivery of opioid receptor Mu siRNA for the treatment of morphine relapse. Sci Rep. 2015 Dec 3;5(1):17543.

17. Zhu X, Badawi M, Pomeroy S, Sutaria DS, Xie Z, Baek A, et al. Comprehensive toxicity and immunogenicity studies reveal minimal effects in mice following sustained dosing of extracellular vesicles derived from HEK293T cells. J Extracell Vesicles. 2017;6(1324730)

18. Mizrak A, Bolukbasi MF, Ozdener GB, Brenner GJ, Madlener S, Erkan EP, et al. Genetically engineered microvesicles carrying suicide mRNA/protein inhibit schwannoma tumor growth. Mol Ther. 2013;21(1):101–8.

19. Samuel MS, Shah SS, Bhattacharya J, Subramaniam K, Pradeep Singh ND. Adsorption of Pb(II) from aqueous solution using a magnetic chitosan/graphene oxide composite and its toxicity studies. Int J Biol Macromol. 2018;115:1142–50.

20. Samuel MS, Selvarajan E, Subramaniam K, Mathimani T, Seethappan S, Pugazhendhi A. Synthesized β-cyclodextrin modified graphene oxide (β-CD-GO) composite for

adsorption of cadmium and their toxicity profile in cervical cancer (HeLa) cell lines. Process Biochem. 2020;93:28–35.

21. Samuel MS, Jose S, Selvarajan E, Mathimani T, Pugazhendhi A. Biosynthesized silver nanoparticles using Bacillus amyloliquefaciens; Application for cytotoxicity effect on A549 cell line and photocatalytic degradation of p-nitrophenol. J Photochem Photobiol B Biol. 2020;202(111642):1011-1344.
22. Mulcahy LA, Pink RC, Raul D, Carter F, David D, Carter RF. Routes and mechanisms of extracellular vesicle uptake. J Extracell Vesicles. 2014;3(24641).
23. Rana S, Yue S, Stadel D, Zöller M. Toward tailored exosomes: The exosomal tetraspanin web contributes to target cell selection. Int J Biochem Cell Biol. 2012;44(9):1574–84.
24. Sancho-Albero M, Navascués N, Mendoza G, Sebastián V, Arruebo M, Martín-Duque P, et al. Exosome origin determines cell targeting and the transfer of therapeutic nanoparticles towards target cells. J Nanobiotechnology. 2019 Dec 25;17(1):16.
25. Zech D, Rana S, Büchler MW, Zöller M. Tumor-exosomes and leukocyte activation: an ambivalent crosstalk. Cell Comm. and Sig. 2012;10(37).
26. Russell AE, Sneider A, Witwer KW, Bergese P, Bhattacharyya SN, Cocks A, et al. Biological membranes in EV biogenesis, stability, uptake, and cargo transfer: an ISEV position paper arising from the ISEV membranes and EVs workshop. J of Extracellular Vesicles. 2019; 8(1).
27. Wiklander OPB, Nordin JZ, O'Loughlin A, Gustafsson Y, Corso G, Mäger I, et al. Extracellular vesicle in vivo biodistribution is determined by cell source, route of administration and targeting. J Extracell vesicles. 2015;4:26316.
28. Busatto S, Giacomini A, Montis C, Ronca R, Bergese P. Uptake Profiles of Human Serum

Exosomes by Murine and Human Tumor Cells through Combined Use of Colloidal Nanoplasmonics and Flow Cytofluorimetric Analysis. Anal Chem. 2018;90(13):7855–61.

29. Feng D, Zhao WL, Ye YY, Bai XC, Liu RQ, Chang LF, et al. Cellular internalization of exosomes occurs through phagocytosis. Traffic. 2010 May;11(5):675–87.

30. Mastoridis S, Bertolino GM, Whitehouse G, Dazzi F, Sanchez-Fueyo A, Martinez-Llordella M. Multiparametric analysis of circulating exosomes and other small extracellular vesicles by advanced imaging flow cytometry. Front Immunol. 2018 Jul 6 ;9(JUL):1583.

31. Tian T, Wang Y, Wang H, Zhu Z, Xiao Z. Visualizing of the cellular uptake and intracellular trafficking of exosomes by live-cell microscopy. J Cell Biochem. 2010 Jun 7;111(2):488–96.

32. Morelli AE, Larregina AT, Shufesky WJ, Sullivan MLG, Stolz DB, Papworth GD, et al. Endocytosis, intracellular sorting, and processing of exosomes by dendritic cells. Blood. 2004 Nov 15;104(10):3257–66.

33. Costa Verdera H, Gitz-Francois JJ, Schiffelers RM, Vader P. Cellular uptake of extracellular vesicles is mediated by clathrin-independent endocytosis and macropinocytosis. J Control Release. 2017 Nov 28;266:100–8.

34. Hazan-Halevy I, Rosenblum D, Weinstein S, Bairey O, Raanani P, Peer D. Cell-specific uptake of mantle cell lymphoma-derived exosomes by malignant and non-malignant B-lymphocytes. Cancer Lett. 2015;364(1):59–69.

35. Gomes J, Lucien F, Cooper TT, Kim Y, Williams KC, Liao X, et al. Analytical Considerations in Nanoscale Flow Cytometry of Extracellular Vesicles to Achieve Data Linearity. Thromb Haemost. 2018 Aug 15;118(09):1612–24.

36. Lannigan J, Erdbruegger U. Imaging flow cytometry for the characterization of extracellular vesicles. Methods. 2017 Jan 1;112:55–67.

37. Erdbrügger U, Rudy CK, E. Etter M, Dryden KA, Yeager M, Klibanov AL, et al. Imaging flow cytometry elucidates limitations of microparticle analysis by conventional flow cytometry. Cytom Part A. 2014 Sep 1;85(9):756–70.

38. Görgens A, Bremer M, Ferrer-Tur R, Murke F, Tertel T, Horn PA, et al. Optimisation of imaging flow cytometry for the analysis of single extracellular vesicles by using fluorescence-tagged vesicles as biological reference material. J Extracell Vesicles. 2019;8(1).

39. Franzen CA, Simms PE, Van Huis AF, Foreman KE, Kuo PC, Gupta GN. Characterization of uptake and internalization of exosomes by bladder cancer cells. Biomed Res Int. 2014;2014.

40. Ofir-Birin Y, Abou karam P, Rudik A, Giladi T, Porat Z, Regev-Rudzki N. Monitoring extracellular vesicle cargo active uptake by imaging flow cytometry. Front Immunol. 2018 May 24;9(MAY):1011.

41. Delenclos M, Trendafilova T, Mahesh D, Baine AM, Moussaud S, Yan IK, et al. Investigation of endocytic pathways for the internalization of exosome-associated oligomeric alpha-synuclein. Front Neurosci. 2017 Mar 30;11(MAR).

42. Temchura V V, Tenbusch M, Nchinda G, Nabi G, Tippler B, Zelenyuk M, et al. Enhancement of immunostimulatory properties of exosomal vaccines by incorporation of fusion-competent G protein of vesicular stomatitis virus. Vaccine. 2008;26:3662–72.

43. Escrevente C, Keller S, Altevogt P, Costa J. Interaction and uptake of exosomes by ovarian cancer cells. BMC Cancer. 2011 Dec 27;11(1):108.

44. Christianson HC, Svensson KJ, Van Kuppevelt TH, Li JP, Belting M. Cancer cell exosomes depend on cell-surface heparan sulfate proteoglycans for their internalization and functional activity. Proc Natl Acad Sci U S A. 2013;110(43):17380–5.

45. Hunt L, Hacker DL, Grosjean F, De Jesus M, Uebersax L, Jordan M, et al. Low-temperature pausing of cultivated mammalian cells. Biotechnol Bioeng. 2005 Jan 20;89(2):157–63.

46. Mittelbrunn M, Gutiérrez-Vázquez C, Villarroya-Beltri C, González S, Sánchez-Cabo F, González MÁ, et al. Unidirectional transfer of microRNA-loaded exosomes from T cells to antigen-presenting cells. Nat Commun. 2011 Sep 19;2(1):282.

47. Chivet M, Javalet C, Laulagnier K, Blot B, Hemming FJ, Sadoul R. Exosomes secreted by cortical neurons upon glutamatergic synapse activation specifically interact with neurons. J. of Extracell Vesicles. 2014;3(1).

48. Lamichhane TN, Jay SM. Production of extracellular vesicles loaded with therapeutic cargo. Methods Mol Biol. 2018;1831:37–47.

49. Schneider DJ, Speth JM, Penke LR, Wettlaufer SH, Swanson JA, Peters-Golden M. Mechanisms and modulation of microvesicle uptake in a model of alveolar cell communication. J Biol Chem. 2017;292(51):20897–910.

50. Polanco JC, Li C, Durisic N, Sullivan R, Götz J. Exosomes taken up by neurons hijack the endosomal pathway to spread to interconnected neurons. Acta Neuropathol Commun. 2018;6(1):10.

51. Takov K, Yellon DM, Davidson SM. Confounding factors in vesicle uptake studies using fluorescent lipophilic membrane dyes. J Extracell Vesicles. 2017;6(1).

52. Pužar Dominkuš P, Stenovec M, Sitar S, Lasič E, Zorec R, Plemenitaš A, et al. PKH26

labeling of extracellular vesicles: Characterization and cellular internalization of contaminating PKH26 nanoparticles. Biochim Biophys Acta. 2018 Jun 1;1860(6):1350–61.

53. Chuo ST-Y, Chien JC-Y, Lai CP-K. Imaging extracellular vesicles: current and emerging methods. J Biomed Sci. 2018 Dec 24;25(1):91.

54. Ricklefs FL, Maire CL, Reimer R, Dührsen L, Kolbe K, Holz M, et al. Imaging flow cytometry facilitates multiparametric characterization of extracellular vesicles in malignant brain tumours. J Extracell Vesicles. 2019;8(1).

55. Mathieu M, Martin-Jaular L, Lavieu G, Théry C. Specificities of secretion and uptake of exosomes and other extracellular vesicles for cell-to-cell communication. Nat Cell Biol. 2019;21(1):9–17.

56. Toda Y, Takata K, Nakagawa Y, Kawakami H, Fujioka S, Kobayashi K, et al. Effective internalization of U251-MG-secreted exosomes into cancer cells and characterization of their lipid components. Biochem. Biophys. Res. Comm. 2014;456:768-773.

57. Svensson KJ, Christianson HC, Wittrup A, Bourseau-Guilmain E, Lindqvist E, Svensson LM, et al. Exosome Uptake Depends on ERK1/2-Heat Shock Protein 27 Signaling and Lipid Raft-mediated Endocytosis Negatively Regulated by Caveolin-1. J. of Bio Chem. 2013;288(24):17713-24.

58. Czernek L, Chworos A, Duechler M. The Uptake of Extracellular Vesicles is Affected by the Differentiation Status of Myeloid Cells. Scand J Immunol. 2015 Dec;82(6):506–14.

59. Pegtel DM, Cosmopoulos K, Thorley-Lawson DA, Van Eijndhoven MAJ, Hopmans ES, Lindenberg JL, et al. Functional delivery of viral miRNAs via exosomes. Proc Natl Acad Sci U S A. 2010 Apr 6;107(14):6328–33.

60. Hong S-B, Yang H, Manaenko A, Lu J, Mei Q, Hu Q. Potential of Exosomes for the Treatment of Stroke. Cell Transplant. 2019;28(6):662–70.

Figures:

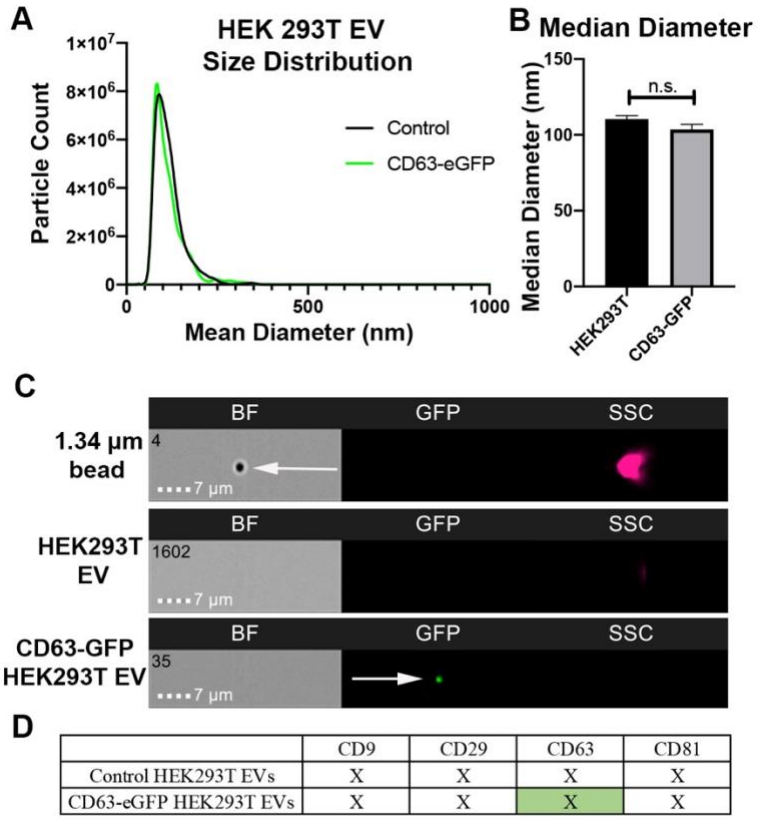

	CD9	CD29	CD63	CD81
Control HEK293T EVs	X	X	X	X
CD63-eGFP HEK293T EVs	X	X	X	X

Figure 2.1: **Characterization of HEK293T EVs tagged with CD63-eGFP.**

EVs were isolated from HEK293T (control) and HEK293T expressing CD63-eGFP cell culture media. **A.** Representative EV size distribution recorded via nanotracking software. **B.** Quantification of mean diameter distribution of transfected vs. non-transfected HEK293T EVs. **C.** IFC images of negative control beads, HEK293T control EVs, and CD63-eGFP tagged EVs. BF signifies Brightfield, GFP signifies green fluorescent protein (488nm excitation laser) and SSC signifies side scatter. Positive eGFP in GFP channel signifies fluorescent HEK293T EVs. **D.** Flow cytometry based MACSPlex surface marker expression of non-transfected HEK293T

EVs and HEK293T CD63-eGFP EVs. Both EV sources are positive for CD29, CD9, CD63, and CD81, as measured in relative fluorescence (denoted by X for positive). Bars represent mean ± SEM; N = 3; unpaired T-test. n.s. signifies p>0.05

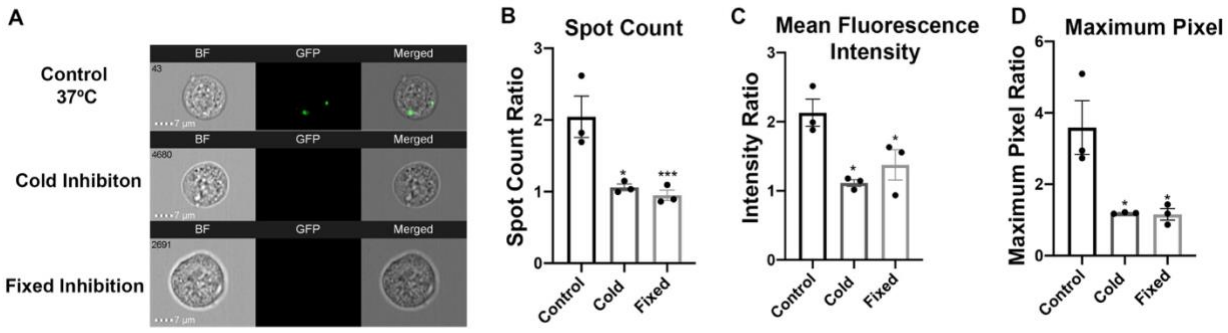

Figure 2.2: **EV internalization inhibition assays.**

HEK293T cells were co-cultured with HEK293T EVs under various conditions. Control (37°C) refers to co-culture in physiological 37°C environment. Cold refers to co-culture in a 4°C environment. Fixed inhibition refers to an assay where recipient cells were PFA fixed prior to co-culture. **A.** Representative IFC images of recipient cells. Column 1, BF, signifies bright field. Column 2, GFP, signifies green fluorescent protein (488nm excitation laser), and Column 3 signifies a merge of BF and GFP. Control shows positive GFP representing EV internalization. **B-D**. Quantification of inhibition assays compared to controls via spot count, mean fluorescence intensity, and maximum pixel. Bars represent mean ± SEM; N = 3; one-way ANOVA followed with Tukey's post hoc test compared to control. *p<0.05 ***p<0.01

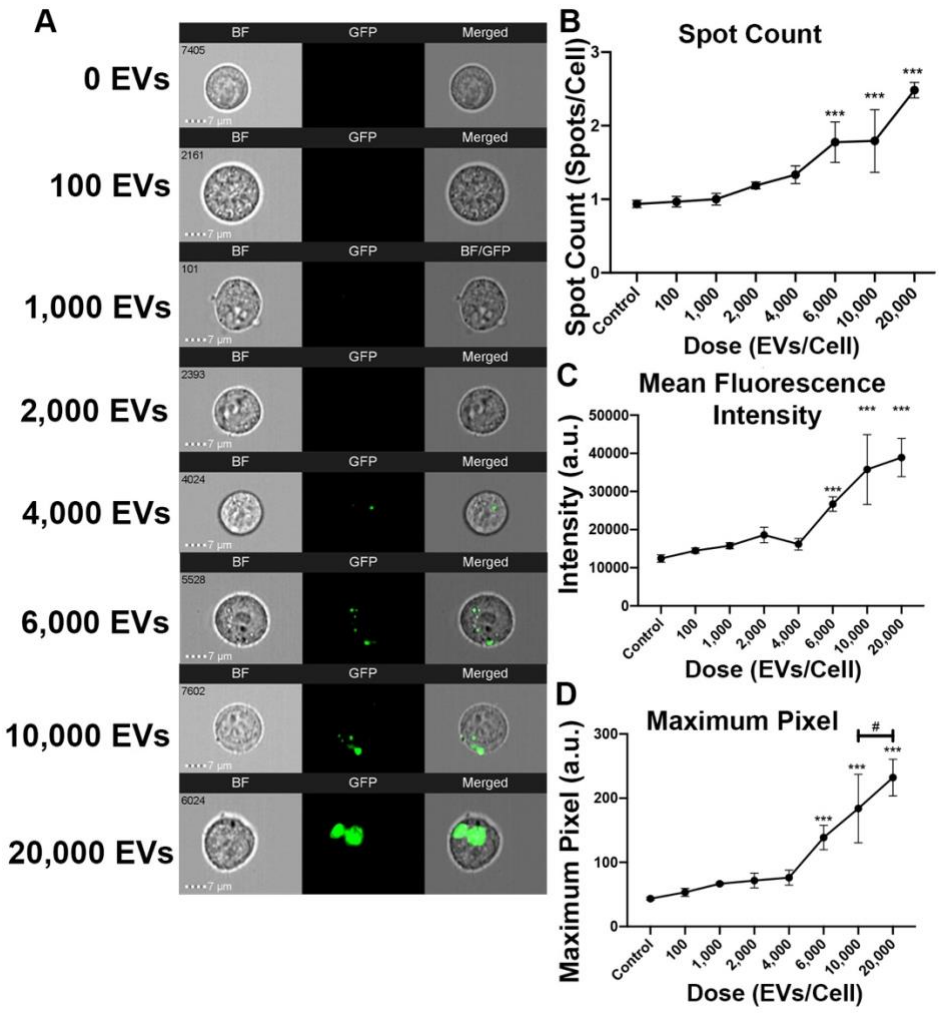

Figure 2.3: **HEK293T EV uptake has a dose effect with a minimum threshold of 6,000EVs.** HEK293T cells were co-cultured with HEK293T EVS at increasing doses from 0-20,000/cell. **A.** Representative IFC images of recipient cells with respective EV doses. GFP localization signifies HEK293T EV uptake. **B-D**. Quantification of dose assays compared to controls and each group via spot count, mean fluorescence intensity, and maximum pixel ratios. Bars represent mean ± SEM; N = 3; one-way ANOVA followed with Tukey's post hoc test. *p<0.05 ***p<0.01

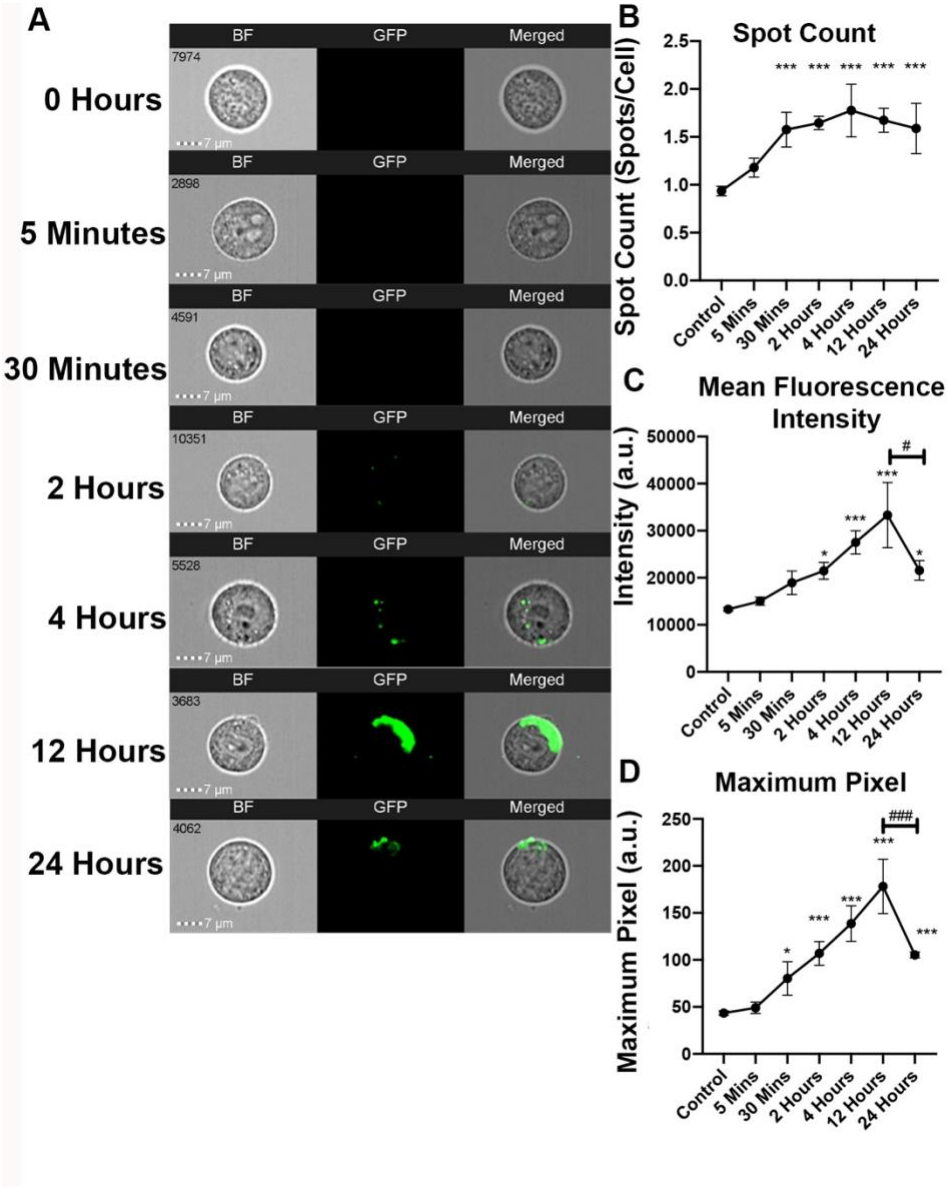

Figure 2.4: **HEK293T EV uptake is time dependent.**

HEK293T cells were co-cultured with 6,000 HEK293T EVs/cell for increasing lengths of time. **A.** Representative IFC images of recipient cells respectively. GFP localization signifies increased HEK293T EV uptake. **B-D**. Quantification of time course assays compared to controls and each group via spot count, mean fluorescence intensity, and maximum pixel ratios. Bars represent mean ± SEM; N = 3; one-way ANOVA followed with Tukey's post hoc test. *p<0.05 ***p<0.01

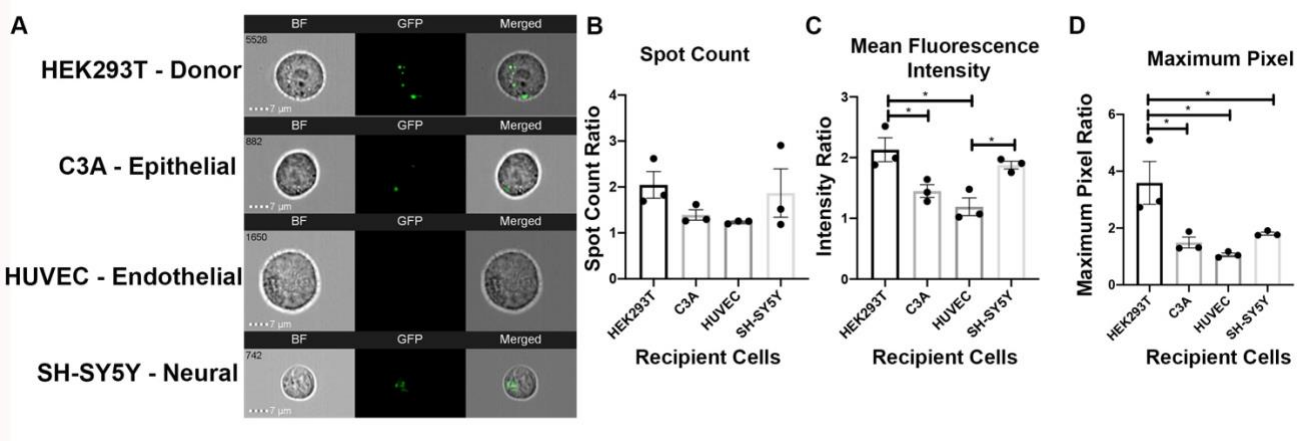

Figure 2.5: **HEK293T EVs display uptake preference to HEK293T cells.**

HEK293T EVs were co-cultured with HEK293T cells, C3A epithelial cells, human umbilical vein endothelial cells (HUVEC), and SY5Y neural cells. **A.** Representative IFC images of recipient cells co-cultured with HEK293T EVs. **B-D**. Quantification of EV uptake preference assays compared to controls and each other via spot count, mean fluorescence intensity, and maximum pixel ratios. Bars represent mean ± SEM; N = 3; one-way ANOVA followed with Tukey's post hoc test. *p<0.05 ***p<0.01

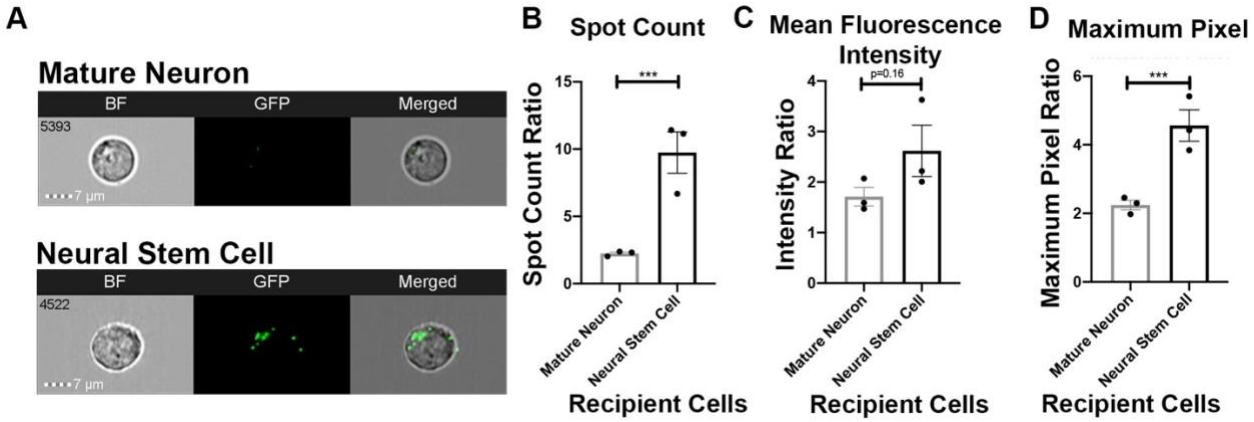

Figure 2.6: **Neural differentiation status affects HEK293T EV uptake.**

HEK293T EVs were co-cultured with mature human neurons and human neural stem cells. **A.** Representative IFC images of recipient cells co-cultured with HEK293T EVs. **B-D**.

Quantification of EV uptake preference assays compared to controls and each other via spot count, mean fluorescence intensity, and maximum pixel ratios.

Bars represent mean ± SEM; N = 3; unpaired T-Test. *p<0.05 ***p<0.01 compared to 0 EVs (control).

List of Abbreviations:

EV: extracellular vesicles, HEK293T: human embryonic kidney cell line, IFC: imaging flow cytometry, hNSC: human neural stem cell, GFP: green fluorescent protein, BF: brightfield, SSC: side scatter, ISEV: international society of extracellular vesicles

CHAPTER 3

EXTRACELLULAR VESICLE MEDIATED DELIVERY OF STAPLED PEPTIDES DISRUPTS THE OVERACTIVE LRRK2-FADD INTERACTION OF PARKINSON'S DISEASE[3]

[3] Brian J. Jurgielewicz, Leah G. Helton, Hardy Rideout, Eileen Kennedy, Yao Yao, Steven Stice. To Be Submitted in Molecular Therapy.

3.1 ABSTRACT

Overexpression of mutant Leucine Rich Repeat Kinase 2 (LRRK2) has been implicated to induce neuronal cell death contributing to the pathogenesis of Parkinson's Disease. The most common LRRK2 mutation, G2019S, activates the extrinsic death pathway through the binding of the adaptor protein FADD. Recently, it has been shown that the blocking of the armadillo region responsible for binding to FADD is neuroprotective. In this study, we have developed a novel protein-protein inhibitor peptide, FARM5, to disrupt the interaction of LRRK2 and FADD. However, synthetic peptides have poor cellular internalization and thus require high *in vitro* concentrations to interrupt the LRRK2-FADD binding, which inhibit clinical translatability of peptide therapeutics. We have developed a high throughput platform to load the FARM5 into HEK293T extracellular vesicles (EVs) to enhance its internalization into recipient cells, protection against proteases, and increase its overall functional efficacy. Our work shows that peptides can be passively loaded into HEK293T EVs and delivered into various disease relevant recipient cells at higher rates than naked peptide. Furthermore, EV mediated delivery of FARM5 peptide disrupted the LRRK2-FADD interaction with significantly lower concentrations than naked peptide alone. These results suggest that for the first time, EVs can be loaded with and improve the therapeutic efficacy of stapled peptides to treat LRRK2 mutation linked Parkinson's Disease.

3.2 INTRODUCTION

Leucine Rich Repeat Kinase 2 (LRRK2) mutations are the most common cause of genetically linked Parkinson's Disease (PD) and closely resemble clinical pathology of idiopathic PD [1–3]. The primary motor dysfunction of PD results from the substantial death of dopaminergic producing neurons in the substantia nigra-pars compacta (SNpc) [4–6]. Consisting of

51 exons, LRRK2 is a large protein of 2527 amino acids responsible for diverse cellular functions including neurite outgrowth, cytoskeletal maintenance, vesicle trafficking, autophagic protein degradation among others [4]. LRRK2 has multiple defined domains including a small GTPase like domain, Ras of complex proteins (ROC), a kinase domain, and other protein interaction domains including the ankyrin repeat domain and the armadillo region [4,7].

Aberrant LRRK function is caused by a missense mutation, specifically the G2019S substitution that results in an overexpression in intrinsic kinase activity and activation of FADD-dependent death pathways which leads to apoptotic cell death [5,8,9]. Previously, our group has shown that the armadillo region of LRRK2 interacts with FADD, an adaptor protein to recruit caspase-8 [8]. Though intrinsic binding of LRRK2 and FADD occurs, the mutant overexpressed LRRK2 hyperactivates the extrinsic death pathway and increases activity of Caspase-8 and key mitochondrial pro-apoptotic proteins, Bid and Bax [8]. To slow neuronal death, co-expression of fragments of LRRK2 that contain the FADD binding motif or deletion of this motif block the interaction with FADD and thus the extrinsic death pathway [8]. Downregulation of the caspase-8 upstream or blocking the ability of FADD to recruits caspase 8 prevents apoptotic death, a putative PD induced cell death mechanism [8]. Thus, LRRK2 mutations contribute to the neuronal cell death induced in Parkinson's Disease[7–9].

The FADD-LRRK binding region of the armadillo domain provides a therapeutic opportunity to inhibit the binding of LRRK2 and FADD and downregulate the extrinsic death pathway, while preserving the integrity of canonical LRRK2. Small peptide inhibitors are viable therapeutic options to disrupt this interaction. To stabilize and maintain an alpha-helical structure of the peptide inhibitors, we synthesized peptides to be conformationally constrained using a staple via the incorporation of an all-hydrocarbon bridge over a helical turn [10]. The stapled

'FARM' peptides specifically target the interaction of FADD and the ARMadillo region of LRRK2. In principle, the stapled peptide targets the protein-protein interfaces by providing an elongated binding surface that can bind to shallow protein surfaces[10]. Though promising, a major obstacle for effective intervention is how to efficiently deliver the charged small molecules across the blood brain barrier (BBB) and the recipient cell plasma membrane [11,12]. Despite the advances of hydrocarbon stapled peptides to enhance stability, the ability to cross plasma membranes is inefficient and dependent on the staple type and charge thus decreasing its efficacy [13]. Peptide therapeutics are susceptible to proteolytic breakdown and consequent clearance by the body when administered intravenously [10,14]. Thus, a delivery vector to enhance uptake is vital to increase the translational potential of peptide therapeutics.

To mitigate the inherent delivery challenges with peptides, we used extracellular vesicles (EVs), to protect and deliver peptides into recipient cells [15,16]. EVs are nanosized lipid bilayer bound vesicles released from most cells responsible for the delivery of proteins, lipids, and genetic material including DNA and RNA [16]. Notably, we and others have previously shown that EVs can cross the BBB and the plasma membrane to enter target neurons [17,18], and neural stem cells derived EVs had a therapeutic benefit via neuroprotection in a porcine stroke model [19–21]. Recently, EVs have been shown to effectively deliver therapeutic payloads including small interfering RNA (siRNA), mircoRNA (miRNA) and antisense oligonucleotides (ASOs) to the brain and modulate recipient cells [18,22–26]. These studies demonstrate therapeutic efficacy of EVs and protection of loaded biomolecules but many of the loading techniques, namely electroporation and sonication, are not scalable and may alter the physical characteristics of the loaded biomolecules and EVs [23,27]. As a passive loading alternative, siRNA has been modified to increase its hydrophobicity through a cholesterol tag to efficiently associated with the EV

membrane [23]. However, to our knowledge, EVs have not been utilized to enhance the uptake of peptide therapeutics.

In this study, we synthesized novel peptides that mimic the FADD region to inhibit the LRRK2 and FADD interaction to downregulate the extrinsic death pathway. After loading the peptide into HEK293T EVs using non-disruptive, high throughput, and scalable methods, loaded EVs more efficiently delivered the peptide to neural and vascular cells than peptide alone. Finally, EV delivery of novel peptides targeted and disrupted the FADD-LRRK2 interaction.

3.3 METHODS

Cell Culture

HEK293T cells (ATCC; Wesel, DE) were purchased cultured in DMEM (Sigma; MO, USA) with 10% fetal bovine serum, 100 U/mL penicillin, and 100 μg/mL streptomycin. HEK293T cells were thawed and plated at $1*10^6$ cells per 100mm plate for expansion. HEK293T cells were cultured for EV production and downstream assays. Differentiated neurons were kindly gifted by ArunA Bio, which were harvested cryopreserved after 28 DIV without FGF2 and cultured in AB2 media and ANS supplement (ArunaBio Inc; Athens, GA). Neurons were thawed directly into 6-well plate at $5*10^5$ cells per well. Human neurovascular cells, hCMEC/D3 (Sigma; MO, USA), thawed at $1*10^6$ cells per 100mm plate were cultured in EndoGRO-MV Culture media (Sigma; MO, USA), and grown on rat tail collagen. All cells were cultured under standard conditions at 37 °C, 5% CO_2.

Peptide Generation – A proprietary process developed at the Kennedy Lab at University of Georgia. Peptides were tagged with the fluorophore, 5-TAMRA (5 Carboxytetramethylrhodamine) isomer with an approximate excitation/emission maximum ~546/579 (ThermoFisher; Waltham, MA, USA).

Plasmids

Human LRRK2 cDNA with an N-terminal Flag epitope tag and full-length V5-tagged WT FADD was used as described [9]. Briefly, WT LRRK2 cDNA was sub-cloned into pcDNA3.1(+) plasmid with an N-terminal flag epitope. To introduce pathogenic PD-linked mutations, disease associated variants or functional mutations, the Quick change II site directed mutagenesis kit (Agilent Technologies; CA, USA) was used according to manufacturer's instructions [8,9]. Plasmids were kindly gifted by Dr. Hardy Rideout.

Extracellular Vesicle Isolation

HEK293T cells were cultured until around 80% confluency. Media was changed to standard HEK293T media without fetal bovine serum and collected for 3 consecutive days. As previously described [20,28], spent media was filtered through a 0.22-μm filter and enriched by ultrafiltration using Amicon Filters, 100-kDa regenerated cellulose centrifugal filter units (Millipore Sigma, Burlington MA). Amicon filters were primed with chilled PBS- -, ultracentrifuged at 2,000G for 10 minutes, and flow through was discarded. Up to 15mLs of spent media were added into the filter units, ultracentrifuged at 4,000G for 20 minutes, and flow through was discarded. This process was repeated for 30mLs total per filter unit. Filters were rinsed with 15mLs PBS and ultracentrifuged for 20 minutes at 2,000G. Filters were washed to resuspend EVs with up to 1mL PBS. Suspended EVs in PBS were aliquoted into 500uL samples to avoid recurring freeze/thaw. Concentration and size distributions of EVs were measured on Nanosight NS300 by the manufacturer's protocol (Malvern, UK).

Extracellular Vesicle Loading

EVs were mixed with 10μM TAMRA-fluorescent FARM5 peptides in PBS- -. EVs were diluted to a concentration of $2*10^{10}$ vesicles per mL and incubated with varying volumes of peptide. The

total volume of peptide and EVs was standardized to 500μL and incubated at 37 °C for 90 minutes with shaking at 500 RPM. EVs were pelleted by ultracentrifugation for 1 hour at 100,000g, 4 °C. Unloaded peptide remained in the supernatant and peptide-loaded EVs in the pellet and later resuspended in 200μL of PBS- -.

Loading Quantification

The TAMRA fluorescence pellet containing peptide loaded EVs and the supernatant with unloaded peptide were measured in a Costar UV-transparent, flat-bottom 96-well plate (Corning; #3635) using SpectraMax iD5 (Molecular Devices; San Jose, CA, USA). A calibration curve was generated using known concentrations of peptide and created using Prism statistical software (Graphpad; San Diego, CA, USA). The loading efficiency was calculated by the percent difference between the total amount of peptide molecules originally added to the EV sample and the amount of peptide remaining in the pellet after exosome incubation and ultracentrifugation. Further, number of EVs with positive fluorescence was approximated using imaging flow cytometry.

EV Uptake

Recipient cell lines were seeded at 60% confluency in a 6-well plate for 24 h under standard culture conditions of 37°C and 5% CO_2. Standard media was changed to fetal bovine serum-free (FBS−) media before co-culture for each cell line. Loaded EVs, naked peptide, or PBS-, were administered to cells and co-cultured for 4 hours at 37°C. 200μL of the EV loaded sample added into each well. The amount of naked peptide was matched to the amount of peptide loaded into the HEK293T EVs (See EV Loading). After co-culture, cells were resuspended in 5% trypsin or Acutase (Sigma, MO, USA) for mature neurons and concentrated to one million cells per 50 μL for flow cytometry.

Imaging Flow Cytometry

Acquisition was performed on the ImageStreamX Mark II Imaging Flow Cytometer (Luminex Corporation, Austin, TX) using the INSPIRE software. As previously described in [28,29], a minimum of 5,000–10,000 cell events were acquired for each technical replicate. Briefly, each biological sample was replicated in three technical replicates and individually acquired on the ISx. Bright field images were collected on channel one and side scatter (785 nm) on channel six. TAMRA fluorescence was excited by 561 nm laser at 150 mW, and fluorescence was collected on channel three (560 - 595 nm). A magnification of 60× was used along with a low acquisition rate for high sensitivity. Cell gating was adjusted for focus via Gradient RMS and cellular size based on Area and Aspect Ratio. For EV characterization, loaded and non-loaded EVs were resuspended in PBS- and acquired on the ISx at full concentration followed by serial dilutions. Each acquisition was done for a minimum of one minute and all events were collected with speed beads ON. Bright field camera was on, 561 laser was set to high at 200mW, and side scatter set to 5mW [30,31].

IDEAS Analysis – Cell Uptake and EV Characterization

Data and image analyses were conducted using the IDEAS software (Luminex; Austin, TX), as previously described in [28,29]. Initial gating occurred during INSPIRE acquisition to eliminate cell debris and control speed beads. Focus gate eliminated cells that were not in the field of focus using the Gradient RMS value. Focused cells were then gated to eliminate doublets and cell debris using area bright field vs. aspect ratio bright field. Gated data were used to create histograms and generate statistic references measuring fluorescence intensity (sum of all pixels in an image), maximum pixel intensity (intensity of the brightest pixels in an image). For EV only, speed beads were gated out in high side scatter intensity, TAMRA+ was gated for ‘not

speed beads. Further, fluorescent EVs were gated by Low Side Scatter and Positive Fluorescence in Channel 3 (EV analysis based on [30–32].

Co-Immunoprecipitation Assay

Based on previous studies [8,9], in a 6-well plate, HEK293T cells were transfected simultaneously at a 4:1 ratio with V5_FADD and Flag_LRRK2 via JetPEI according to manufacturer's protocol (PolyPlus Transfection, NY, USA). After ~36 hours of transfection, cells are treated with naked peptide or EV loaded peptide for 8 hours at varying concentrations. The cells were then washed in cold PBS, pelleted, and resuspended in IP lysis buffer and incubated for 30 minutes (20mM Hepes, pH 7.4; 150mM NaCl; 0.1% NP-40; 2mM EGTA; 2mM MGCL2; 10% glycerol, pH 7.2; phosphatase inhibitor cocktail and protease inhibitors). Cells were disrupted by a Dounce glass homogenizer and clarified by centrifugation at 13,000RPM for 15 minutes at 4°C. The lysate was incubated with Anti-Flag M2 Magnetic beads (M8823) for 12 hours. Beads were then washed 3-5x in 2X Laemmli/SDS sample buffer for 5 minutes. Samples were separated by SDS-PAGE. Blotted membranes were blocked with 5% non-fat milk and incubated with primary antibodies.

Statistical Methods

Statistics were done via GraphPad Prism 8.1.2 (Graphpad; San Diego, California) in triplicates. The data are presented as mean ± standard error of the mean (SEM). Statistical significance was determined using an unpaired *T* test or a one-way analysis of variance (ANOVA) with Tukey's or Dunnett's multiple comparison post hoc compared when appropriate. $p < 0.05$ was considered significant.

3.4 RESULTS

FARM5 Peptide Identification and Synthesis

Computer generated alpha-helical structure elucidated the predicted binding interface between LRRK2 and FADD (Figure 3.1A). The FADD-DD binding region to the LRRK2 ARM region is the targeted site of disruption. We designed a peptide to mimic the helical conformation of the corresponding FADD region using solid phase peptide synthesis (Figure 3.1B). The FARM5 peptide inhibitors are conformationally constrained using peptide 'stapling' to stabilize and maintain an alpha-helical structure through incorporation of an all-hydrocarbon bridge over a helical turn (Figure 3.1B). Using a co-expression assay we screened five different stapled peptides to assess the capacity of each to inhibit the interaction between LRRK2 and full length FADD while preserving the canonical activities of LRRK2 (Figure 3.1C). F5 was selected for downstream assays due to its inhibition activity between LRRK2 and FADD.

Dose Optimization of Peptide Loading dose into HEK293T EVs

Ultrafiltration prior to loading resulted in standard HEK293T EVs size and distribution (Figure 3.2A-B) with a mean diameter of 180nm (Figure 3.2C). After loading, average EV size was compared showing that a dose of 100,000 molecules of peptide per EV significantly increased the particle size above 200nm ($p=0.02$), whereas the 50,000 and 200,000 molecules per EV doses did not significantly affect the mean diameter ($p=0.3$, $p=0.54$) (Figure 3.2C).

Loading efficiency was calculated by comparing the EV pellet fluorescence to the inputted amount of peptide into the solution. 50,000 molecules of peptide per EV inputted yielded a loading efficiency of 9% which equated to around 4,650 molecules per EV loaded. When comparing the low dose of 10,000 molecules / EV to 50,000 EVs there were significantly more molecules with the 50,000 molecule / EV dose ($p=0.014$). Further increasing the input

dosage to 100,000 and 200,000 molecules per EV slightly increased the amount of peptide into the EVs to 5,600 and 6,200 compared to the 10,000 molecule / EV dose ($p=0.011$, $p=0.004$), but were associated with large decreases in loading efficiency to 5.6 and 3.1% respectively (Figure 2D-E). When comparing molecules per EV loaded, there were no significant differences between 50,000 and the higher doses ($p=0.71$, $p=0.36$) suggestive of a possible tapering or saturation of peptide loading. Thus, for scalable therapeutic applications, 50,000 molecules per EV represents an optimal dose to maintain moderate efficiency with an increase in amount of peptide in each EV for downstream assays.

Imaging Flow Cytometry Assays of EV Loading

An imaging flow cytometry based assay was developed to further characterize loading of FARM5 into HEK293T EVs by generating paired qualitative images with quantitative measures of fluorescently loaded extracellular vesicles. In the brightfield (BF) channel and the side scatter channel, extracellular vesicles are not detected (Figure 3.3A). Further, there are minimal visible positive events in the TAMRA fluorescent channel for non-loaded EVs and other negative controls (Figure 3.3A). The 1.35um beads are positive in BF and SSC, with minimal autofluorescence (Figure 3.3A). Peptide only and non-loaded EVs did not register in the TAMRA channel (Figure 3.3A) with minimal mean fluorescence intensity due to potential false positives or peptide aggregation (Figure 3.3C).

When assessing concentration of EVs in ‘objects per mL’ recorded via the ISx, the negative controls are nearly zero (Figure 3.3B). The fluorescent tag on the peptide is visible when loaded into EVs in all doses ranging from 10,000 molecules of peptide per EV through 200,000 (Figure 3.3B). Compared to peptide only, non-loaded and 10,000 molecules per EV dose did not significantly differ in positive fluorescence concentration ($p>0.999$, $p=0.5431$). At

higher doses, 25-100,000 molecules per EV had significantly increased positive fluorescent concentration to peptide only ($p=0.0003$, $p<0.0001$ for other comparisons). 50,000 molecules of peptide per EV resulted in $1.27*10^8$ loaded EVs/mL, 100,000 at $1.37*10^8$ EVs/mL, and 200,000 at $2.89*10^8$ loaded EVs/mL suggesting that increasing concentration of peptide may result in more EVs loaded with FARM5. Compared to peptide only controls, 10,000 ($p=0.0005$), 25,000 ($p=0.003$), and 50,000, 100,000 and 200,000 ($p<0.0001$) molecules of peptide per EV increased mean fluorescence values. When comparing between 50,000 vs. 100,000 ($p=0.91$), 50,000 vs. 200,000 ($p>0.99$), there were no statistical differences. Thus, it can be implied that there was a saturation effect of loading EVs when using fluorescence as the key metric.

EV Mediated FARM5 Delivery into Disease Relevant Recipient Cells

To assess the benefits of EV mediated delivery and internalization into recipient cells of the FARM5 peptide, EVs and naked peptide were co-cultured with cell lines including HEK293T, mature neurons, and neurovascular cells. In HEK293T recipient cells, minimal naked peptide is visualized in the Farm5 channel, whereas there are fluorescently tagged peptides internalized into the cell (Figure 3.4A). EV mediated delivery has a higher intensity, 24,446 compared to 13,753 ($p=0.18$) (Figure 3.4B) and maximum pixel, 111 compared to 46.89 ($p=0.15$) (Figure 3.4C) suggesting an enhanced uptake compared to naked EV. Similarly in neurovascular cells, the EV delivered peptide has visual fluorescence (Figure 3.4D) and supported quantitively by higher intensity 26,283 compared to 12,9111 ($p=0.012$) (Figure 3.4E) and maximum pixel, 173.7 compared to 59.87 ($p=0.005$) (Figure 4F). Visually, mature neurons have internalized naked peptide with slight increases in EV mediated delivery (Figure 3.4G). EV delivery compared to naked peptide had increased maximum pixel 69.83 compared to 45.14

(p=0.002) and trending increases in intensity 11,197 compared to 8,961 (p-0.085) further supporting higher internalization of peptide via EV delivery (Figure 3.4I).

Co-Immunoprecipitation of LRRK2 and FADD

Co-immunoprecipitation assays were conducted to evaluate the potential of EV mediated delivery of FARM5 to disrupt the LRRK2 and FADD interaction and henceforth inhibit the activation of the extrinsic death pathway (Figure 3.5A). The non-transfected column showed marginal endogenous LRRK2 binding to FADD, whereas the transfected cells with no treatment has a strong FADD indication (Figure 3.5B). When administering FARM5 peptide to transfected HEK293T cells at high *in vitro* concentrations the interaction is completely disrupted at 10uM and partially disrupted at 5uM. When FARM5 is loaded with EVs, we estimate the concentration (Methods) to be around 50nM, and it results in an efficient knockdown of the LRRK2-FADD interaction comparable to between 5uM and 10uM of naked peptide. This suggests that EV mediated delivery of the FARM5 peptide has potentially higher efficacy at lower doses compared to naked peptide alone, thereby supporting the utility of EVs as delivery vectors for therapeutic peptides.

3.5 DISCUSSION

The G2019S mutation in the LRRK2 gene leads to overexpression and enhanced binding between LRRK2 and the death adaptor protein FADD which in turn over activates the extrinsic death pathway and apoptotic cell death [8]. Patients with Parkinson's Disease demonstrate accelerated neuronal cell death with mutant LRRK2 due to the FADD-LRRK2 interaction [33].Thus, interrupting this interaction could lead to decreases in neuronal cell death in Parkinson's Disease. Herein, we have designed and synthesized a neuroprotective hydrocarbon constrained, stapled peptide, that acts as a protein-protein interface disrupter of the LRRK2 and FADD. We

further enhanced the peptide efficacy through EV mediated delivery and uptake in target cells *in vitro*. Using this targeted approach, the canonical features of LRRK2 including its kinase and GTPase activities remain functional while particularly slowing the apoptotic cell death [6]. However, synthetic peptides alone are not viable therapeutics due to poor permeability and biodistribution [10,13].

Since EVs functionally modulate recipient cells, EVs have been exploited for their protective capacity of cargoes and ability to deliver at high rates into recipient cells [16,34–37]. To date, the majority of studies harnessing EVs as delivery vectors have used small RNA species including siRNAs and ASOs [18,22,24,38], but not peptides. Not only do EVs provide protection of the therapeutic cargoes, but also have been documented to cross the blood brain barrier and enter into neurons [17,18,39,40]. Building upon this foundation, we have loaded novel stapled peptides into HEK293T EVs to disrupt the overactive extrinsic death pathway in Parkinson's Disease. Our ultimate aim was to develop a therapeutic modality delivered and protected by EVs to decelerate the apoptotic cell death in Parkinson's Disease.

The major challenge of creating effective peptide therapeutics is their poor ability to cross physiological barriers including the plasma membrane of recipient cells [10,13]. Therefore, increasing their uptake into targeted neurons should permit a lower required dose to inhibit the LRRK2-FADD interaction. As shown in our previous studies, HEK293T EVs are internalized by HEK293T cells along with significant uptake into mature neuronal subtypes [28]. Herein, we assayed EV delivery and uptake into disease relevant cells compared to matched controls *in vitro* of naked peptide and showed that EV mediated delivery of peptide delivered significantly higher quantities. Since the major hurdle of delivering neurological therapeutics is crossing the blood brain barrier and targeted cells are dopaminergic neurons [40,41], recipient cells included

neurovascular cells and differentiated neurons. EVs correspondingly have been hypothesized to traverse the BBB via transcytosis, so positive internalization of the loaded EVs provides confidence with translational applicability [42,43]. Often when assessing peptide uptake, the common dose is 10μM to assess efficacy, however we estimate a significantly lower dose approximately 50nM when delivered by EVs. The lower required dose and targeted uptake of the stapled peptides into recipient cells may decrease potential off target or toxic side effects [44]. The lower required dose thereby can increase the translational potential when scaling up peptide synthesis for *in vivo* models. Ultimately, the increased uptake of peptide mediated by EVs provides long-term value in safety, translatability, and efficacy of peptide therapeutics.

Despite the recent advancements of loading EVs with exogenous therapeutics, methods of loading EVs are not standardized and often are low throughput, have low efficiency, or disrupt the EV membrane [35,38]. Electroporation of EV and siRNA mixtures resulted in an overabundance of siRNA aggregates causing extensive amounts of false positive loading [27]. Several studies have shown that to passively load EVs with siRNA, a cholesterol tag which enriches the siRNA hydrophobicity, successfully increases the association of EVs with siRNA [23,45]. However, the siRNA molecules are then attached to the EVs external surface and may lack the protective capacity provided by the EV membrane [23]. As the first group to do so, we have shown that passively loading EVs with the small, stapled peptides through simple co-incubation is viable and an efficient and reproducible method of loading EVs. The simplicity and high throughput nature of our techniques should accelerate progress in utilizing EVs to deliver stapled peptides.

Our passive loading method allows for control of inputted concentration of both EVs and peptide while resulting in sufficient loading values. Similar to a passive technique using hydrophobically modified siRNA where 1-3,000 molecules of siRNA per EV was observed [23,45],

we recorded between 2-6,000 molecules / EV with similar loading efficiencies of around 5-10%. Though others have noted loading of 10-50%, we observed consistent and repetitive results around 10% efficiency suggesting that our techniques of post-loading cleanup and quantification are sufficient [23]. We have also shown a dose dependent increase when increasing the concentration of peptide while maintaining EV concentration followed with a plateau effect. Thus, we surmise that the EVs are saturated with peptide at around 5,000 molecules per EV and increasing concentration leads to decreases in loading efficiency with minimal increases in peptide loading.

Advancing beyond the standard of quantifying loading efficiencies using a plate reader, we further optimized the imaging flow cytometry based platform to support our initial loading data and to evaluate EV uptake. As compared to plate reader assessment of percent of peptide loaded into EVs, imaging flow cytometry elucidates the concentration of extracellular vesicles with the fluorescently loaded with peptide [31]. These measures together provide more insights into loading of peptide into EVs and optimizing the efficiencies. Previous studies have shown that imaging flow cytometry is capable of detecting fluorescent nanoparticles as small as 100nm, but also eGFP tagged EVs [28,31]. IFC is advantageous due to its ability to capture nanosized particles visually, along with providing the quantitative and high throughput attributes of standard flow cytometry [28,30,31,46]. Herein, we are the first group to evaluate EV loading using IFC. IFC further supported that HEK293T EVs are loaded with fluorescently tagged peptide in a dose dependent manner with a possible saturation effect. By measuring mean fluorescence intensity, IFC analysis showed that EV loading can be quantified in a high-throughput manner which advances the standard loading quantification techniques while providing visual signal of loaded EVs.

To assess the functionality of the naked and EV mediated delivery of FARM5 peptide as a protein-protein inhibitor, we transfected HEK293T cells with LRRK2 and FADD. This model has been previously utilized to recapitulate the LRRK2-FADD interaction in dopaminergic neurons in Parkinson's Disease [8,47,48], Notably, we showed that the EV mediated delivery of FARM5 disrupted FADD-LRRK2 binding at greater rates than highly concentrated naked peptide. This data suggests not only that EVs have higher uptake efficiency into mutant recipient cells most commonly via endocytosis, but that it can functionally deliver higher quantities to the appropriate intracellular regions as compared to naked peptide [49–51]. The increased knockdown efficiency of peptide delivery is a promising proof of principle outcome showing that EVs can be efficiently harnessed to deliver peptide therapeutics for the treatment of LRRK2 Parkinson's Disease.

3.6 REFERENCES

1. Haugarvoll, K. *et al.* Lrrk2 R1441C parkinsonism is clinically similar to sporadic Parkinson disease NIH Public Access. *Neurology* **70**, 1456–1460 (2008).
2. Paisán-Ruiz, C., Lewis, P. A. & Singleton, A. B. LRRK2: Cause, risk, and mechanism. *Journal of Parkinson's Disease* vol. 3 85–103 (2013).
3. Yue, M. *et al.* Progressive dopaminergic alterations and mitochondrial abnormalities in LRRK2 G2019S knock in mice HHS Public Access. *Neurobiol Dis* **78**, 172–195 (2015).
4. Rideout, H. J. & Stefanis, L. The neurobiology of LRRK2 and its role in the pathogenesis of Parkinson's disease. *Neurochemical Research* vol. 39 576–592 (2014).
5. Rui, Q., Ni, H., Li, D., Gao, R. & Chen, G. The Role of LRRK2 in Neurodegeneration of Parkinson Disease. *Curr. Neuropharmacol.* **16**, 1348–1357 (2018).
6. Zhao, Y. & Dzamko, N. Recent Developments in LRRK2-Targeted Therapy for

Parkinson's Disease. *Drugs* **79**, 1037–1051 (2019).

7. Ho, C. C. Y., Rideout, H. J., Ribe, E., Troy, C. M. & Dauer, W. T. The Parkinson disease protein leucine-rich repeat kinase 2 transduces death signals via Fas-associated protein with death domain and caspase-8 in a cellular model of neurodegeneration. *J. Neurosci.* **29**, 1011–1016 (2009).
8. Antoniou, N. *et al.* A motif within the armadillo repeat of Parkinson's-linked LRRK2 interacts with FADD to hijack the extrinsic death pathway. *Sci. Rep.* **8**, 1–17 (2018).
9. Melachroinou, K. *et al.* Activation of FADD-Dependent neuronal death pathways as a predictor of pathogenicity for LRRK2 mutations. *PLoS One* **11**, (2016).
10. Ali, A. M., Atmaj, J., Van Oosterwijk, N., Groves, M. R. & Dömling, A. Stapled Peptides Inhibitors: A New Window for Target Drug Discovery. *Computational and Structural Biotechnology Journal* vol. 17 263–281 (2019).
11. Zheng, M., Huang, M., Ma, X., Chen, H. & Gao, X. Harnessing Exosomes for the Development of Brain Drug Delivery Systems. *Bioconjugate Chemistry* vol. 30 994–1005 (2019).
12. Dong, X. Current strategies for brain drug delivery. *Theranostics* vol. 8 1481–1493 (2018).
13. Chu, Q. *et al.* Towards understanding cell penetration by stapled peptides. *Medchemcomm* **6**, 111–119 (2015).
14. Jenssen, H. & Aspmo, S. I. Serum stability of peptides. *Methods in Molecular Biology* vol. 494 177–186 (2008).
15. Raposo, G. & Stoorvogel, W. Extracellular vesicles: Exosomes, microvesicles, and friends. *Journal of Cell Biology* vol. 200 373–383 (2013).

16. O'Brien, K., Breyne, K., Ughetto, S., Laurent, L. C. & Breakefield, X. O. RNA delivery by extracellular vesicles in mammalian cells and its applications. *Nature Reviews Molecular Cell Biology* vol. 21 585–606 (2020).

17. Sun, M. K. *et al.* Extracellular vesicles mediate neuroprotection and functional recovery after traumatic brain injury. *J. Neurotrauma* neu.2019.6443 (2019) doi:10.1089/neu.2019.6443.

18. Alvarez-Erviti, L. *et al.* Delivery of siRNA to the mouse brain by systemic injection of targeted exosomes. *Nat. Biotechnol.* **29**, 341–345 (2011).

19. Webb, R. L. *et al.* Human Neural Stem Cell Extracellular Vesicles Improve Tissue and Functional Recovery in the Murine Thromboembolic Stroke Model. *Transl. Stroke Res.* **9**, 530–539 (2018).

20. Webb, R. L. *et al.* Human Neural Stem Cell Extracellular Vesicles Improve Recovery in a Porcine Model of Ischemic Stroke. *Stroke* **49**, 00–00 (2018).

21. Spellicy, S. E. *et al.* Neural Stem Cell Extracellular Vesicles Disrupt Midline Shift Predictive Outcomes in Porcine Ischemic Stroke Model. *Transl. Stroke Res.* (2019) doi:10.1007/s12975-019-00753-4.

22. Ohno, S. I. *et al.* Systemically injected exosomes targeted to EGFR deliver antitumor microrna to breast cancer cells. *Mol. Ther.* **21**, 185–191 (2013).

23. Didiot, M. C. *et al.* Exosome-mediated delivery of hydrophobically modified siRNA for huntingtin mRNA silencing. *Mol. Ther.* **24**, 1836–1847 (2016).

24. Usman, W. M. *et al.* Efficient RNA drug delivery using red blood cell extracellular vesicles. *Nat. Commun.* **9**, 2359 (2018).

25. Shtam, T. A. *et al.* Exosomes are natural carriers of exogenous siRNA to human cells in

vitro. *Cell Commun. Signal.* **11**, 88 (2013).

26. Wahlgren, J. *et al.* Plasma exosomes can deliver exogenous short interfering RNA to monocytes and lymphocytes. *Nucleic Acids Res.* **40**, (2012).

27. Kooijmans, S. A. A. *et al.* Electroporation-induced siRNA precipitation obscures the efficiency of siRNA loading into extracellular vesicles. *J. Control. Release* **172**, 229–238 (2013).

28. Jurgielewicz, B., Yao, Y. & Stice, S. Kinetics and Specificity of HEK293T Extracellular Vesicle Uptake using Imaging Flow Cytometry. *Nanoscale Res. Lett.* **15**, (2020).

29. Ofir-Birin, Y. *et al.* Monitoring extracellular vesicle cargo active uptake by imaging flow cytometry. *Front. Immunol.* **9**, 1011 (2018).

30. Ricklefs, F. L. *et al.* Imaging flow cytometry facilitates multiparametric characterization of extracellular vesicles in malignant brain tumours. *J. Extracell. Vesicles* **8**, (2019).

31. Görgens, A. *et al.* Optimisation of imaging flow cytometry for the analysis of single extracellular vesicles by using fluorescence-tagged vesicles as biological reference material. *J. Extracell. Vesicles* **8**, (2019).

32. Tertel, T. *et al.* <scp>High-Resolution</scp> Imaging Flow Cytometry Reveals Impact of Incubation Temperature on Labeling of Extracellular Vesicles with Antibodies. *Cytom. Part A* cyto.a.24034 (2020) doi:10.1002/cyto.a.24034.

33. Rideout, H. J. & Stefanis, L. The neurobiology of LRRK2 and its role in the pathogenesis of Parkinson's disease. *Neurochemical Research* vol. 39 576–592 (2014).

34. Valadi, H. *et al.* Exosome-mediated transfer of mRNAs and microRNAs is a novel mechanism of genetic exchange between cells. *Nat. Cell Biol.* **9**, 654–659 (2007).

35. De Jong, O. G. *et al.* Drug Delivery with Extracellular Vesicles: From Imagination to

Innovation. *Acc. Chem. Res.* **52**, 1761–1770 (2019).

36. Murphy, D. E. *et al.* Extracellular vesicle-based therapeutics: natural versus engineered targeting and trafficking. *Experimental and Molecular Medicine* vol. 51 1–12 (2019).

37. Sancho-Albero, M., Ana Medel-MartínezMartínez ac, ab & MartínMartín-Duque, P. Use of exosomes as vectors to carry advanced therapies. (2020) doi:10.1038/s41929-019-0333-4.

38. Jiang, L., Vader, P. & Schiffelers, R. M. Extracellular vesicles for nucleic acid delivery: Progress and prospects for safe RNA-based gene therapy. *Gene Ther.* **24**, 157–166 (2017).

39. Banks, W. A. *et al.* Transport of extracellular vesicles across the blood-brain barrier: Brain pharmacokinetics and effects of inflammation. *Int. J. Mol. Sci.* **21**, 1–21 (2020).

40. Chen, C. C. *et al.* Elucidation of Exosome Migration Across the Blood–Brain Barrier Model In Vitro. *Cell. Mol. Bioeng.* **9**, 509–529 (2016).

41. Shahjin, F., Chand, S. & Yelamanchili, S. V. Extracellular Vesicles as Drug Delivery Vehicles to the Central Nervous System. doi:10.1007/s11481-019-09875-w.

42. Banks, W. A. *et al.* Transport of Extracellular Vesicles across the Blood-Brain Barrier: Brain Pharmacokinetics and Effects of Inflammation. *Int. J. Mol. Sci. Artic.* doi:10.3390/ijms21124407.

43. Saint-Pol, J., Gosselet, F., Duban-Deweer, S., Pottiez, G. & Karamanos, Y. Targeting and Crossing the Blood-Brain Barrier with Extracellular Vesicles. *Cells* **9**, 851 (2020).

44. Bruno, B. J., Miller, G. D. & Lim, C. S. Basics and recent advances in peptide and protein drug delivery. *Therapeutic Delivery* vol. 4 1443–1467 (2013).

45. Biscans, A. *et al.* Hydrophobicity of Lipid-Conjugated siRNAs Predicts Productive Loading to Small Extracellular Vesicles. *Mol. Ther.* **26**, 1520–1528 (2018).

46. Lannigan, J. & Erdbruegger, U. Imaging flow cytometry for the characterization of extracellular vesicles. *Methods* **112**, 55–67 (2017).

47. Melachroinou, K. *et al.* Activation of FADD-Dependent neuronal death pathways as a predictor of pathogenicity for LRRK2 mutations. *PLoS One* **11**, e0166053 (2016).

48. Melachroinou, K. *et al.* Elevated In Vitro Kinase Activity in Peripheral Blood Mononuclear Cells of Leucine-Rich Repeat Kinase 2 G2019S Carriers: A Novel Enzyme-Linked Immunosorbent Assay–Based Method. *Mov. Disord.* **35**, 2095–2100 (2020).

49. Joshi, B. S., de Beer, M. A., Giepmans, B. N. G. & Zuhorn, I. S. Endocytosis of Extracellular Vesicles and Release of Their Cargo from Endosomes. *ACS Nano* **14**, 4444–4455 (2020).

50. Mulcahy, L. A. *et al.* Routes and mechanisms of extracellular vesicle uptake. *J. Extracell. Vesicles* **3**, (2014).

51. McKelvey, K. J., Powell, K. L., Ashton, A. W., Morris, J. M. & McCracken, S. A. Exosomes: Mechanisms of Uptake. *J. Circ. biomarkers* **4**, 7 (2015).

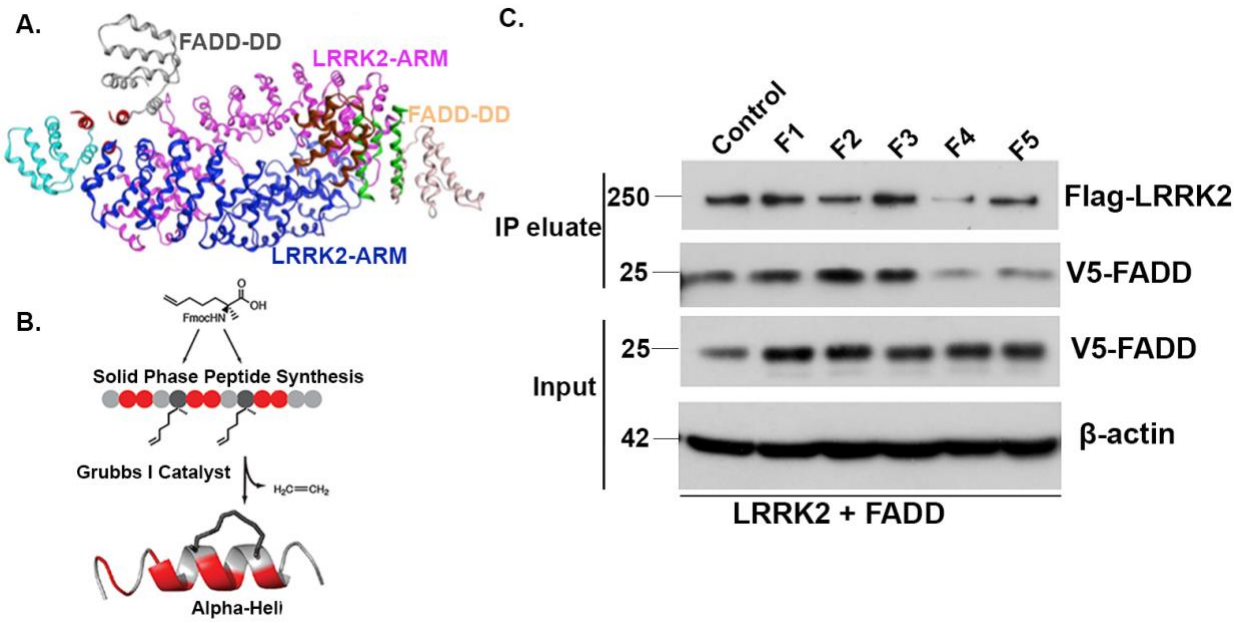

Figure 3.1: FARM5, Protein-protein inhibitor background, synthesis, and structure

(A) A structural model of the LRRK2-ARM region and the DD of FADD showing the predicted binding interface between LRRK2 and FADD (B) A schematic of the synthesis of the stapled alpha helical peptide using solid phase peptide synthesis. (C) Co-immunoprecipitation screen of peptide inhibitors for the interaction of LRRK2 and FADD. LRRK2 was bound to FLAG and V5 to FADD. F4 and F5 displayed decreased Flagg and LRRK2 interaction. Beta-actin was the positive control.

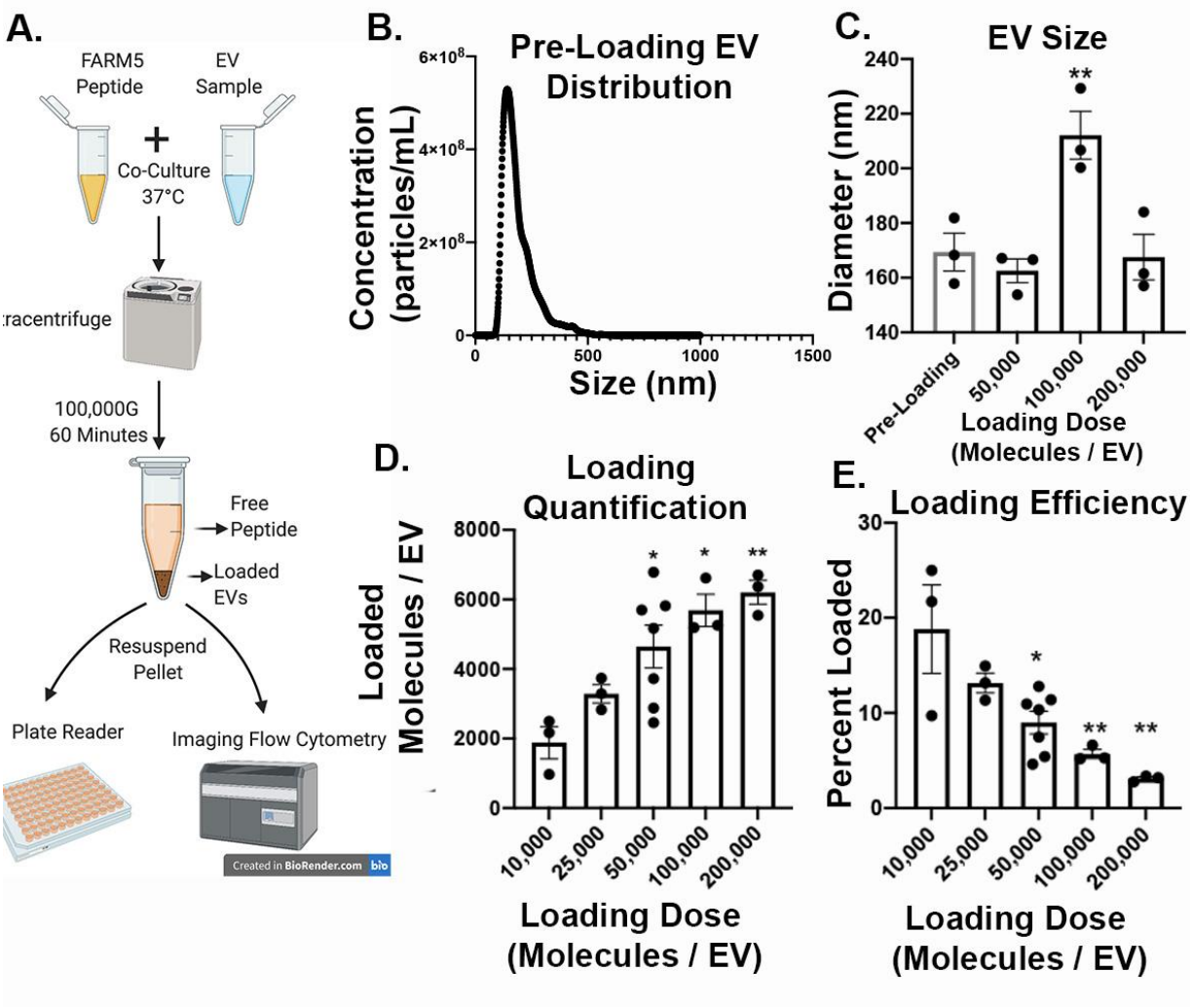

Figure 3.2: Passive loading of FARM5 peptide into HEK293T EVs

(A) Schematic of the workflow of peptide loading with HEK293T EVs. HEK293T EVs are isolated, concentrated to $2*10^{10}$ EVs/mL and co-cultured with fluorescently tagged peptide. To separate free peptide from loaded peptide, the sample is pelleted and later resuspended for downstream applications. (B) Representative distribution plot of EV size as measured by nanotracking analysis (NTA) software with a mean around 180nm. (C) EV diameter comparison between pre-loading and post-loading doses as measured by NTA. (D) Number of molecules of peptide loaded per EV is quantified based on a standard curve. (E) Percent of peptide loaded comparison across doses. Percent of peptide loaded based on standard curve was calculated by

(number of peptide molecules estimated in pellet / inputted number of molecules)*100. Each dot represents a biological replicate.

* p<0.05, **p<0.01

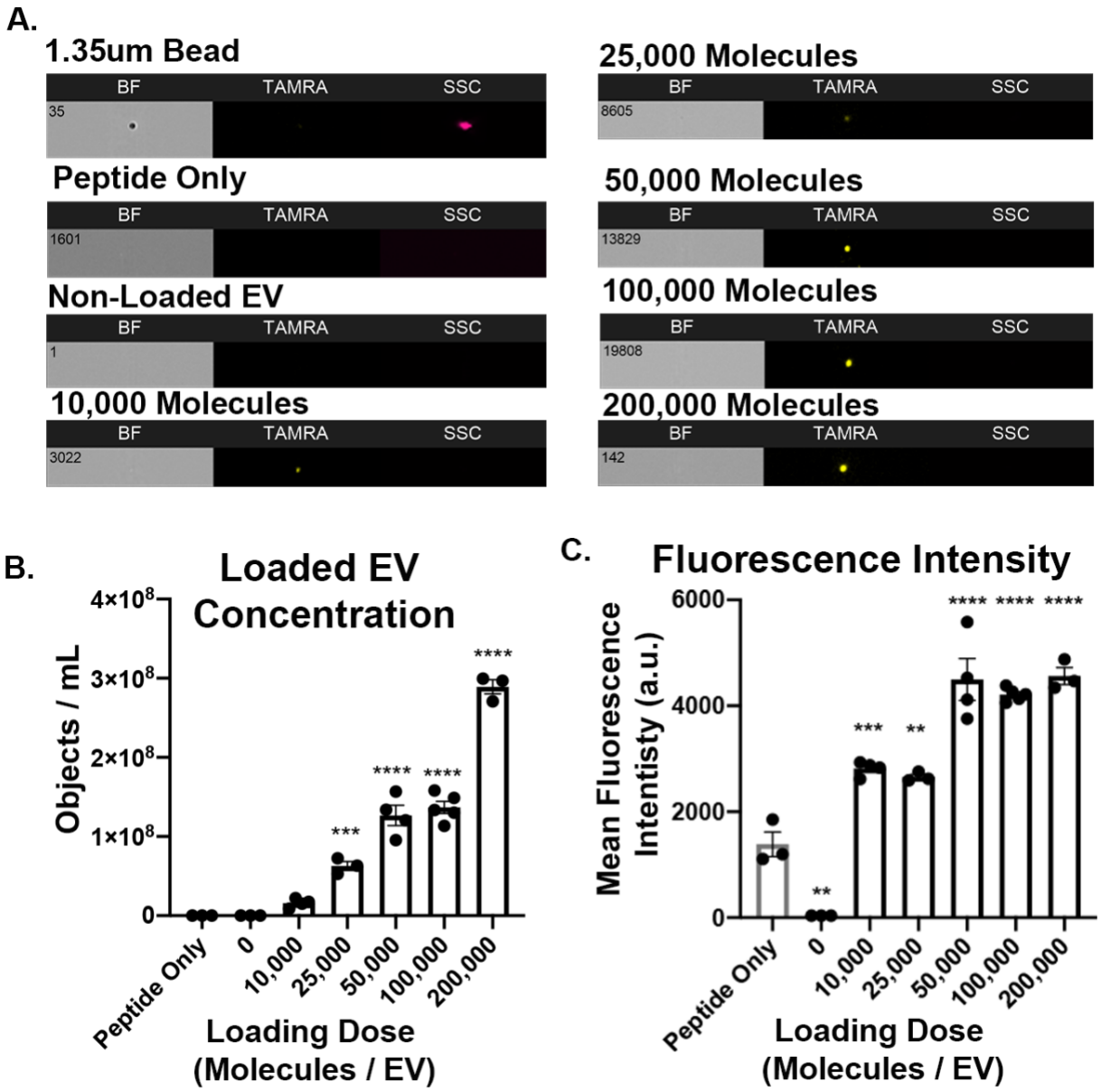

Figure 3.3: **Imaging flow cytometry analysis of peptide loading**

(A) Imaging flow cytometry images of negative control beads (1.35um), peptide only, non-loaded EVs, and loading doses of peptide loaded EVs. BF signifies brightfield, TAMRA

signifies the TAMRA fluorophore on the FARM5 peptide (XX nm excitation laser) and SSC signifies side scatter. Positive TAMRA represents FARM5 association with HEK293T EVs. (B) Quantification of the number of positive fluorescent EVs via imaging flow cytometry measured in objects / mL. (C) Mean fluorescence intensity measurement comparison between loading groups measured in MFI arbitrary units. Each dot represents a biological replicate which consists of three technical replicates. ** p<0.01, ***P<0.001 ****p<0.0001.

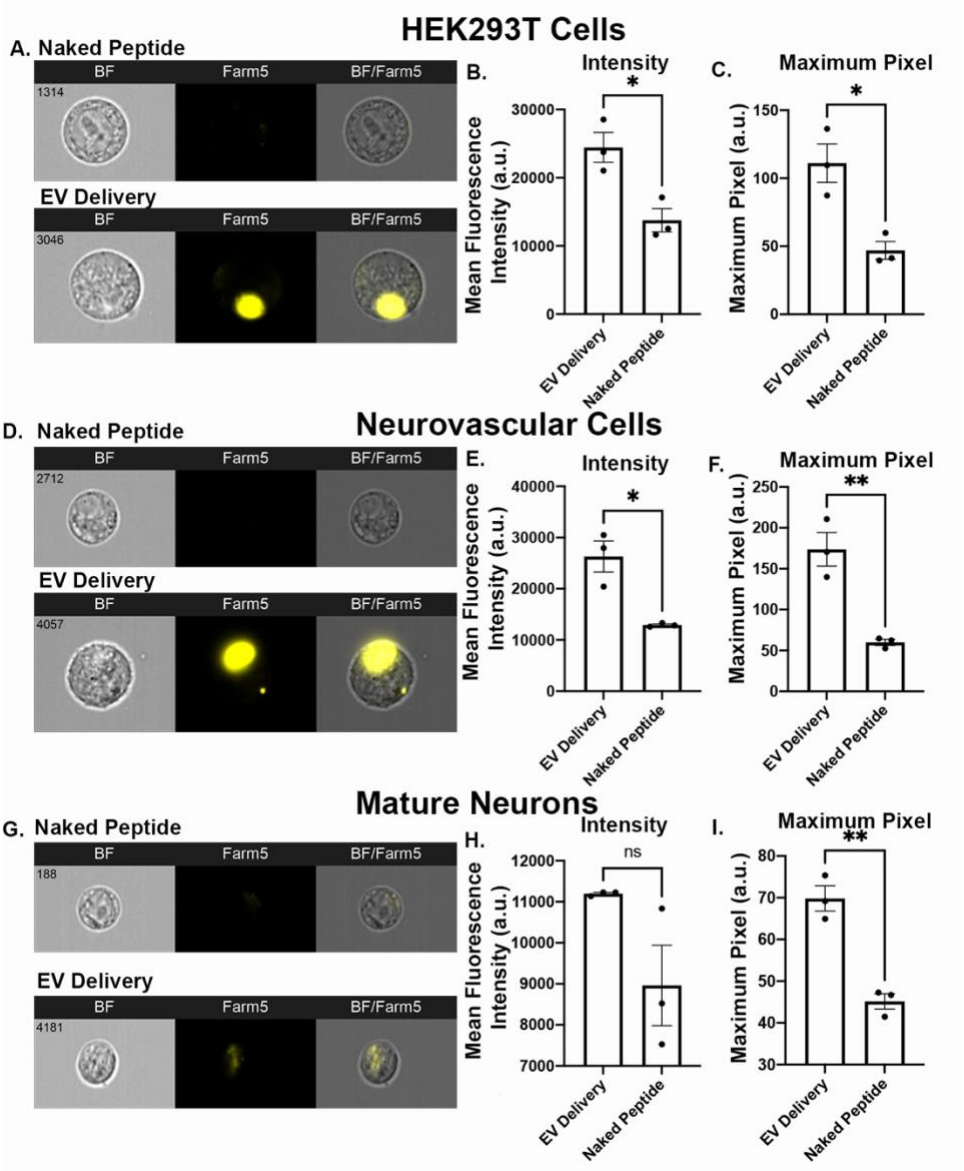

Figure 3.4: **EV Mediated Internalization of FARM5 Peptide into Recipient Cells**

(A) Imaging flow cytometry images of HEK293T cells co-cultured with naked peptide and EV mediated delivery of peptide. EV delivery displays greater amounts of positive fluorescence than naked peptide. (B-C) EV mediated delivery of FARM5 has significantly higher mean fluorescence intensity and maximum pixel in HEK293T cells. (D) Images of Blood brain barrier, neurovascular cell as recipient cells. (E-F) EV mediated delivery of FARM5 has significantly higher intensity and maximum pixel than naked peptide in neurovascular cells. (G) Images of mature neurons as recipient cells. (H-I) EV mediated delivery of FARM5 has significantly higher maximum pixel and trending differences in intensity compared to naked peptide. *p<0.05, **P<0.01.

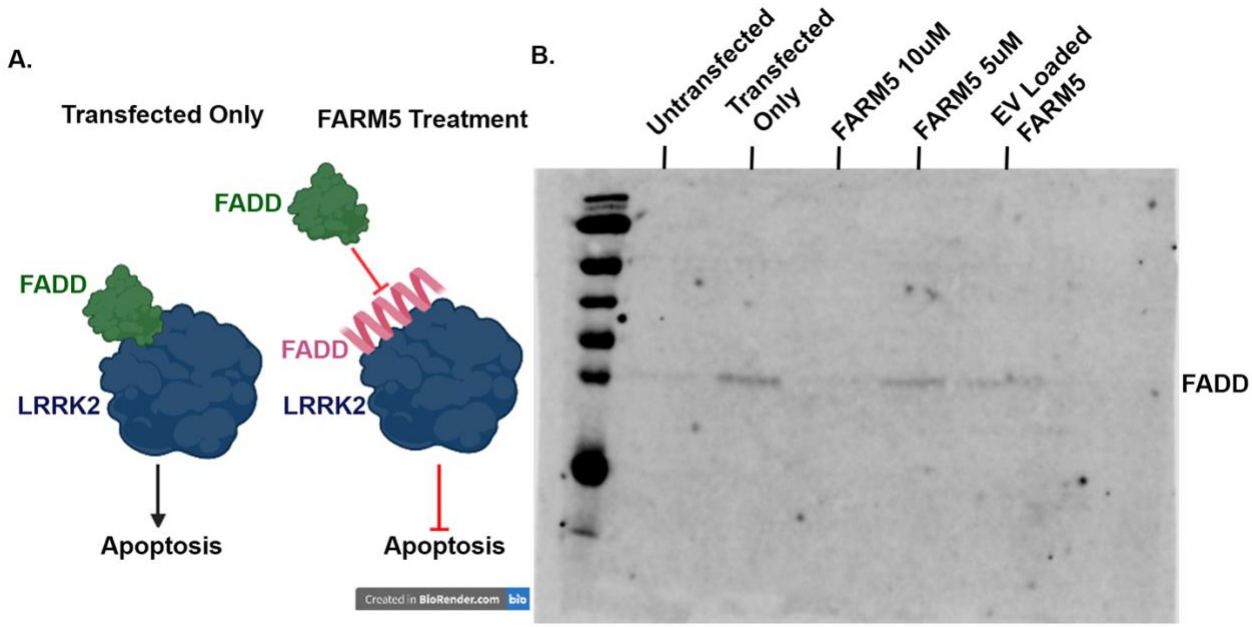

Figure 3.5: **LRRK2-FADD Binding Assays**

(A) Schematic representation of the FADD-LRRK2 binding and the proposed disruption by the FARM5 stapled peptide. (B) Co-immunoprecipitation assay of LRRK2 and FADD. Treatment groups include non-transfected, transfected with mutant Flag-LRRK2, V5-FADD, FARM5

peptide treatments, and peptide loaded EVs. Positive blot signifies binding of LRRK2 and FADD. Negative blot signifies lack of binding.

CHAPTER 4

EXPLORING THE PREDICTIVE VALUE OF LESION TOPOLOGY ON MOTOR FUNCTION OUTCOMES IN A PORCINE ISCHEMIC STROKE MODEL[4]

---

[4] **Brian J. Jurgielewicz†,** Kelly M. Scheulin†, Samantha E. Spellicy, Elizabeth S. Waters, Emily W. Baker, Holly A. Kinder, Gregory A. Simchick, Sydney E. Sneed, Janet A. Grimes, Qun Zhao, Steven L. Stice, Franklin D. West. 2021. *Scientific Reports*. 10.1038/s41598-021-83432-5. Reprinted here with permission of the publisher.

† these authors equally contributed to this work

4.1 ABSTRACT

Harnessing the maximum diagnostic potential of magnetic resonance imaging (MRI) by including stroke lesion location in relation to specific structures that are associated with particular functions will likely increase the potential to predict functional deficit type, severity, and recovery in stroke patients. This exploratory study aims to identify key structures lesioned by a middle cerebral artery occlusion (MCAO) that impact stroke recovery and to strengthen the predictive capacity of neuroimaging techniques that characterize stroke outcomes in a translational porcine model. Clinically relevant MRI measures showed significant lesion volumes, midline shifts, and decreased white matter integrity post-MCAO. Using a pig brain atlas, damaged brain structures included the insular cortex, somatosensory cortices, temporal gyri, claustrum, and visual cortices, among others. MCAO resulted in severely impaired spatiotemporal gait parameters, decreased voluntary movement in open field testing, and higher modified Rankin Scale (mRS) scores at acute timepoints. Pearson correlation analyses at acute timepoints between standard MRI metrics (e.g., lesion volume) and functional outcomes displayed moderate R values to functional gait outcomes. Moreover, Pearson correlation analyses showed higher R values between functional gait deficits and increased lesioning of structures associated with motor function, such as the putamen, globus pallidus, and primary somatosensory cortex. This correlation analysis approach helped identify neuroanatomical structures predictive of stroke outcomes and may lead to the translation of this topological analysis approach from preclinical stroke assessment to a clinical biomarker.

Keywords: ischemic stroke, permanent middle cerebral artery occlusion, lesion topology, magnetic resonance imaging, porcine stroke model

4.2 INTRODUCTION

Middle cerebral artery occlusion (MCAO) is the most common cause of ischemic stroke and one of the leading causes of mortality and long-term disability worldwide [1]. Nearly half of survivors with large territory middle cerebral artery (MCA) strokes have permanent deficits and fail to regain functional independence [2]. Magnetic resonance imaging (MRI) is commonly used in clinical practice to evaluate stroke pathology, determine injury severity, and predict patient outcomes. However, standard MRI measures, such as lesion volume and midline shift, alone have limited prognostic value with respect to functional deficit type, severity, and recovery [3-8]. Including stroke lesion location in relation to specific structures that coordinate with functional tasks (e.g., a lesioned primary somatosensory cortex leads to loss of limb coordination in walking) is likely to increase the predictive power of acute MRI metrics as biomarkers of stroke outcomes [9].

The prognostic value of lesion volume, the most commonly used biomarker to assess stroke severity and predict patient outcomes, is only moderate for motor impairments [5]. The correlation between lesion volume and quality of life measurements, such as modified Rankin Scale (mRS), have also proven to be limited [3,4]. To ultimately strengthen the prognostic value of MRI, lesion location has been assessed using topographic maps and resulted in increased predictive power [6,10-18]. Using a voxel-based lesion mapping technique, infarcts in the corona radiata, internal capsule, and insula were associated with worse mRS scores in patients with an MCAO ischemic stroke [6]. Lesions in the insular ribbon, lentiform nuclei, and middle corona radiata resulted in poor recovery based on the National Institutes of Health Stroke Scale (NIHSS) scoring [18]. Additionally, regionalized infarction in the left basal ganglia and frontal lobe were negatively correlated with functional independence scores [1]. Overall, these findings indicate that

lesion location is a key metric to determine an accurate prognosis of functional recovery post-stroke. Since discrepancies regarding lesion size and location in clinical stroke recovery exist as well as a void in viable translational models, the current study aims to characterize structures lesioned by an MCAO and evaluate their impact on stroke outcomes.

The Stroke Therapy Academic Industry Roundtable (STAIR) recommends using permanent occlusion gyrencephalic preclinical models, such as a porcine permanent MCAO model, and considering clinically relevant biomarkers, such as MRI detected lesion volume and location, to assess new treatments [19,20]. The pig model serves as a valuable large animal system to study the effects of MCAO on specific structures due to the comparable brain size and similar cerebral composition (e.g., gray to white matter ratio) between pigs and humans [21,22], and the ability to utilize a standardized porcine MRI brain atlas [23]. Critical brain structures present in the human and pig brain such as the hippocampus, caudate, and putamen are found in different locations, orientations, or absent in the rodent brain, the most commonly used stroke animal model [21,24-26]. For example, in the human and pig, the striatum is separated into two individual structures, the caudate nucleus and putamen, while the caudate nucleus and putamen are indistinguishable from each other in the rodent [27,28]. These unique differences in critical structures in the mouse brain relative to the human and pig brain are likely to have a profound effect on stroke outcomes. Our research group has developed a more translational porcine MCAO model that displays stroke pathophysiology comparable to humans including lesioning, cytotoxic and vasogenic edema, and white matter damage as determined by MRI [29-33]. In addition, we have demonstrated that the porcine MCAO model displays behavioral and motor function deficits similar to human patients [34-37]. Building upon the unique strengths of the porcine MCAO model and initial advancements utilizing basic acute MRI measures to predict functional outcomes, we

assessed the potential of lesion topology as an important MRI variable to advance functional prognostication.

In this exploratory study, we utilized MRI to evaluate acute clinical pathologies, including lesion volume and midline shift, and lesioning of individual brain structures to determine their potential in predicting chronic motor function outcomes in a porcine model of ischemic stroke. These findings suggest that including regional damage information in acute clinical evaluations of stroke patients is beneficial in determining acute motor deficits.

4.3 METHODS

Study design

All work involving the use of animals in this study were performed in accordance with the National Institutes of Health (NIH) Guidelines for the Care and Use of Laboratory Animals and was reviewed and approved by the University of Georgia (UGA) Institutional Animal Care and Use Committee (IACUC; Protocol Number A2018 01-029-Y1-A5). Inclusion criteria established a priori indicated that all castrated/ovariectomized, healthy animals with no lameness would be included. Researchers would exclude an animal if any signs of illness or lameness presented. All animals were included in the study and the experiments have been reported following/in compliance with the Animal Research: Reporting *in Vivo* Experiments (ARRIVE) guidelines. Biomedical Yucatan miniature pigs were acquired from Exemplar Genetics (Sioux Center, IA) and individually housed. Sexually mature castrated male and ovariectomized (OVX) female Yucatan miniature pigs between 68-98 kg and between 1-2 years of age were randomly assigned to either stroke (MCAO, n = 7) or non-stroked normal control (non-stroked, n = 5) groups. Sex hormones (e.g., testosterone and estrogen) have a confounding effect as they are neuroprotective [65-67]. This challenge is compounded in female animals where phases of the

reproductive cycle increase and decrease estrogen levels, thus leading to constantly changing neuroprotective levels in animals. Additionally, strokes typically occur in older women, post-menopause [68]. For uniformity, males were castrated, and females were OVX. All functional analysis was performed blinded with animal identifiers removed. The sample size for this study was determined by a power calculation based on our previous porcine MCAO studies [29,32].

Middle cerebral artery occlusion

One day prior to surgery, pigs were administered antibiotics (Ceftiofur crystalline free acid; 5mg/kg intramuscular (IM); Zoetis). A right sided permanent MCAO was performed on all stroke animals as described in Platt, et al. [69]. Pre-induction analgesia and sedation was achieved using xylazine (4 mg/kg IM; VetOne), midazolam (0.3 mg/kg IM; Heritage), methadone (0.2 mg/kg IM; Henry Schein Animal Health). Anesthesia was induced with propofol (to effect, intravenous (IV); Zoetis) and prophylactic lidocaine (1.0 mL 2% lidocaine; VetOne) was applied to the laryngeal folds to facilitate intubation. Anesthesia was maintained with isoflurane (1.0 – 2.0%; Abbott Laboratories) in oxygen.

Briefly, the middle cerebral artery (MCA) was accessed by performing a frontotemporal craniectomy with orbital rim ostectomy, zygomatic arch resection, and temporal fascia and muscle incision. The MCA was permanently occluded utilizing bipolar electrocautery forceps at the location distal to the origin of the Circle of Willis, resulting in ischemic infarction. The exposed brain was covered with a sterile oxidized cellulose hemostatic agent (VetSpon). Following occlusion, the temporalis muscle and epidermis were routinely re-apposed. After surgery, anesthesia was discontinued, pigs were returned to their pens and underwent standard monitoring and pain management. To treat and manage post-operative inflammation and pain, MCAO pigs received banamine (2.2 mg/kg IM or IV; Merck) during MCAO surgery

and every 12 hours for 24 hours and every 24 hours for 3 days following surgery and methadone (0.2 mg/kg IM or IV) every 6 hours for 24 hours following surgery. Non-stroked normal animals did not undergo surgery.

Magnetic resonance imaging data acquisition

MRI was acquired on a GE Signa HDx 3.0 Tesla scanner using an 8-channel torso coil at 1d and 28d post-MCAO. Under general anesthesia, MRI of the brain was performed with the animal positioned in supine recumbency. The multiplanar MRI protocol included five sequences: 1) 3D Fast SPoiled GRadient echo (FSPGR) T1-Weighted (T1W), 2) Fast Spin Echo (FSE) T2W, 3) T2-Weighted Fluid Attenuated Inversion Recovery (T2FLAIR), 4) Spin Echo (SE) Diffusion Weighted Imaging (DWI), and 5) SE DTI.

Ischemic stroke was confirmed 1d post-MCAO by comparing the hyperintense infarction in T2FLAIR and DWI to the corresponding hypointense region in apparent diffusion coefficient (ADC) maps, indicating cytotoxic edema (data not shown). Axial 3D FSPGR sequences were acquired with the following parameters: inversion time (TI) = 450 ms, flip angle = 20°, slice thickness = 1.0 mm, field of view (FOV) = 19.8 cm^3, and matrix size (frequency x phase) = 198 x 198. Axial and coronal FSE T2W images were acquired with the following parameters: repetition time (TR) = 6260 ms, echo time (TE) = 124 ms, slice thickness = 3.0 mm, FOV = 18-20 cm^2, and matrix size (frequency x phase) = 384 x 288. Axial T2FLAIR images were acquired with the following parameters: TR = 9070 ms, TE =120 ms, TI = 2587 ms, slice thickness = 3.0 mm, FOV = 20 mm^2, and matrix size (frequency x phase) = 320 x 224. Axial DWI was acquired with the following parameters: b = 0 and 1000, TR = 6000 ms, number of excitation (NEX) = 4, slice thickness = 3.0 mm, FOV = 26.6 cm^2, matrix size (frequency x phase) = 256 x 256 with 3 diffusion directions. In order to obtain information on white matter integrity, DTI was acquired

in the axial plane with the following parameters: TR = 10,000 ms, isotropic voxel = 2.0 mm x 2.0mm x 2.0mm, with 30 diffusion encoding directions; fractional anisotropy (FA) maps were generated from DTI images as described below. During DTI acquisition, an error occurred when acquiring the DTI sequence of one MCAO animal, therefore, this animal was excluded from FA analysis.

Magnetic resonance imaging data preprocessing

DICOM images of the T1W and T2W volumetric series were converted into NIfTI (Neuroimaging Informatics Technology Initiative) format using the "dcm2niix" tool [70]. Brain masks were obtained by separating brain tissue from the skull and other surrounding tissues using the FSL brain extraction tool (BET) and then manually refining slice-by-slice the generated FSL-BET masks in 3D Slicer version 4 (slicer.org, [71]). Lesion masks were manually drawn in 3D Slicer using the axial T2W images to identify the hyperintense region associated with the lesion after applying an inversion filter to remove bias in lesion identification **(Supplementary Figure 1)**.

The porcine brain atlas [23] was then spatially normalized to each stroked pig's masked T1W image (note that each stroked pig's T2W image is in the same space as its T1W image). First, a spatial transformation was calculated between the pig brain atlas' associated T1W anatomical image, which is in the same space as the atlas, and each pig's masked T1W image using the Old Normalize Statistical Parametric Mapping algorithm (SPM12, Institute of Neurology, University College London) [72]. Then the calculated spatial transformation was applied to the atlas. Spatial transformations consisted of a 12-parameter affine transformation, followed by a nonlinear deformation transformation in stereotaxic coordinates [73,74].

Magnetic resonance imaging data analysis

Lesion and hemispheric volumes were analyzed using OsiriX software (Version 10.0.5, Pixmeo SARL, Bernex, Switzerland) at default thresholds from T2W sequences. Hemisphere and lateral ventricle volumes were calculated for each slice using manual segmentation of the ipsilateral and contralateral hemispheres to find the area and multiplying by the slice thickness (3.0 mm). The lateral ventricle volumes were subtracted from each hemisphere to eliminate non-brain tissue. The cerebellum was not included in hemispheric volume analysis.

The percentage of the ipsilateral hemisphere that the lesion occupied was calculated as a sum of the lesion volume per slice (multiplied by slice thickness, 3.0 mm) divided by the total ipsilateral hemispheric volume.

Hemispheric swelling and atrophy were calculated using the total ipsilateral hemisphere volume divided by the contralateral hemisphere volume, which is reported as a percentage change.

Midline shift analysis was also analyzed using OsiriX according to a previous publication [34]. Briefly, three linear measurements were utilized to determine the midline after stroke at 1d and 28d post-stroke using the axial T2W images for each pig. The first line was drawn at the septum pellucidum in between the lateral ventricles. The next line drawn was the ideal midline using boney structures and non-brain anatomy to determine the natural midline (red lines in **Figure 1**). The midline shift was determined by drawing and measuring a third perpendicular line between the ideal midline and septum pellucidum.

DTI was used to evaluate white matter integrity in the corpus callosum (CC) through FA analysis. FA maps were generated using the FMRIB's Diffusion Toolbox (FDT) (FSL, University of Oxford, UK) [75-77], and FA values of the CC were measured using ImageJ, FIJI [78,79] to

manually segment each major white matter tract in the ipsilateral and contralateral hemispheres. To account for hemispheric swelling and atrophy, the ipsilateral ROI was manipulated to encompass as much of the remaining visible structure possible without changing the area of the ROI.

Using the co-registered lesion masks and porcine brain atlas [23], percentage of structure (PoS) and percentage of lesion (PoL) were calculated using MatLab (R2018b, The Mathworks, Inc.) to determine the percentage of each individual structure affected by the lesion and the percentage of the lesion that overlaps with individual brain atlas structures, respectively.

$$PoS = [Equation]$$

$$PoL = [Equation]$$

T1W images were used to generate figures. The pig brain atlas contained 178 individual cerebral structures, including 42 paired and 9 single deep brain structures, 5 ventricular system areas, 6 paired deep cerebellar nuclei, 12 cerebellar lobules, and 28 cortical areas per hemisphere [23].

Gait data collection

Gait analysis was performed utilizing the GAITFour walkway system as previously described [32] and assessed using GAITFour software (Version 4.9 x 5, CIR Systems, Franklin, NJ) . Pre-MCAO gait data was collected on 3 separate days (d) for each pig. After stroke surgery, gait analysis was performed on 2d, 8d, 15d, and 27d post-MCAO. Gait collection occurred for a maximum of 15 minutes at each collection time point for each pig. Five recordings of the pig traversing the track at a consistent trotting gait was used for analysis.

Behavior data collection

Open field testing was performed for all pigs pre-MCAO and on 2d, 8d, 15d, and 27d post-MCAO. Behavior tests were recorded using EthoVision XT software (Version 11.5, Noldus

Systems, Wageningen, Netherlands) as described previously [32]. Briefly, individual pigs were placed in a 2.7 x 2.7 m open field arena for 10 minutes and allowed to voluntarily explore. EthoVision was used to track movement duration, velocity, and distance traveled and also to preform data analysis.

Modified Rankin Scale scoring

Neurological disability was assessed post-MCAO using a pig-adapted Modified Rankin Scale (mRS) as previous published [34]. All pigs were assessed 1 day prior to MCAO surgery and 4 hours (h), 8h, 12h, 16h, 20h, 24h, 2d, 3d, 4d, 5d, 6d, 8d, 15d, and 27d post-MCAO surgery. Possible scores ranged from 0 (no residual stroke symptoms) to 6 (death due to stroke).

Statistical analysis

GraphPad Prism 8 (Version 8.4.0; San Diego, CA) was utilized to calculate the statistics. Statistical differences in MRI parameters were evaluated using paired t tests between 1d and 28d post-MCAO. White matter integrity was evaluated between the left and right CC with paired t tests at pre-MCAO, 1d and 28d post-MCAO. To determine if MLS and hemispheric swelling/atrophy were statistically different from normal at each timepoint, one-sample t tests were performed with a hypothetical value of 0 for MLS and 100 for hemispheric changes, statistical significance was indicated by $. For longitudinal analyses of gait and behavior, 2-way repeated measures ANOVA were conducted with Sidak's multiple comparisons test when appropriate. All error bars represented SD. Pearson correlations were evaluated at 2d and 8d post-MCAO for the 6 gait parameters reported in the manuscript to determine the association between percent of lesioned structure (top reported PoS) and canonical MRI metrics (lesion volume, lesion percent, midline shift, and hemispheric swelling) to motor impairments. A minimum of three pigs had to have a lesion within the individual structure to conduct each

correlation analysis. From here, R values were reported in a heat map and the False Discovery Rate (FDR) corrected p-values were reported in **Supplementary Table 3**. QQ plots of the residuals were generated to assess normality. Data are shown as mean±SD. Statistical significance was indicated where * (or # or $) signified $p<0.05$; ** (or ## or $$) signified $p<0.01$; *** (### or $$$) signified $p<0.001$; and **** (or #### or $$$$) signified $p<0.0001$.

4.4 RESULTS

MCAO resulted in lesioning, hemispheric swelling/atrophy, and decreased white matter integrity

To assess the dynamic pathophysiological response of an MCAO ischemic stroke, T2Weighted (T2W) MRI sequences were evaluated. Visual assessments of pre-MCAO pig brains showed no observable damage **(Figure 4.1a)**. At 1 day (d) post-MCAO, the MCAO group displayed substantial lesioning (hyperintense region, white arrows), a midline shift towards the unaffected contralateral hemisphere, and decreased ventricle size due to cerebral swelling **(Figure 4.1b)**. By 28d post-MCAO, animals showed a decrease in lesion size, a midline shift towards the ipsilateral hemisphere, and increased ventricle size due to tissue atrophy **(Figure 4.1c)**. Quantitative lesion volume analysis showed significant brain lesioning 1d post-MCAO with an average volume of 11.39±4.91 cm^3 and by 28d post-stroke, lesion volume size (4.22±2.12 cm^3) was significantly ($p=0.0010$) reduced **(Figure 4.1d)**. To account for potential animal variability, lesion volume was evaluated as a percent of the ipsilateral hemisphere. At 1d post-MCAO, the lesion occupied 32.64±12.99% of the ipsilateral hemisphere and by 28d post-MCAO, the lesion occupied 14.54±7.66% ($p=0.0004$) **(Figure 4.1e)**. In MCAO pigs, the ipsilateral hemisphere showed 1.57±0.83 mm midline shift towards the contralateral hemisphere at 1d post-MCAO, indicating hemispheric swelling and was different from normal

(p=0.0024). At 28d post-MCAO, the ipsilateral hemisphere showed a midline shift of -1.99±1.00 mm away from the contralateral hemisphere (1d vs 28d post-MCAO, p=0.0003), indicating hemispheric atrophy and was different from normal (p=0.0019) **(Figure 4.1f)**. At 1d post-MCAO, animals showed hemispheric swelling with a 15.17±7.89% increase in ipsilateral hemisphere volume and was different from normal (p=0.0022). Cerebral atrophy was observed at 28d post-MCAO with a 10.41±3.63% decrease in ipsilateral hemisphere volume from 1d post-MCAO (p<0.0001) **(Figure 4.1g)** and was different from normal (p<0.0001).

Axial diffusion tensor imaging (DTI) images in pre-MCAO animals depict major white matter tracts from a medial slice of the pig brain and showed an intact ipsilateral (right side, white arrow) and contralateral (left) CC with fractional anisotropy (FA) values of 0.42±0.10 and 0.45±0.13, respectively (p>0.05) **(Supplementary Figure 4.2a, d)**. At 1d post-MCAO, the ipsilateral CC was disrupted and showed a significant (p=0.0347) decrease in FA (0.33±0.04) compared to the contralateral CC (0.47±0.12) **(Supplementary Figure 4.2b, e)**. The ipsilateral CC had recovered FA by 28d post-MCAO with ipsilateral FA of 0.39±0.10 and contralateral FA of 0.41±0.05 (p>0.05) (**Supplementary Figure 4.2c, f**). The corpus callosum (CC) is responsible for interhemispheric communications and, due to the location of the ischemic lesion, we found the CC to be impacted. The structural integrity of the CC after stroke has been shown to be repeatedly associated with motor deficits [38,39]. Overall, standard MRI analyses showed significant lesioning along with hemispheric swelling, subsequent atrophy, and decreased white matter integrity post-MCAO.

Ischemic lesioning spanned the thalamic nuclei, striatum, limbic system, and multiple Brodmann's areas

The ischemic lesion affected multiple major brain regions including the thalamic nuclei, striatum, limbic system, and various Brodmann's areas. A regional pixel analysis was completed to calculate the percentage of each structure lesioned. The structures with the highest percentage of infarction (percent of structure, PoS) at 1d post-MCAO included the claustrum (65.91±29.68%), inferior temporal gyrus (62.15±27.67%), superior temporal gyrus (58.91±36.32%), insular cortex (54.45±31.35%), middle temporal gyrus (44.43±24.49%), putamen (44.00±22.23%), somatosensory association cortex (43.05±27.06%), secondary visual cortex (40.57±28.62%), globus pallidus (34.52±28.61%), and primary somatosensory cortex (33.48±23.73%) **(Figure 4.2a)**. At 28d post-MCAO, the structures with the highest level of lesioning included the middle temporal gyrus (39.84±31.80%), superior temporal gyrus (31.14±17.55%), inferior temporal gyrus (18.19±13.55%), somatosensory association cortex (16.78±11.46%), insular cortex (15.95±9.28%), associative visual cortex (10.02±14.48%), primary somatosensory cortex (8.44±8.92%), prepiriform area (7.84±5.85%), fusiform gyrus (6.82±10.44%), and secondary visual cortex (5.83±6.30%) **(Figure 4.2b)**. The percent of the identified lesion (PoL) in each structure was quantified to represent the percent of the lesion that affected specific brain structures and characterized stroke location. At 1d post-MCAO, the structures that occupied the lesion included the insular cortex (8.45±5.09%), primary somatosensory cortex (6.33±4.82%), secondary visual cortex (6.02±4.34%), inferior temporal gyrus (5.16±4.65%), somatosensory association cortex (4.98±2.87%), putamen (3.22±1.58%), middle temporal gyrus (2.59±2.97%), superior temporal gyrus (2.36±1.68%), parahippocampal cortex (2.06±3.00%), claustrum (1.94±0.71%), prepiriform area (1.44±0.61%), amygdala

(1.23±1.95%), and primary visual cortex (1.08±1.36%) **(Supplementary Figure 4.3a)**. By 28d post-MCAO, PoL structures that occupied the lesion included the insular cortex (7.95±6.02%), primary somatosensory cortex (5.64±6.36%), somatosensory association cortex (5.41±3.59%), middle temporal gyrus (4.23±3.01%), inferior temporal gyrus (3.27±2.72%), superior temporal gyrus (3.15±1.87%), secondary visual cortex (2.07±1.93%), parahippocampal cortex (1.42±2.34%), and prepiriform area (1.30±1.06%) **(Supplementary Figure 4.3b)**. A complete list of lesioned structures (PoS and PoL) (Mean ± standard deviation (SD)) are detailed in **Supplementary Table 4.1**. Notably, 100% of pigs had lesioning in the claustrum, putamen, insular cortex, secondary visual cortex, inferior temporal gyrus, superior temporal gyrus, parahippocampal cortex, and prepiriform area **(Table 4.1)**.

MCAO induced functional gait deficits

To assess changes in motor function, gait analysis was performed on all animals pre-MCAO to establish a baseline and collected over a 27-day period following MCAO. Compiled functional outcome (gait and behavior) parameters definitions that were analyzed in this study can be found in **Supplementary Table 4.2**. The MCAO group showed significant decreases in the left front (LF) limb (contralateral to MCAO) at 2d post-MCAO in velocity (**Figure 4.3a**; Pre: 198.78±13.24 cm/s vs. Day 2: 71.49±44.22 cm/s, p=0.0048) and cadence (**Figure 4.3a**; Pre: 133.01±8.23 stride/min vs. Day 2: 69.78±24.61 stride/min, p=0.0081) as compared to pre-MCAO. In addition, there were significant decreases at 2d post-MCAO in the LF limb in stride length (**Figure 4.3b**; Pre: 89.01±3.42 cm vs. Day 2: 57.98±10.96 cm, p=0.0042), step length (**Figure 4.3b**; Pre: 44.36±2.05 cm vs. Day 2: 29.65±5.00 cm, p=0.0031), and swing percent (**Figure 4.3c**; Pre: 51.93±2.47% vs. Day 2: 31.45±6.14%, p=0.0034), along with an increase in stance percent (**Figure 4.3c**; Pre: 48.06±2.49% vs. Day 2: 68.55±6.12%, p=0.0034) relative to

pre-MCAO. Velocity (**Figure 4.3a**; Day 8: 114.77±48.21 cm/s, p=0.0168), cadence (**Figure 4.3a**; Day 8: 90.03±27.37 stride/min, p=0.0247), stride length (**Figure 4.3b**; Day 8: 73.29±10.29 cm, p=0.0289), step length (**Figure 4.3b**; Day 8: 36.96±5.39 cm, p=0.0324), swing percent (**Figure 4.3c**; Day 8: 38.98±5.53%, p=0.0104), and stance percent (**Figure 4.3c**; Day 8: 61.03±5.52%, p=0.0104) continued to display deficits at 8d post-MCAO. No significant (p>0.05) differences between the MCAO and non-stroked groups were measured pre-MCAO. Non-stroked pigs did not have any significant differences at any measured timepoints (**Figure 4.3**). Stroked animals exhibited signs of recovery after 8d post-MCAO, showing no significant changes in measured parameters to non-stroked animals or pre-stroke values (p>0.05). Gait parameters for the other three limbs, right front (RF), left hind (LH), and right hind (RH), are detailed in **Supplementary Figure 4.4**.

MCAO induced contralateral limb weakness

Changes in weight distribution in all four limbs due to stroke was evaluated by assessing deviations in total pressure index for each individual limb. Total pressure index is the sum of peak pressure values recorded from each activated sensor by a hoof during contact and is representative of weight distribution. The MCAO group showed a significant decrease in total pressure index at 2d post-MCAO in the LF limb (**Supplementary Figure 4.5a**; Pre: 28.99±1.66 vs. Day 2: 26.87±2.07, p=0.0224) with a corresponding increase in pressure in the RF limb (**Supplementary Figure 4.5b**; Pre: 29.57±1.95 vs. Day 2: 31.87±2.30, p=0.0413). By 8d post-MCAO, total pressure index showed no significant changes in measured parameters compared to pre-MCAO in the LF limb (**Supplementary Figure 4.5a**; Pre: 28.99±1.66 vs. Day 8: 27.96±1.45, p=0.1076) and the RF limb (**Supplementary Figure 4.5b**; Pre: 29.57±1.95 vs. Day 8: 29.65±1.78, p=0.9999). LH and RH limb total pressure indices did not change significantly

compared to pre-MCAO (**Supplementary Figure 4.5c-d;** p>0.05). However, these results were expected in the pig model, as the forelimbs carried 60% of the body weight and, thus, are more susceptible to disruptions in weight distribution. Collectively, gait analysis provided quantifiable parameters showing functional gait deficits in weight distribution induced by MCAO.

MCAO pigs showed deficits in voluntary movement and behavioral scores

Open field testing was performed to assess behavioral changes post-stroke. Representative tracking images displayed decreased voluntary movement at 2d post-MCAO **(Figure 4.4a)**. At 2d post-MCAO, the MCAO group showed a significant decrease in distance traveled (**Figure 4.4b**; Non-stroked: 75.70±23.86 m vs. MCAO: 27.83±13.80 m, p=0.0346), movement duration (**Figure 4.4c**; Non-stroked: 230.55±38.87 s vs. MCAO: 85.87±49.84 s, p=0.0022), and velocity (**Figure 4.4d**; Non-stroked: 0.13±0.04 m/s vs. MCAO: 0.05±0.02 m/s, p=0.0350) compared to the non-stroked group. By 8d post-MCAO, there were no significant differences between groups (p>0.05).

A pig mRS assessment was used to evaluate the degree of disability pre- and post-MCAO with 0 being no residual stroke symptoms and 6 being death **(Supplementary Figure 4.6)**. At all timepoints non-stroked animals had an mRS score of 0. At 4 hours (h) to 3d post-MCAO, stroked animals had mean mRS scores above 3 (ranging from 2-5) and were significantly impaired relative to non-stroked animals (4h post-MCAO: 4.86±0.38, p<0.0001; 8h post-MCAO: 4.57±0.79, p<0.0001; 12h post-MCAO: 3.71±0.76, p=0.0002; 16h post-MCAO: 3.71±0.95, p=0.0007; 20h post-MCAO: 3.57±0.98, p=0.001; 24h post-MCAO: 3.57±0.79, p=0.0003; 2d post-MCAO: 3.43±0.98, p=0.0013; 3d post-MCAO: 3.29±0.76, p=0.0004). At 4d (2.57±1.13, p=0.0144), 6d (1.71±0.95, p=0.0455) and 8d (1.57±0.79, p=0.0275) post-MCAO, stroked animals still had a significantly greater mRS score than non-stroked controls suggesting

persistent deficits. After 8d post-MCAO, scores trended between 0-2 and displayed no significant differences from normal animals ($p>0.05$) suggesting overall recovery.

Location of stroke lesion in structures associated with motor coordination had prognostic value when evaluating motor functional outcomes

Development of an accurate prognosis method by identification of acute parameters is vital to assess efficacy of novel treatments in preclinical models. Thus, correlation analyses were performed to determine unique relationships between individual lesioned brain structures at 1d post-MCAO and functional gait outcomes at 2d and 8d post-MCAO. Lesioned structures ranked by PoS (y-axis) and top gait outcomes (x-axis) were evaluated by Pearson correlations for 2d post-MCAO (**Figure 4.5a**) and 8d post-MCAO (**Figure 4.5b**). R values were reported with cell color indicating correlation direction and strength. FDR p-values corrected for multiple comparisons can be found in **Supplementary Table 4.3**. In general, structures associated with motor coordination and function had higher R values when using PoS as the quantitative indicator. This suggests that identification of lesion topology, specifically the percentage of structure with an ischemic lesion, can be used as a predictive biomarker for functional outcomes.

Further, commonly used MRI parameters including lesion volume, midline shift, and hemispheric swelling were evaluated for their potential to predict 6 gait functional outcomes **(Figure 4.5)**. Pearson correlation analyses were also conducted at 2d and 8d post-MCAO between canonical MRI metrics and functional gait outcomes. For 1d post-MCAO MRI parameters (y-axis) and top gait outcomes (x-axis) were evaluated by Pearson correlations for 2d post-MCAO (**Figure 4.5c**) and 8d post-MCAO (**Figure 4.5d**). R values were reported with cell color indicating correlation direction and strength. FDR p-values corrected for multiple

comparisons can be found in **Supplementary Table 4.3**. Traditional MRI diagnostic parameters showed moderate prognostic value in this preclinical model. However, the inclusion of lesion topology may further advance the relationship between individual structures and functional outcomes.

4.5 DISCUSSION

MRI assessment of stroke severity and injury characteristics has significant clinical potential to better predict functional outcomes. However, standard clinical practice typically relies on basic injury metrics such as lesion volume and midline shift and does not account for injury location [6,14,40-42]. Since brain functions such as motor and executive control are highly regionalized to specific brain structures, it is logical that consideration of injury location would have a profound effect on clinical prognoses [6]. In this exploratory study, we demonstrated that the canonical MRI metrics (e.g., lesion volume, lesion percent, midline shift, and hemispheric swelling) were predictive of functional deficits. However, we showed that specific lesioned brain structures responsible for motor coordination and function (e.g., putamen, globus pallidus, and primary somatosensory cortex) demonstrated higher R values (R= |0.58| to |0.81|) to motor function deficits than canonical MRI metrics (R= |0.30 to |0.69|). The results from this exploratory study showed that lesion topology analysis may be a stronger predictor of functional outcomes at acute timepoints after ischemic stroke when the structures lesioned involve motor coordination and function. However, additional studies are needed with increased animal numbers to confirm this finding. In recent studies, our team has shown the pig MCAO model displays significant similarities to human stroke patients with respect to functional deficits [29-32,34,37,43]. For the first time in a neural injury porcine model, we have adapted an MRI pig atlas [23] to account for stroke induced structural changes and demonstrated that the effected MCA territory

and brain structures are also comparable to humans, which likely explains the similarities in functional outcomes [44,45]. These results further support the pig as a translational large animal model for the study of ischemic stroke pathophysiology, development of prognostic biomarkers, and therapeutic interventions.

The MCA is one of the largest arteries in the brain with the highest incidence of occlusion causing ischemic stroke in humans [1,44]. Anatomically, the MCA provides vascular support to a large territory including the lateral inferior frontal lobe, superior temporal gyrus, primary motor and somatosensory cortices, basal ganglia structures, internal capsule, and insular cortex, among others [1,2,44]. Thus, the blockage of this artery by an embolus or thrombus leading to an ischemic stroke can be particularly detrimental causing behavioral and gait deficits [18]. Clinically, an MCAO stroke lesion typically spans parts of the frontal, temporal, and parietal lobes, including the insular cortex, as well as deep brain structures such as the amygdala, caudate nucleus, putamen, globus pallidus, and thalamic nuclei [6,14-18,45-47]. In pigs, we found MCAO resulted in the highest percent of lesion in the insular cortex, somatosensory cortices, temporal gyri, and visual cortices. In a thromboembolic MCAO cynomolgus monkey model, infarction was similarly observed in the basal ganglion, internal capsule, temporal cortex, and insular cortex and it was noted that contralateral hemiparesis in their model was likely caused by ischemia in the temporal cortex and internal capsule [48]. Although the MCA stroke territory depends on the individual differences of MCA branching, our model showed a high level of reproducibility with respect to infarct location. 100% of the pigs showed lesioning in the claustrum, inferior temporal gyrus, insular cortex, parahippocampal cortex, putamen, prepiriform area, secondary visual cortex, and superior temporal gyrus. Thus, we have identified consistent and reproducible lesion locations that can aid in the understanding of the pathophysiology of

stroke progression and provide a framework for assessing the importance of lesion location on functional outcomes.

Gait and behavior analyses have been used as clinical biomarkers to quantify stroke severity, functional deficits, and subsequent recovery potential. Consistent with human manifestations where patients have decreased cadence and walk six times slower than aged matched pairs [35], the porcine MCAO group showed similar deficits in cadence and velocity [35,36]. Humans display other spatiotemporal abnormalities including a decreased stride length, increased cycle time, and increased stance time [49], which have consistently manifested in the porcine model [30,32,37]. Asymmetrical hemiplegic gait is commonly induced by stroke and results in a shifting of weight between limbs and subsequent decreased propulsion, where the contralateral limb assumes significantly less weight and decreased pressure [36]. Here, stroked pigs showed asymmetrical hemiplegic gait with a decreased total pressure index in the contralateral limb. As seen in the open field test and mRS scoring, MCAO pigs displayed deficits similar to those of stroke patients, including decreased voluntary movement and velocity, with overall behavioral deficits [50,51]. These impairments are typically a result of infarction to the motor and somatosensory cortices, and subcortical structures [50], similar to the regions injured in our pig model. Manifestation of clinically relevant gait deficits in the porcine model suggests that this model may be useful in understanding post-stroke functional deficits and recovery patterns.

Recent clinical retrospective analyses assessing the prognostic capacity of early MRI stroke injury parameters indicate lesion location can be highly predictive of functional outcomes, whereas lesion volume alone is only moderately predictive [4,12-14,17,52]. In fact, a voxel-based lesion mapping approach showed location, independent of lesion volume, is predictive of higher NIHSS scores at admission and discharge [18]. Here, regional lesion location showed higher R values to

acute functional outcomes in brain regions responsible for motor function, including the putamen, globus pallidus, and primary somatosensory cortex, at 2d post-MCAO compared to brain regions that are not responsible for motor coordination but still highly effected by the stroke lesion, including the claustrum, superior and middle temporal gyri, and secondary visual cortex. The structures impacted that presented higher correlations to gait outcomes are directly involved with motor and executive control and therefore it is expected that they would influence gait deficits 2d post-MCAO [53-55]. For example, effected structures, such as the globus pallidus (a critical regulatory structure of voluntary movement [56]), were predictive of early functional outcomes such as velocity with an R value of -0.76 at 2d post-MCAO, whereas lesion volume only had an R value of -0.37. In addition, the insular cortex, which is sensitive to hypoperfusion [47], has a high likelihood of infarct growth [10], and is associated with functional deficits [46], was affected in 100% of pigs at 1d post-MCAO and was the largest PoL structure effected. The insular cortex also displayed moderate correlation relationships between PoS and gait impairments (R=|0.37| to |0.56|). In a large clinical study, MCA strokes resulted in higher disability with the lowest functional independence measure (FIM), a functional assessment that consists of 13 motor and 5 cognitive metrics, compared to other territory strokes [57]. These findings support strong correlations between MCA territory lesioning of structures involved in motor coordination and motor deficits. Many clinical studies often examine the correlation between MRI based structural changes and one or two functional scales, such as mRS or NIHSS scores [7,18,57-59], while our study evaluated the relationship between multiple major gait parameters acquired on the sensitive GAITFour mat and the highly lesioned structures in our porcine model. Here, we found that ischemic infarcts in the putamen, globus pallidus, and primary somatosensory cortex were associated with higher R values to motor functional deficits

(R>|0.5|). A voxel-based lesion symptom mapping approach in humans determined infarcts within the area leading from the corticospinal tract to cortical motor areas, including fibers from the primary somatosensory cortex and other secondary motor regions, were critical for maintaining proper hand motor performance after a stroke [60]. We were encouraged to discover similar relationships between major structures responsible for motor function and functional gait outcomes in our pig model.

However, a number of limitations were associated with this exploratory study including the lack of significance in our correlation analyses, although it is likely a function of small sample size (**Supplementary Table 4.3**). Additionally, correlations between MRI and motor function at 8d post-MCAO were reduced relative to 2d post-MCAO. This may be a result of spontaneous recovery observed in functional outcomes 8d post-MCAO, even though significant differences still remained between stroked and non-stroked animals. A general shortcoming of the topological analysis approach is each structure should be considered individually based on its function and associated outcomes. This adds an increased level of complexity with the evaluator needing to be well versed in the function of each structure and making it less practical as a clinical prognostic tool. A benefit of the traditional MRI analysis approaches (e.g., lesion volume, midline shift, and swelling) is the ease of clinical use with no neuroanatomical key of functional information. Furthermore, in both animal stroke models and clinical patients, MRI image registration to neuroanatomical atlases are often imperfect due to hemispheric swelling and atrophy. In our pig model, registration of larger structures demonstrated an acceptable level of atlas registration fidelity, while there was decreased accuracy in the registration of smaller structures such as the contralateral ventricle and small white matter structures. These potential inconsistencies represent an unmet need in the preclinical and clinical settings to improve atlas

registration techniques accounting for swelling, midline shifts, and other commonly observed stroke pathologies. The rodent community has made strides to account for registration errors including the development of an enhanced mathematical framework to correct for edema in evaluating lesion size leading to improved image analysis [61]. Future studies utilizing the pig stroke model should build upon these advances to improve registration. Despite these limitations, the topological approach utilized in this study has helped identify lesioned structures involved in motor function related to stroke outcomes and supports the clinical use of this methodology. Further in-depth studies with larger cohorts are warranted to generate more conclusive preclinical data.

In this exploratory study utilizing the Yucatan pig MCAO model, we demonstrated that evaluating lesioning in specific brain structures demonstrated moderate-to-strong relationships with motor function impairments as compared to lesion volume and other commonly assessed clinical MRI stroke metrics at acute timepoints. The lesioned MCAO territory in the pig model was anatomically similar to human ischemic stroke patients and resulted in comparable functional outcomes, supporting the pig as a robust ischemic stroke model. It is important to note that other key elements such as functional and structural connectivity may also be critical components in predicting functional outcomes and should be further explored in future studies [62-64]. Nevertheless, using stroke location to improve outcome prediction is rapidly evolving in clinical practice. Currently, the use of stroke location to predict functional outcomes is under assessed in animal models that tend to report traditional metrics such as lesion volumes and midline shifts. Increased frequency of the identification of stroke lesion topology correlated to functional outcomes in preclinical animal models may lead to greater clinical translatability. Improving the accuracy and precision of clinical prognoses is critically important in evidence-

based clinical decision-making after stroke to improve acute patient care, develop long-term treatment plans (e.g., rehabilitation programs), and determine required living assistance needs. The findings of this study support the premise of including a structural injury component in acute MRI assessment to improve clinical prognostication.

4.5 REFERENCES

1 Lin, C., Chatterjee, N., Lee, J., Harvey, R. & Prabhakaran, S. Predictive value of the combination of lesion location and volume of ischemic infarction with rehabilitation outcomes. *Neuroradiology* **61**, 1131-1136, doi:10.1007/s00234-019-02234-9 (2019).

2 Walcott, B. P. *et al.* Outcomes in severe middle cerebral artery ischemic stroke. *Neurocrit Care* **21**, 20-26, doi:10.1007/s12028-013-9838-x (2014).

3 Lovblad, K. O. *et al.* Ischemic lesion volumes in acute stroke by diffusion-weighted magnetic resonance imaging correlate with clinical outcome. *Ann Neurol* **42**, 164-170, doi:10.1002/ana.410420206 (1997).

4 Schiemanck, S. K. *et al.* Ischemic lesion volume correlates with long-term functional outcome and quality of life of middle cerebral artery stroke survivors. *Restor Neurol Neurosci* **23**, 257-263 (2005).

5 Schiemanck, S. K., Post, M. W., Witkamp, T. D., Kappelle, L. J. & Prevo, A. J. Relationship between ischemic lesion volume and functional status in the 2nd week after middle cerebral artery stroke. *Neurorehabil Neural Repair* **19**, 133-138, doi:10.1177/1545968305019002O7 (2005).

6 Cheng, B. *et al.* Influence of stroke infarct location on functional outcome measured by the modified rankin scale. *Stroke* **45**, 1695-1702, doi:10.1161/STROKEAHA.114.005152 (2014).

7 Ernst, M. *et al.* Association of Computed Tomography Ischemic Lesion Location With Functional Outcome in Acute Large Vessel Occlusion Ischemic Stroke. *Stroke* **48**, 2426-2433, doi:10.1161/STROKEAHA.117.017513 (2017).

8 Vora, N. A. *et al.* A 5-item scale to predict stroke outcome after cortical middle cerebral artery territory infarction: validation from results of the Diffusion and Perfusion Imaging Evaluation for Understanding Stroke Evolution (DEFUSE) Study. *Stroke* **42**, 645-649, doi:10.1161/STROKEAHA.110.596312 (2011).

9 Borich, M. R., Brodie, S. M., Gray, W. A., Ionta, S. & Boyd, L. A. Understanding the role of the primary somatosensory cortex: Opportunities for rehabilitation. *Neuropsychologia* **79**, 246-255, doi:10.1016/j.neuropsychologia.2015.07.007 (2015).

10 Cheng, B. *et al.* Dynamics of regional distribution of ischemic lesions in middle cerebral artery trunk occlusion relates to collateral circulation. *J Cereb Blood Flow Metab* **31**, 36-40, doi:10.1038/jcbfm.2010.185 (2011).

11 Phan, T. G., Fong, A. C., Donnan, G. A., Srikanth, V. & Reutens, D. C. Digital probabilistic atlas of the border region between the middle and posterior cerebral arteries. *Cerebrovasc Dis* **27**, 529-536, doi:10.1159/000214215 (2009).

12 Menezes, N. M. *et al.* The real estate factor: quantifying the impact of infarct location on stroke severity. *Stroke* **38**, 194-197, doi:10.1161/01.STR.0000251792.76080.45 (2007).

13 Munsch, F. *et al.* Stroke Location Is an Independent Predictor of Cognitive Outcome. *Stroke* **47**, 66-73, doi:10.1161/STROKEAHA.115.011242 (2016).

14 Wu, O. *et al.* Role of Acute Lesion Topography in Initial Ischemic Stroke Severity and Long-Term Functional Outcomes. *Stroke* **46**, 2438-2444, doi:10.1161/STROKEAHA.115.009643 (2015).

15 Phan, T. G. *et al.* Proof of concept study: relating infarct location to stroke disability in the NINDS rt-PA trial. *Cerebrovasc Dis* **35**, 560-565, doi:10.1159/000351147 (2013).

16 Laredo, C. *et al.* Prognostic Significance of Infarct Size and Location: The Case of Insular Stroke. *Sci Rep* **8**, 9498, doi:10.1038/s41598-018-27883-3 (2018).

17 Timpone, V. M. *et al.* Percentage insula ribbon infarction of >50% identifies patients likely to have poor clinical outcome despite small DWI infarct volume. *AJNR Am J Neuroradiol* **36**, 40-45, doi:10.3174/ajnr.A4091 (2015).

18 Payabvash, S., Taleb, S., Benson, J. C. & McKinney, A. M. Acute Ischemic Stroke Infarct Topology: Association with Lesion Volume and Severity of Symptoms at Admission and Discharge. *AJNR Am J Neuroradiol* **38**, 58-63, doi:10.3174/ajnr.A4970 (2017).

19 Fisher, M. *et al.* Update of the stroke therapy academic industry roundtable preclinical recommendations. *Stroke* **40**, 2244-2250, doi:10.1161/STROKEAHA.108.541128 (2009).

20 McBride, D. W. & Zhang, J. H. Precision Stroke Animal Models: the Permanent MCAO Model Should Be the Primary Model, Not Transient MCAO. *Transl Stroke Res*, doi:10.1007/s12975-017-0554-2 (2017).

21 Lind, N. M. *et al.* The use of pigs in neuroscience: modeling brain disorders. *Neurosci Biobehav Rev* **31**, 728-751, doi:10.1016/j.neubiorev.2007.02.003 (2007).

22 Gieling, E. T., Schuurman, T., Nordquist, R. E. & van der Staay, F. J. The pig as a model animal for studying cognition and neurobehavioral disorders. *Curr Top Behav Neurosci* **7**, 359-383, doi:10.1007/7854_2010_112 (2011).

23 Saikali, S. *et al.* A three-dimensional digital segmented and deformable brain atlas of the domestic pig. *J Neurosci Methods* **192**, 102-109, doi:10.1016/j.jneumeth.2010.07.041 (2010).

24 Ulyanova, A. V. *et al.* Electrophysiological Signature Reveals Laminar Structure of the Porcine Hippocampus. *eNeuro* **5**, doi:10.1523/ENEURO.0102-18.2018 (2018).

25 Holm, I. E. & West, M. J. Hippocampus of the domestic pig: a stereological study of subdivisional volumes and neuron numbers. *Hippocampus* **4**, 115-125, doi:10.1002/hipo.450040112 (1994).

26 Matsas, R., Kenny, A. J. & Turner, A. J. An immunohistochemical study of endopeptidase-24.11 ("enkephalinase") in the pig nervous system. *Neuroscience* **18**, 991-1012, doi:10.1016/0306-4522(86)90113-2 (1986).

27 Hof PR, Y. W., Bloom FE, Belichenko PV, Celio MR. (Elsevier, Amsterdam, 2000).

28 A, P. Vol. Ninth Edition (Williams and Wilkins, Baltimore, 1996).

29 Baker, E. W. *et al.* Induced Pluripotent Stem Cell-Derived Neural Stem Cell Therapy Enhances Recovery in an Ischemic Stroke Pig Model. *Sci Rep* **7**, 10075, doi:10.1038/s41598-017-10406-x (2017).

30 Kaiser, E. E. *et al.* Characterization of tissue and functional deficits in a clinically translational pig model of acute ischemic stroke. *Brain Res* **1736**, 146778, doi:10.1016/j.brainres.2020.146778 (2020).

31 Platt, S. R. *et al.* Development and characterization of a Yucatan miniature biomedical pig permanent middle cerebral artery occlusion stroke model. *Exp Transl Stroke Med* **6**, 5, doi:10.1186/2040-7378-6-5 (2014).

32 Webb, R. L. *et al.* Human Neural Stem Cell Extracellular Vesicles Improve Recovery in a Porcine Model of Ischemic Stroke. *Stroke* **49**, 1248-1256, doi:10.1161/STROKEAHA.117.020353 (2018).

33 Kaiser, E. E. & West, F. D. Large animal ischemic stroke models: replicating human stroke pathophysiology. *Neural Regen Res* **15**, 1377-1387, doi:10.4103/1673-5374.274324 (2020).

34 Spellicy, S. E. *et al.* Neural Stem Cell Extracellular Vesicles Disrupt Midline Shift Predictive Outcomes in Porcine Ischemic Stroke Model. *Transl Stroke Res*, doi:10.1007/s12975-019-00753-4 (2019).

35 Beyaert, C., Vasa, R. & Frykberg, G. E. Gait post-stroke: Pathophysiology and rehabilitation strategies. *Neurophysiol Clin* **45**, 335-355, doi:10.1016/j.neucli.2015.09.005 (2015).

36 Balaban, B. & Tok, F. Gait disturbances in patients with stroke. *PM R* **6**, 635-642, doi:10.1016/j.pmrj.2013.12.017 (2014).

37 Duberstein, K. J. *et al.* Gait analysis in a pre- and post-ischemic stroke biomedical pig model. *Physiol Behav* **125**, 8-16, doi:10.1016/j.physbeh.2013.11.004 (2014).

38 Stewart, J. C. *et al.* Role of corpus callosum integrity in arm function differs based on motor severity after stroke. *Neuroimage Clin* **14**, 641-647, doi:10.1016/j.nicl.2017.02.023 (2017).

39 Wang, L. E. *et al.* Degeneration of corpus callosum and recovery of motor function after stroke: a multimodal magnetic resonance imaging study. *Hum Brain Mapp* **33**, 2941-2956, doi:10.1002/hbm.21417 (2012).

40 Kim, B. J. *et al.* Magnetic resonance imaging in acute ischemic stroke treatment. *J Stroke* **16**, 131-145, doi:10.5853/jos.2014.16.3.131 (2014).

41 Thijs, V. N. *et al.* Is early ischemic lesion volume on diffusion-weighted imaging an independent predictor of stroke outcome? A multivariable analysis. *Stroke* **31**, 2597-2602, doi:10.1161/01.str.31.11.2597 (2000).

42 Saver, J. L. *et al.* Infarct volume as a surrogate or auxiliary outcome measure in ischemic stroke clinical trials. The RANTTAS Investigators. *Stroke* **30**, 293-298, doi:10.1161/01.str.30.2.293 (1999).

43 Lau, V. W., Platt, S. R., Grace, H. E., Baker, E. W. & West, F. D. Human iNPC therapy leads to improvement in functional neurologic outcomes in a pig ischemic stroke model. *Brain Behav* **8**, e00972, doi:10.1002/brb3.972 (2018).

44 Navarro-Orozco, D. & Sanchez-Manso, J. C. in *StatPearls* (2020).

45 Nogles, T. E. & Galuska, M. A. in *StatPearls* (2020).

46 Payabvash, S. *et al.* Location-weighted CTP analysis predicts early motor improvement in stroke: a preliminary study. *Neurology* **78**, 1853-1859, doi:10.1212/WNL.0b013e318258f799 (2012).

47 Payabvash, S. *et al.* Regional ischemic vulnerability of the brain to hypoperfusion: the need for location specific computed tomography perfusion thresholds in acute stroke patients. *Stroke* **42**, 1255-1260, doi:10.1161/STROKEAHA.110.600940 (2011).

48 Kito, G. *et al.* Experimental thromboembolic stroke in cynomolgus monkey. *J Neurosci Methods* **105**, 45-53, doi:10.1016/s0165-0270(00)00351-4 (2001).

49 Titianova, E. B., Pitkanen, K., Paakkonen, A., Sivenius, J. & Tarkka, I. M. Gait characteristics and functional ambulation profile in patients with chronic unilateral stroke. *Am J Phys Med Rehabil* **82**, 778-786; quiz 787-779, 823, doi:10.1097/01.PHM.0000087490.74582.E0 (2003).

50 Lang, C. E., Bland, M. D., Bailey, R. R., Schaefer, S. Y. & Birkenmeier, R. L. Assessment of upper extremity impairment, function, and activity after stroke: foundations for clinical decision making. *J Hand Ther* **26**, 104-114;quiz 115, doi:10.1016/j.jht.2012.06.005 (2013).

51 Langhorne, P., Coupar, F. & Pollock, A. Motor recovery after stroke: a systematic review. *Lancet Neurol* **8**, 741-754, doi:10.1016/S1474-4422(09)70150-4 (2009).

52 Riley, J. D. *et al.* Anatomy of stroke injury predicts gains from therapy. *Stroke* **42**, 421-426, doi:10.1161/STROKEAHA.110.599340 (2011).

53 Saga, Y., Hoshi, E. & Tremblay, L. Roles of Multiple Globus Pallidus Territories of Monkeys and Humans in Motivation, Cognition and Action: An Anatomical, Physiological and Pathophysiological Review. *Front Neuroanat* **11**, 30, doi:10.3389/fnana.2017.00030 (2017).

54 Blair, C. Educating executive function. *Wiley Interdiscip Rev Cogn Sci* **8**, doi:10.1002/wcs.1403 (2017).

55 Sherman, S. M. Functioning of Circuits Connecting Thalamus and Cortex. *Compr Physiol* **7**, 713-739, doi:10.1002/cphy.c160032 (2017).

56 Gillies, M. J. *et al.* The Cognitive Role of the Globus Pallidus interna; Insights from Disease States. *Exp Brain Res* **235**, 1455-1465, doi:10.1007/s00221-017-4905-8 (2017).

57 Ng, Y. S., Stein, J., Ning, M. & Black-Schaffer, R. M. Comparison of clinical characteristics and functional outcomes of ischemic stroke in different vascular territories. *Stroke* **38**, 2309-2314, doi:10.1161/STROKEAHA.106.475483 (2007).

58 Furlanis, G. *et al.* Ischemic Volume and Neurological Deficit: Correlation of Computed Tomography Perfusion with the National Institutes of Health Stroke Scale Score in Acute

Ischemic Stroke. *J Stroke Cerebrovasc Dis* **27**, 2200-2207, doi:10.1016/j.jstrokecerebrovasdis.2018.04.003 (2018).

59 Ernst, M. *et al.* Impact of Ischemic Lesion Location on the mRS Score in Patients with Ischemic Stroke: A Voxel-Based Approach. *AJNR Am J Neuroradiol* **39**, 1989-1994, doi:10.3174/ajnr.A5821 (2018).

60 Lo, R., Gitelman, D., Levy, R., Hulvershorn, J. & Parrish, T. Identification of critical areas for motor function recovery in chronic stroke subjects using voxel-based lesion symptom mapping. *Neuroimage* **49**, 9-18, doi:10.1016/j.neuroimage.2009.08.044 (2010).

61 Koch, S. *et al.* Atlas registration for edema-corrected MRI lesion volume in mouse stroke models. *J Cereb Blood Flow Metab* **39**, 313-323, doi:10.1177/0271678X17726635 (2019).

62 Ktena, S. I. *et al.* Brain Connectivity Measures Improve Modeling of Functional Outcome After Acute Ischemic Stroke. *Stroke* **50**, 2761-2767, doi:10.1161/STROKEAHA.119.025738 (2019).

63 Etherton, M. R. *et al.* White Matter Integrity and Early Outcomes After Acute Ischemic Stroke. *Transl Stroke Res* **10**, 630-638, doi:10.1007/s12975-019-0689-4 (2019).

64 Zhang, J. *et al.* Disrupted structural and functional connectivity networks in ischemic stroke patients. *Neuroscience* **364**, 212-225, doi:10.1016/j.neuroscience.2017.09.009 (2017).

65 Vannucci, S. J. & Hurn, P. D. Gender differences in pediatric stroke: is elevated testosterone a risk factor for boys? *Ann Neurol* **66**, 713-714, doi:10.1002/ana.21925 (2009).

66 Hawk, T., Zhang, Y. Q., Rajakumar, G., Day, A. L. & Simpkins, J. W. Testosterone increases and estradiol decreases middle cerebral artery occlusion lesion size in male rats. *Brain Res* **796**, 296-298, doi:10.1016/s0006-8993(98)00327-8 (1998).

67 Manwani, B. & McCullough, L. D. Sexual dimorphism in ischemic stroke: lessons from the laboratory. *Womens Health (Lond)* **7**, 319-339, doi:10.2217/whe.11.22 (2011).

68 Lisabeth, L. & Bushnell, C. Stroke risk in women: the role of menopause and hormone therapy. *Lancet Neurol* **11**, 82-91, doi:10.1016/S1474-4422(11)70269-1 (2012).

69 Platt, S. R. *et al.* Development and characterization of a Yucatan miniature biomedical pig permanent middle cerebral artery occlusion stroke model. *Experimental & translational stroke medicine* **6**, 5-5, doi:10.1186/2040-7378-6-5 (2014).

70 Li, X., Morgan, P. S., Ashburner, J., Smith, J. & Rorden, C. The first step for neuroimaging data analysis: DICOM to NIfTI conversion. *J Neurosci Methods* **264**, 47-56, doi:10.1016/j.jneumeth.2016.03.001 (2016).

71 Fedorov, A. *et al.* 3D Slicer as an image computing platform for the Quantitative Imaging Network. *Magn Reson Imaging* **30**, 1323-1341, doi:10.1016/j.mri.2012.05.001 (2012).

72 Ashburner, J. *et al.* SPM12 manual. *URL: http://www. fil. ion. ucl. ac. uk/spm/doc/spm12 manual. pdf* (2016).

73 Ashburner, J. & Friston, K. Multimodal image coregistration and partitioning--a unified framework. *Neuroimage* **6**, 209-217, doi:10.1006/nimg.1997.0290 (1997).

74 Ashburner, J. & Friston, K. J. Nonlinear spatial normalization using basis functions. *Hum Brain Mapp* **7**, 254-266 (1999).

75 Jenkinson, M., Beckmann, C. F., Behrens, T. E., Woolrich, M. W. & Smith, S. M. Fsl. *Neuroimage* **62**, 782-790, doi:10.1016/j.neuroimage.2011.09.015 (2012).

76 Smith, S. M. *et al.* Advances in functional and structural MR image analysis and implementation as FSL. *Neuroimage* **23 Suppl 1**, S208-219, doi:10.1016/j.neuroimage.2004.07.051 (2004).

77 Woolrich, M. W. *et al.* Bayesian analysis of neuroimaging data in FSL. *Neuroimage* **45**, S173-186, doi:10.1016/j.neuroimage.2008.10.055 (2009).

78 Rueden, C. T. *et al.* ImageJ2: ImageJ for the next generation of scientific image data. *BMC Bioinformatics* **18**, 529, doi:10.1186/s12859-017-1934-z (2017).

79 Schindelin, J. *et al.* Fiji: an open-source platform for biological-image analysis. *Nat Methods* **9**, 676-682, doi:10.1038/nmeth.2019 (2012).

Acknowledgements

We would like to thank Dr. E. Kaiser, Dr. G. Kim, Dr. J. Mumaw, Dr. E. Howerth, X. Fang, J. Jeon, E. Karstedt, K. McClanahan, L. Reno, and M. Wendzik for assistance with pig care, K. Mason for MRI technical assistance, Dr. S. Platt for performing stroke surgeries, and T. Ellison and C. Temple for assistance with data analysis. We would also like to thank our team of undergraduate researchers: M. Alcalde-Santa Ana, W. Anand, J. Bourbo, T. Burnette, A. Cieszewski, L. Francis, Z. Jones, J. Johnston, Z. Oberholzer, L. Parker, S. Patel, S. Radhakrishnan, H. Rasheed, S. Shin, A. Simmons, E. Smith, M. Snyder, H. Stavas, C. Temple, B. Winkler, and J. Winkler, we could not have done this research without your help. Research reported in this publication was supported by the National Institutes of Health under award number **1R43NS103596-01**.

Authors' contribution statement

KMS, BJJ, SLS, and FDW wrote and edited the manuscript. KMS, BJJ, SESp, EWB, HAK, SLS, and FDW participated in study design. KMS, BJJ, and ESW performed pig work. JAG

performed ovariectomy surgeries on female pigs. KMS, GAS, SESn, and QZ performed MRI analysis. KMS and BJJ performed statistical tests. All authors reviewed the manuscript.

Competing interests statement

SLS is a stockholder in Aruna Bio Inc and was a part-time employee of Aruna Bio Inc during the study. EWB was a full-time employee of Aruna Bio Inc during the study. All other authors declare no competing interests.

Data availability statement

Data and MatLab code is available at https://zenodo.org/. [10.5281/zenodo.4339189]

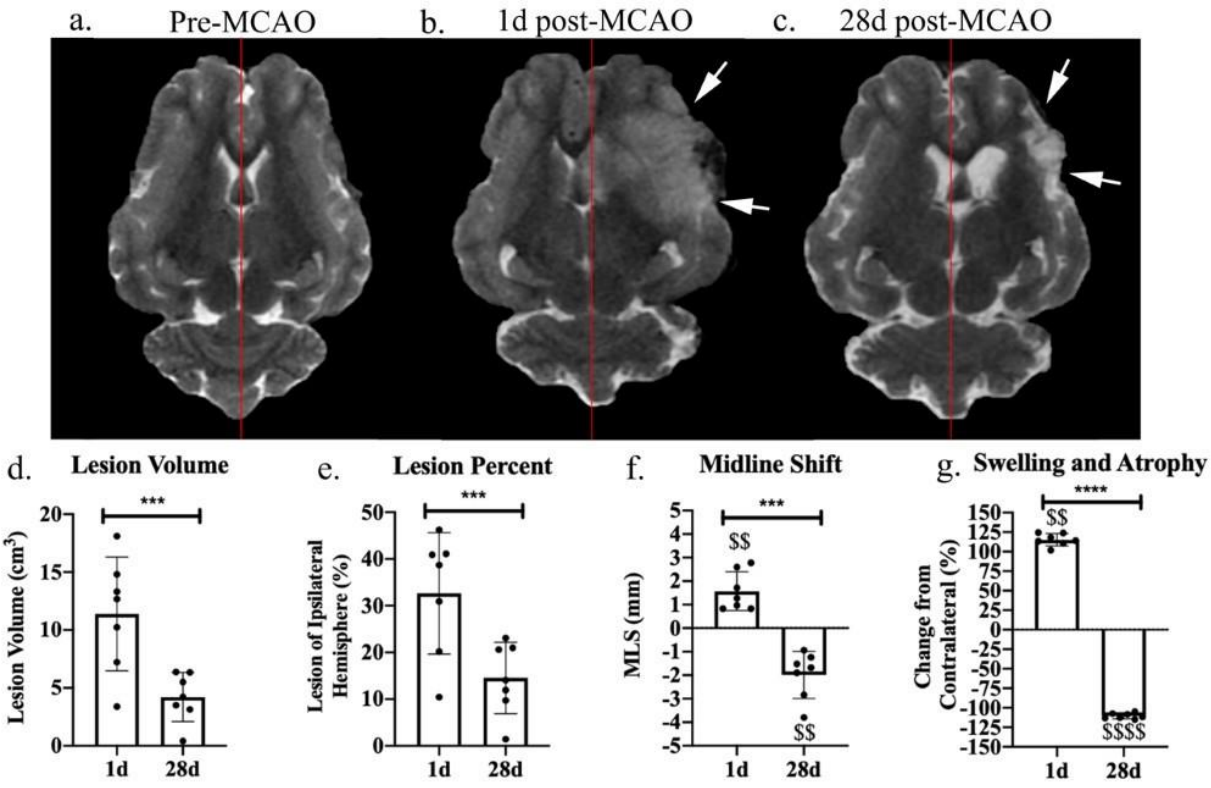

Figure 4.1: Canonical MRI measurements of MCAO induced ischemic stroke at 1d and 28d post-MCAO. T2W images prior to MCAO reveal homology between the hemispheres (**a**). At 1d (**b**) and 28d (**c**) post-MCAO, T2W images exhibited territorial hyperintense lesions indicated by white arrows and a shift from the natural midline (red lines indicate natural midline). Lesion volume (**d**), lesion volume as a percent of the ipsilateral hemisphere (**e**), midline shift (MLS) (**f**), and hemispheric changes (**g**) were quantified at 1d and 28d post-MCAO. *** and **** indicated statistically different between timepoints. $$ and $$$$ indicated statistically different from hypothetical normal.

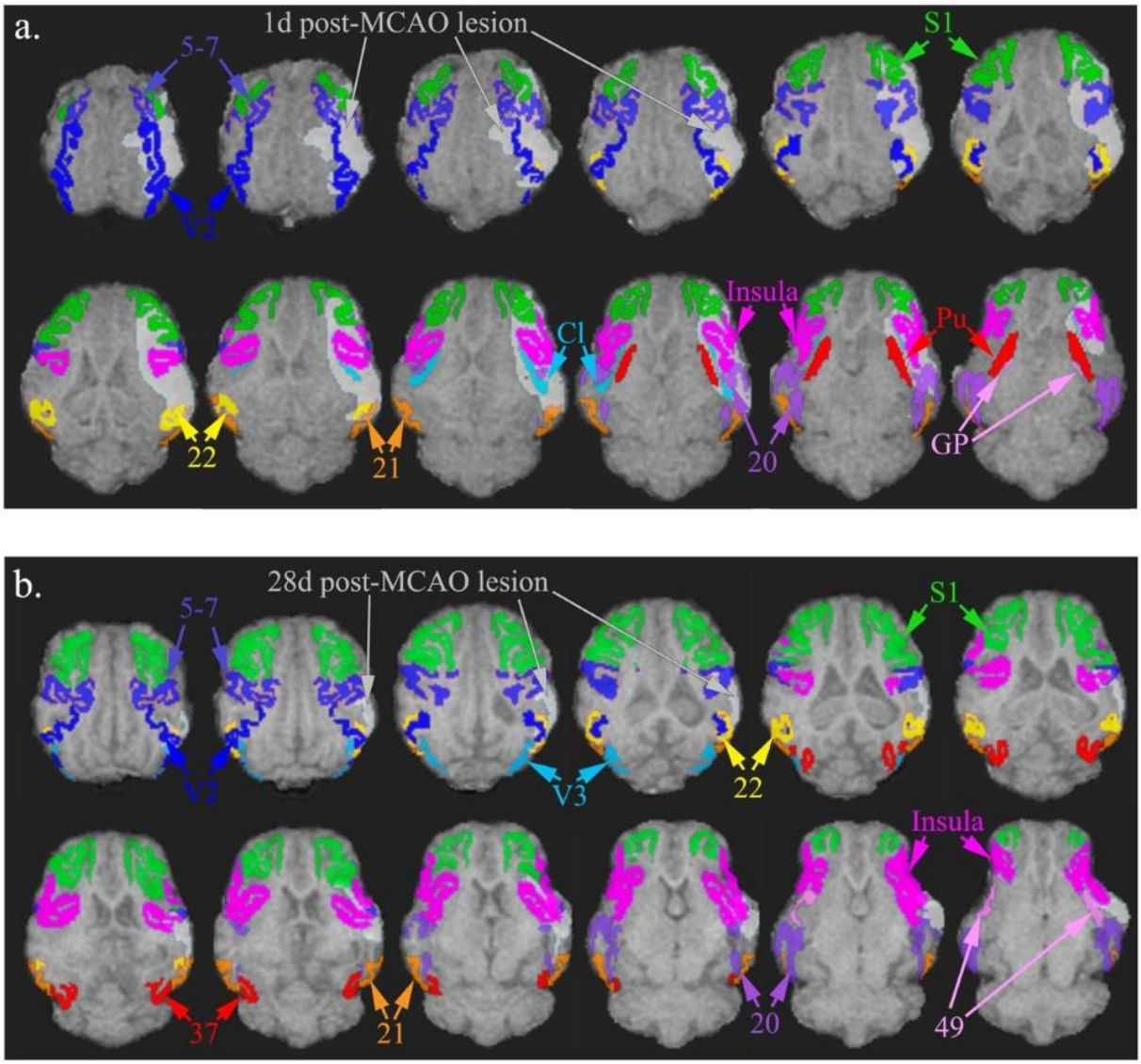

Figure 4.2: Structures most highly lesioned by MCAO in a porcine ischemic stroke model. Images depict axial T1 brain overlay with entire bilateral structures most affected by the lesion. The structures with the highest percentage of infarction (percent of structure, PoS) at 1d post-MCAO in descending order include the claustrum (*Cl*), inferior temporal gyrus (*Brodmann's Area 20*), superior temporal gyrus (*Brodmann's Area 22*), insular cortex (*Insula*), middle temporal gyrus (*Brodmann's Area 21*), putamen (*Pu*), somatosensory association cortex

(*Brodmann's Area 5-7*), secondary visual cortex (*V2*), globus pallidus (*GP*), and primary somatosensory cortex (*S1*) (**a**). At 28d post-MCAO, the structures with the highest level of lesioning included the middle temporal gyrus (*Brodmann's Area 21*), superior temporal gyrus (*Brodmann's Area 22*), inferior temporal gyrus (*Brodmann's Area 20*), somatosensory association cortex (*Brodmann's Area 5-7*), insular cortex (*Insula*), associative visual cortex (*V3*), primary somatosensory cortex (*S1*), prepiriform area (*Brodmann's Area 49*), fusiform gyrus (*Brodmann's Area 37*), and secondary visual cortex (*V2*) (**b**).

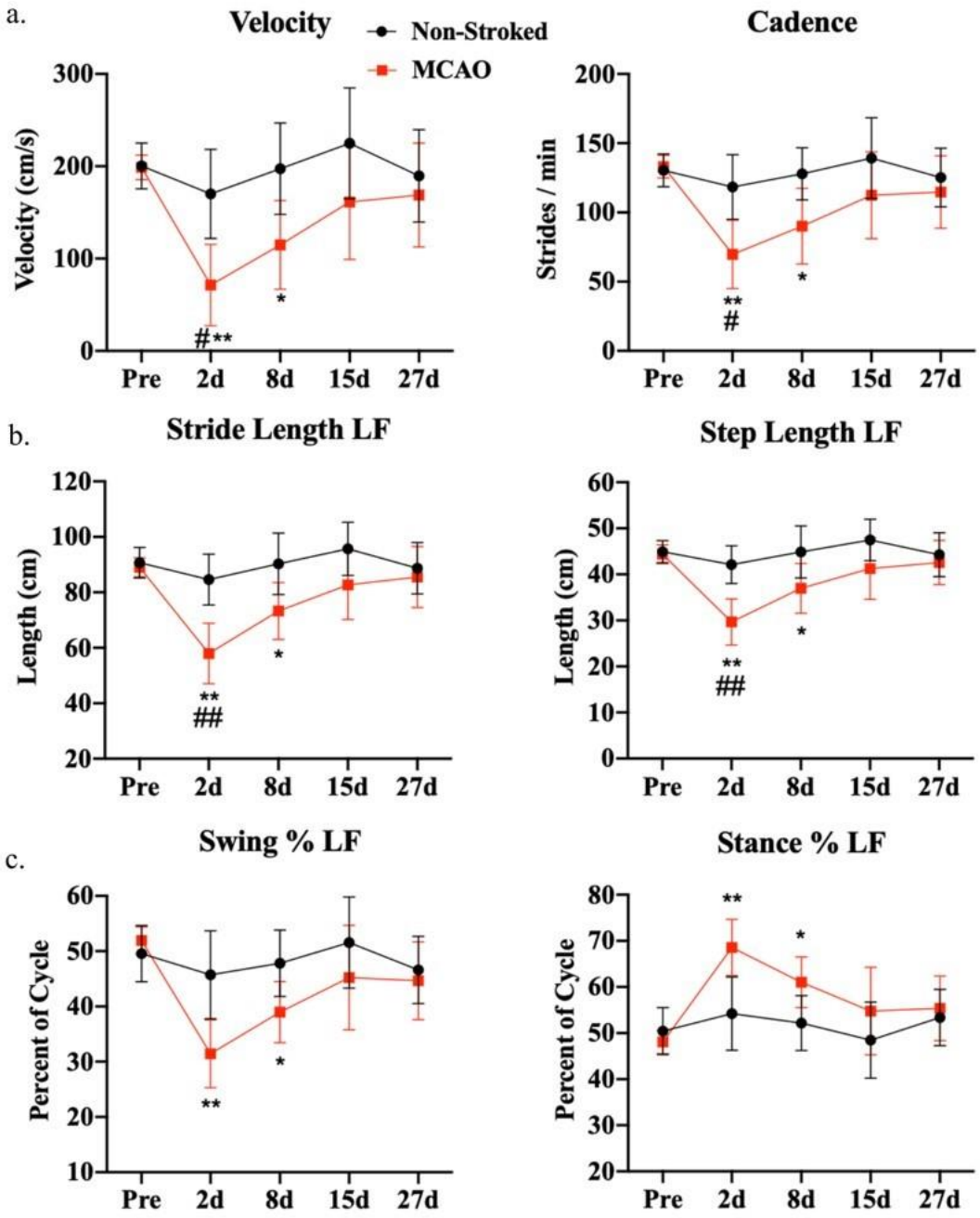

Figure 4.3: MCAO resulted in acute functional gait deficits. At 2d and 8d post-MCAO, MCAO pigs exhibited significant decreases in velocity (**a**), cadence (**a**), stride length (**b**), step length (**b**), swing percent (**c**), and an increase in stance percent (**c**) relative to pre-MCAO values. At 15d and 27d post-MCAO, there were no significant differences compared to pre-

stroke, which was indicative of functional recovery (p>0.05). At 2d post-MCAO, MCAO pigs exhibited significantly different velocity (**a**), cadence (**a**), stride length (**b**), and step length (**b**) relative to non-stroked controls. Non-stroked controls had no significant changes over the course of the study (p>0.05). * and ** indicated statistical difference from pre-MCAO values. # and ## indicated statistically different between groups.

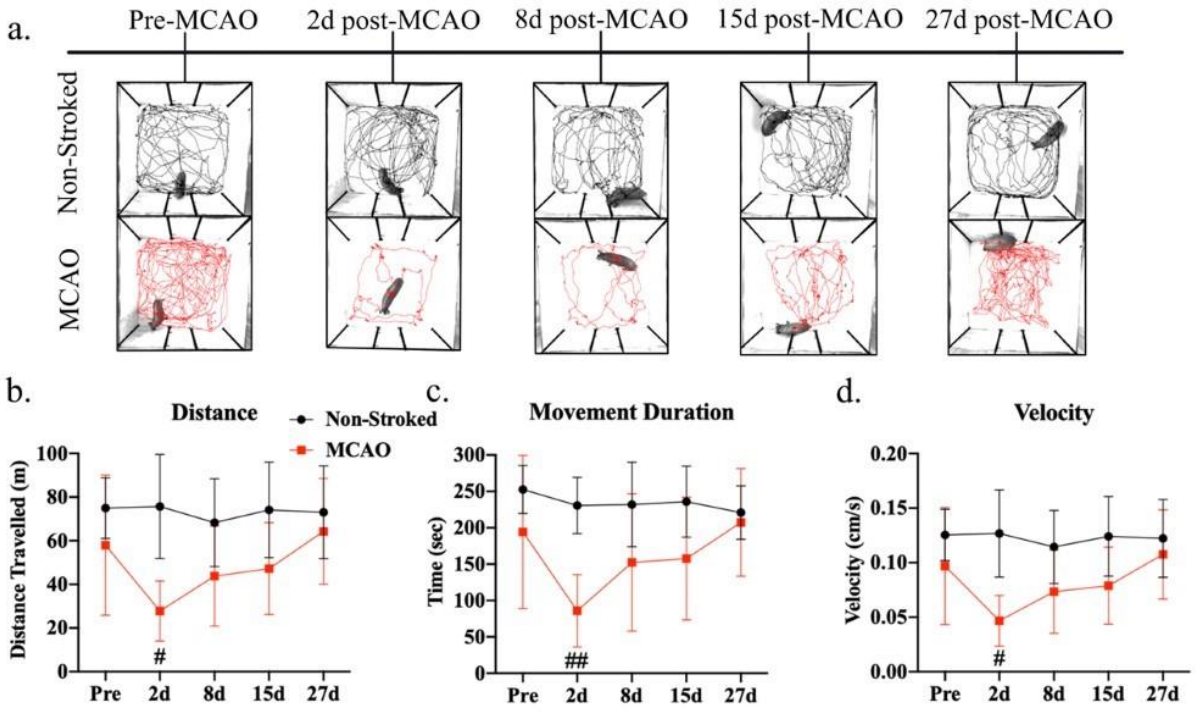

Figure 4.4: Stroke decreased acute voluntary movement in open field behavioral test. Representative 10-min movement tracings shown for non-stroked (black) and MCAO (red) pigs across all time points (**a**). At 2d post-MCAO, MCAO pigs had decreased distance traveled (**b**), movement duration (**c**), and average velocity (**d**) compared to non-stroked pigs. No significant differences were observed at 8d, 15d, and 27d post-MCAO in both groups (p>0.05). # and ## indicated statistically different between groups.

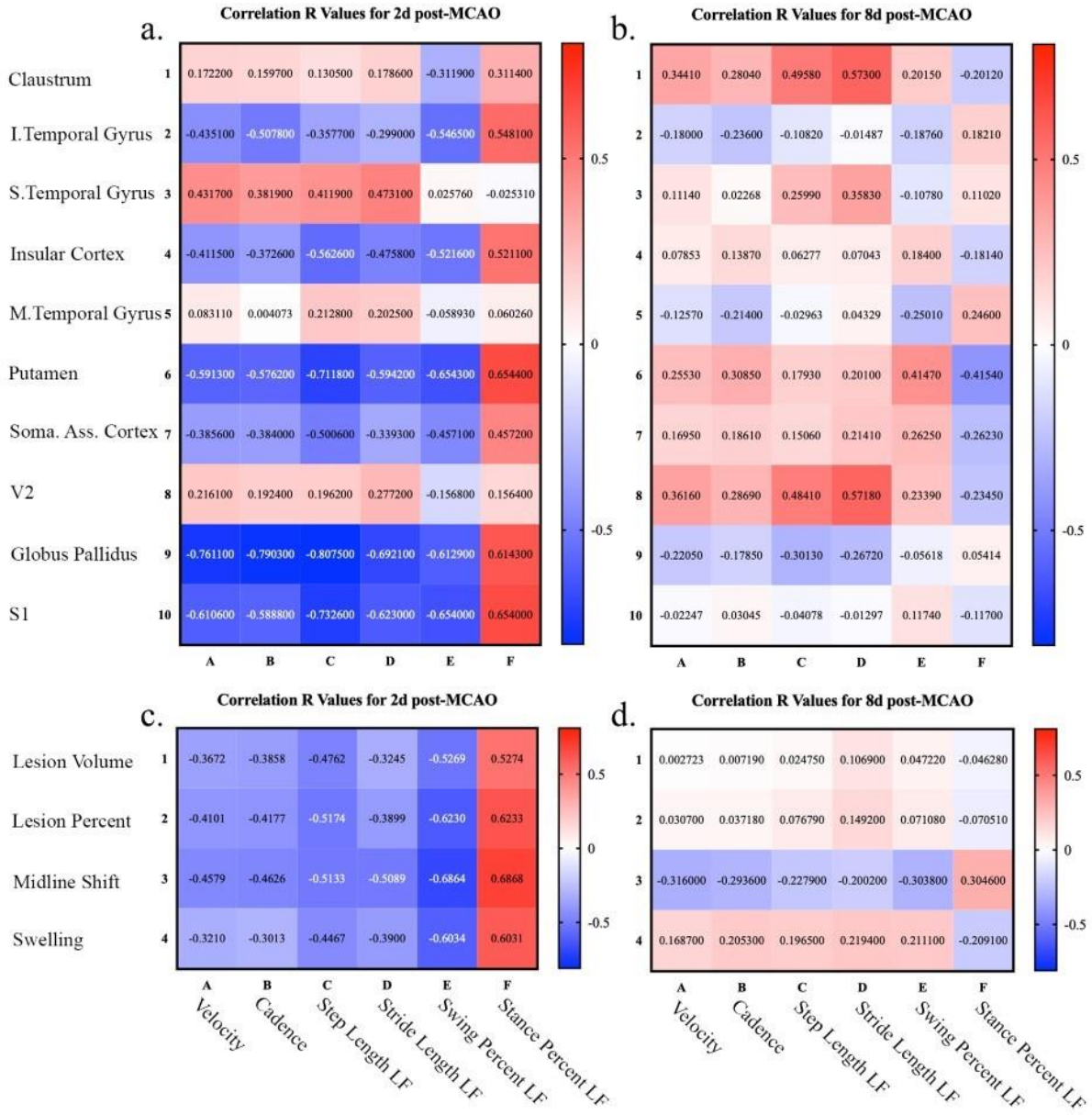

Figure 4.5: Location of stroke lesion in structures associated with motor coordination had prognostic value when evaluating motor functional outcomes. Pearson correlations between top PoS structures impacted by the lesion (y-axis) to gait functional outcomes (x-axis) were

evaluated at 2d post-MCAO (**a**) and 8d post-MCAO (**b**). Pearson correlations between canonical MRI parameters (y-axis), including lesion volume, lesion percent of ipsilateral hemisphere, midline shift, and hemispheric swelling, and gait functional outcomes (x-axis) were evaluated at 2d post-MCAO (**c**) and 8d post-MCAO (**d**). R values were reported with cell color indicating correlation direction and strength. FDR p-values corrected for multiple comparisons can be found in **Supplementary Table 4.3**.

Table 4.1: Percentage of pigs effected with lesion in each structure. Identified structures were separated into regions including the thalamus, striate system, limbic system, and Brodmann's Areas. Activated pixels in each structure signified positive lesion. Lesion locations were identified at 1d and 28d post-MCAO. 100% signifies that all pigs (n=7) had lesion in structure.

Region	**Structure**	**Pigs Effected at 1d Post-MCAO (%)**	**Pigs Effected at 28d Post-MCAO (%)**
Thalamus	Pulvinar Nuclei	42.9	--
	Reticular Thalamic Nucleus	42.9	--
	Ventral Anterior Thalamic Nucleus	14.3	--
	Ventral Posterior Thalamic Nucleus	42.9	--
Striate System	Caudate Nucleus	71.4	--
	Claustrum	100	28.6
	Globus Pallidus	71.4	--
	Putamen	100	14.3
Limbic System	Fornix	85.7	28.6
	Hippocampus	85.7	14.3

	Subiculum	42.9	--
	Amygdala	71.4	28.6
Brodmann's Area	Primary Somatosensory Cortex	71.4	71.4
	Primary Motor Cortex	28.6	--
	Somatosensory Association Cortex	85.7	100
	Dorsolateral Prefrontal Cortex	42.9	14.3
	Anterior Prefrontal Cortex	28.6	--
	Orbitofrontal Cortex	14.3	--
	Insular Cortex	100	85.7
	Primary Visual Cortex	71.4	28.6
	Secondary Visual Cortex	100	85.7
	Associative Visual Cortex	85.7	57.1
	Inferior Temporal Gyrus	100	100
	Middle Temporal Gyrus	85.7	100
	Superior Temporal Gyrus	100	85.7
	Dorsal Anterior Cingulate Cortex	14.3	--
	Anterior Entorhinal Cortex	85.7	14.3
	Parahippocampal Cortex	100	71.4
	Fusiform Gyrus	71.4	42.9
	Prepiriform Area	100	100

Page Break

Supplementary Information

Supplementary Table 3.1: Percent of structure signifies the percent of individual anatomical structure with a lesion. Percent of structure (PoS) was calculated by the total number of activated pixels (lesion) in structure divided by the total number of pixels in structure. Percent of lesion (PoL) signifies the percent of each structure in the identified lesion. PoL was calculated by dividing number of activated pixels per structure by the total number of pixels of the lesion.

	Percent of Structure 1d post-MCAO		**Percent of Structure 28d post-MCAO**		**Percent of Lesion 1d post-MCAO**		**Percent of Lesion 28d post-MCAO**	
Structure	**Mean**	**SD**	**Mean**	**SD**	**Mean**	**SD**	**Mean**	**SD**
Amygdala	24.13	27.18	4.31	8.25	1.23	1.95	0.60	1.03
Anterior Commissure	0.97	2.55	0	0	0.004	0.01	0	0
Anterior Entorhinal Cortex	9.95	9.29	0.16	0.43	0.93	1.66	0.06	0.15
Anterior Prefrontal Cortex	2.43	4.40	0	0	0.19	0.36	0	0
Associative Visual Cortex	15.49	13.95	10.02	14.48	0.54	0.51	0.85	1.03
Caudate Nucleus	7.20	8.73	0	0	0.45	0.62	0	0
Claustrum	65.91	29.68	0.96	2.45	1.94	0.71	0.07	0.17
Corpus Callosum	0.22	0.56	0	0	0.03	0.07	0	0

Dorsal Anterior Cingulate Cortex	0.19	0.51	0	0	0.008	0.02	0	0
Dorsolateral Prefrontal Cortex	1.23	2.05	0.01	0.03	0.07	0.12	0.002	0.006
Fornix	2.93	2.82	0.25	0.53	0.18	0.18	0.08	0.18
Fusiform Gyrus	10.43	12.06	6.82	10.44	0.72	1.31	0.59	0.77
Geniculate Nucleus	0.04	0.12	0	0	0.0004	0.001	0	0
Globus Pallidus	34.52	28.61	0	0	0.59	0.69	0	0
Hippocampus	4.46	3.66	0.46	1.23	0.48	0.68	0.21	0.54
Inferior Temporal Gyrus	62.15	27.67	18.19	13.55	5.16	4.65	3.27	2.72
Insular Cortex	54.45	31.35	15.95	9.28	8.45	5.09	7.95	6.02
Middle Temporal Gyrus	44.43	24.49	39.84	31.80	2.59	2.97	4.23	3.01
Parahippocampal Cortex	12.98	10.99	3.11	3.51	2.06	3.00	1.42	2.34
Piriform Cortex	0	0	0.21	0.54	0	0	0	0
Prepiriform Area	23.76	15.86	7.84	5.85	1.44	1.31	1.30	1.06
Primary Motor Cortex	0.18	0.32	0	0	0.007	0.01	0	0
Primary Somatosensory Cortex	33.48	23.73	8.44	8.92	6.33	4.82	5.65	6.36
Primary Visual Cortex	4.90	6.86	0.02	0.03	1.08	1.36	0.009	0.02
Pulvinar Nuclei	0.53	0.98	0	0	0.008	0.02	0	0

Putamen	44.00	22.23	0.27	0.72	3.22	1.58	0.04	0.11
Reticular Thalamic Nucleus	7.61	9.74	0	0	0.09	0.13	0	0
Orbitofrontal Cortex	0.41	1.08	0	0	0.002	0.004	0	0
Secondary Visual Cortex	40.57	28.62	5.83	6.30	6.02	4.34	2.07	1.93
Somatosensory Association Cortex	43.05	27.06	16.78	11.46	4.98	2.87	5.41	3.59
Subiculum	2.23	3.56	0	0	0.02	0.03	0	0
Superior Temporal Gyrus	58.91	36.32	31.14	17.55	2.36	1.68	3.15	1.87
Ventral Anterior Thalamic Nucleus	0.02	0.06	0	0	0.001	0.002	0	0
Ventral Posterior Thalamic Nucleus	0.29	0.40	0	0	0.004	0.006	0	0

Supplementary Table 4.2: Functional outcomes evaluated. Compiled list of functional outputs with corresponding definitions.

	Gait or Behavior Parameter Measured
Spatial Gait Parameters	▪ Step Length (cm) LF, RF, LH, RH (*Measured between the heel center of the current hoof print to the heel center of the previous hoof print on the opposite foot*) ▪ Stride Length (cm) LF, RF, LH, RH (*Distance between consecutive hoof prints of the same hoof)*

Temporal Gait Parameters	▪ Velocity (*Distance traveled (cm)/sec*) ▪ Cadence (S*trides/min*) ▪ Swing Percent (%) LF, RF, LH, RH *(The percent of 1 full gait cycle in which the limb was in the non-contact phase*) ▪ Stance Percent (%) LF, RF, LH, RH *(The percent of 1 full gait cycle in which the limb was in the contact phase*)
Pressure Gait Parameters	▪ Total Pressure Index LF, RF, LH, RH (*TSP expressed as a percentage of all four limbs. This shows % of weight distribution across all four hoofs*)
Open Field Mobility Behavior Parameters	▪ Distance (m) (*Distance traveled by the pig within the open field arena)* ▪ Velocity (*Distance traveled (cm)/sec*) ▪ Movement Moving Duration (*Elapsed time the running average velocity exceeds the start velocity*)
Modified Rankin Scale Score	Observational behavior assessment modified for a pig. 0 (no residual stroke symptoms) to 6 (death due to stroke). *See Spellicy et al.*[1] *for further information on the scale.*

Supplementary Table 4.3: FDR Corrected P-Values. False discovery rate analysis was completed on original p-values to correct for multiple comparisons.

	2d post-MCAO					
	Velocity	**Cadence**	**Step Length LF**	**Stride Length LF**	**Swing % LF**	**Stance % LF**
Claustrum	0.8134	0.8134	0.8134	0.8134	0.8134	0.8134

Inferior Temporal Gyrus	0.5704	0.5704	0.5704	0.5704	0.5704	0.5704
Superior Temporal Gyrus	0.6893	0.6893	0.6893	0.6893	0.9716	0.9716
Insular Cortex	0.4716	0.4716	0.4716	0.4716	0.4716	0.4716
Middle Temporal Gyrus	1	1	1	1	1	1
Putamen	0.2336	0.2336	0.2336	0.2336	0.2336	0.2336
Somatosensory Association Cortex	0.5156	0.5156	0.5156	0.5156	0.5156	0.5156
Secondary Visual Cortex	0.775	0.775	0.775	0.775	0.775	0.775
Globus Pallidus	0.1592	0.1592	0.1592	0.1933	0.1978	0.1978
Primary Somatosensory Cortex	0.2211	0.2211	0.2211	0.2211	0.2211	0.2211

	8d post-MCAO

	Velocity	Cadence	Step Length LF	Stride Length LF	Swing % LF	Stance % LF
Claustrum	0.6721	0.6721	0.6721	0.6721	0.6721	0.6721
Inferior Temporal Gyrus	0.9846	0.9846	0.9846	0.9846	0.9846	0.9846
Superior Temporal Gyrus	0.9712	0.9712	0.9712	0.9712	0.9712	0.9712
Insular Cortex	0.9026	0.9026	0.9026	0.9026	0.9026	0.9026
Middle Temporal Gyrus	0.9592	0.9592	0.9592	0.9592	0.9592	0.9592
Putamen	0.7074	0.7074	0.7074	0.7074	0.7074	0.7074
Somatosensory Association Cortex	0.7547	0.7547	0.7547	0.7547	0.7547	0.7547
Secondary Visual Cortex	0.6198	0.6198	0.6198	0.6198	0.6198	0.6198
Globus Pallidus	0.9173	0.9173	0.9173	0.9173	0.9173	0.9173
Primary Somatosensory Cortex	0.9879	0.9879	0.9879	0.9879	0.9879	0.9879

	2d post-MCAO					
	Velocity	**Cadence**	**Step Length LF**	**Stride Length LF**	**Swing % LF**	**Stance % LF**
Lesion Volume	0.5356	0.5356	0.5356	0.5356	0.5356	0.5356
Lesion Percent	0.4492	0.4492	0.4492	0.4492	0.4492	0.4492
Midline Shift	0.3648	0.3648	0.3648	0.3648	0.3648	0.3648
Swelling	0.5673	0.5673	0.5673	0.5673	0.5673	0.5673

	8d post-MCAO					
	Velocity	**Cadence**	**Step Length LF**	**Stride Length LF**	**Swing % LF**	**Stance % LF**
Lesion Volume	1	1	1	1	1	1
Lesion Percent	0.9574	0.9574	0.9574	0.9574	0.9574	0.9574
Midline Shift	0.6735	0.6735	0.6735	0.6735	0.6735	0.6735
Swelling	0.7248	0.7248	0.7248	0.7248	0.7248	0.7248

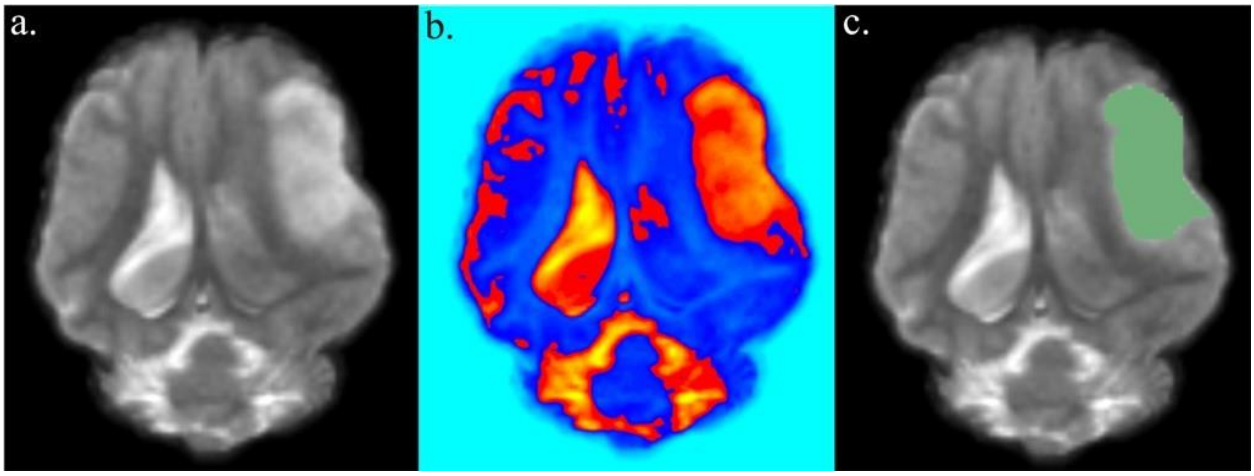

Supplementary Figure 4.1: Method of identifying lesion volume with inversion filter. T2W image (**a**) with a territorial hyperintense lesion in the ipsilateral hemisphere. Inversion filter applied (**b**) and lesion manually outlined in each slice (**c**).

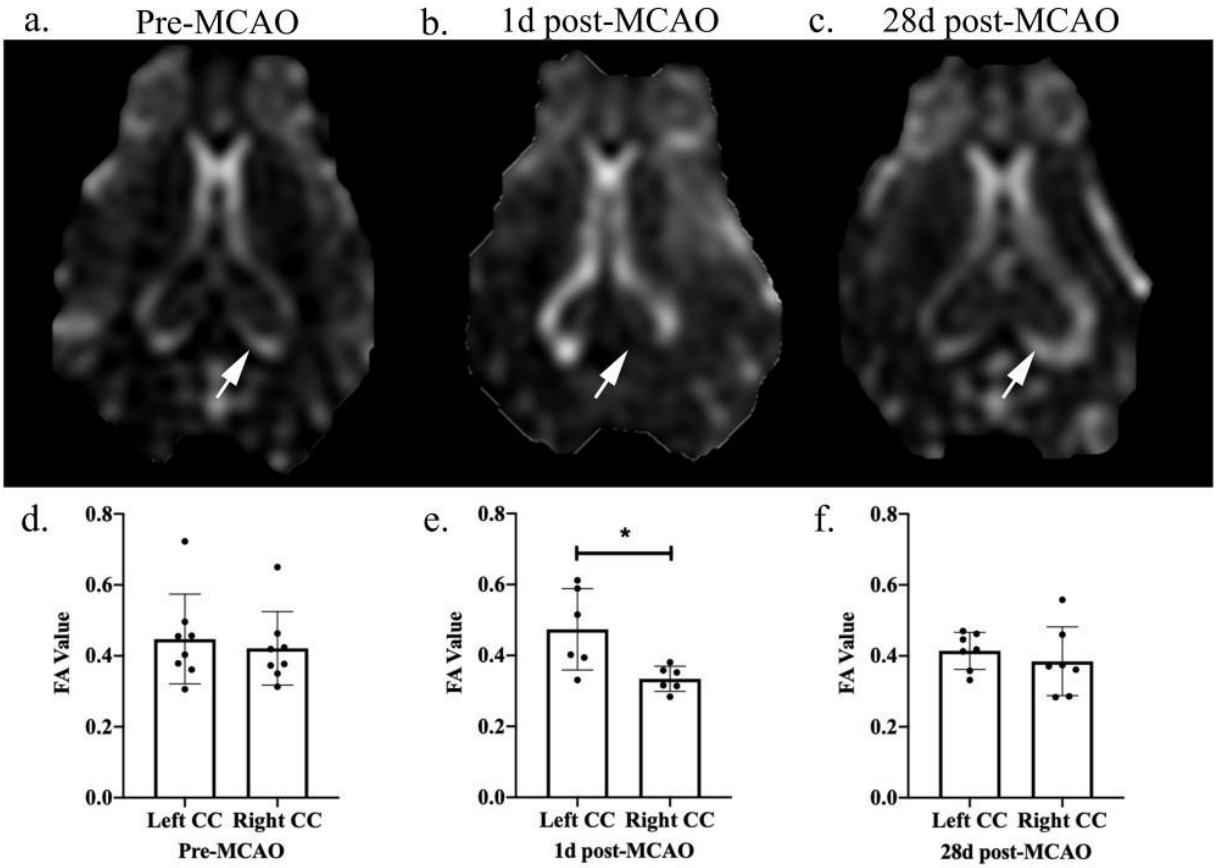

Supplementary Figure 4.2: MCAO results in acute white matter integrity decreases in the corpus callosum. Axial DTI images show an intact corpus callosum (CC) at pre-MCAO (**a**), reduced ipsilateral (right CC) integrity at 1d post-MCAO (**b**), and recovered ipsilateral integrity at 28d post-MCAO (**c**). Pre-MCAO fractional anisotropy (FA) values did not reveal a significant difference between hemispheres (**d**). At 1d post-MCAO, ipsilateral (right) CC FA value was reduced compared to the contralateral (left) CC (**e**). By 28d post-MCAO, FA values had recovered (**f**). * indicated statistical difference between hemispheres.

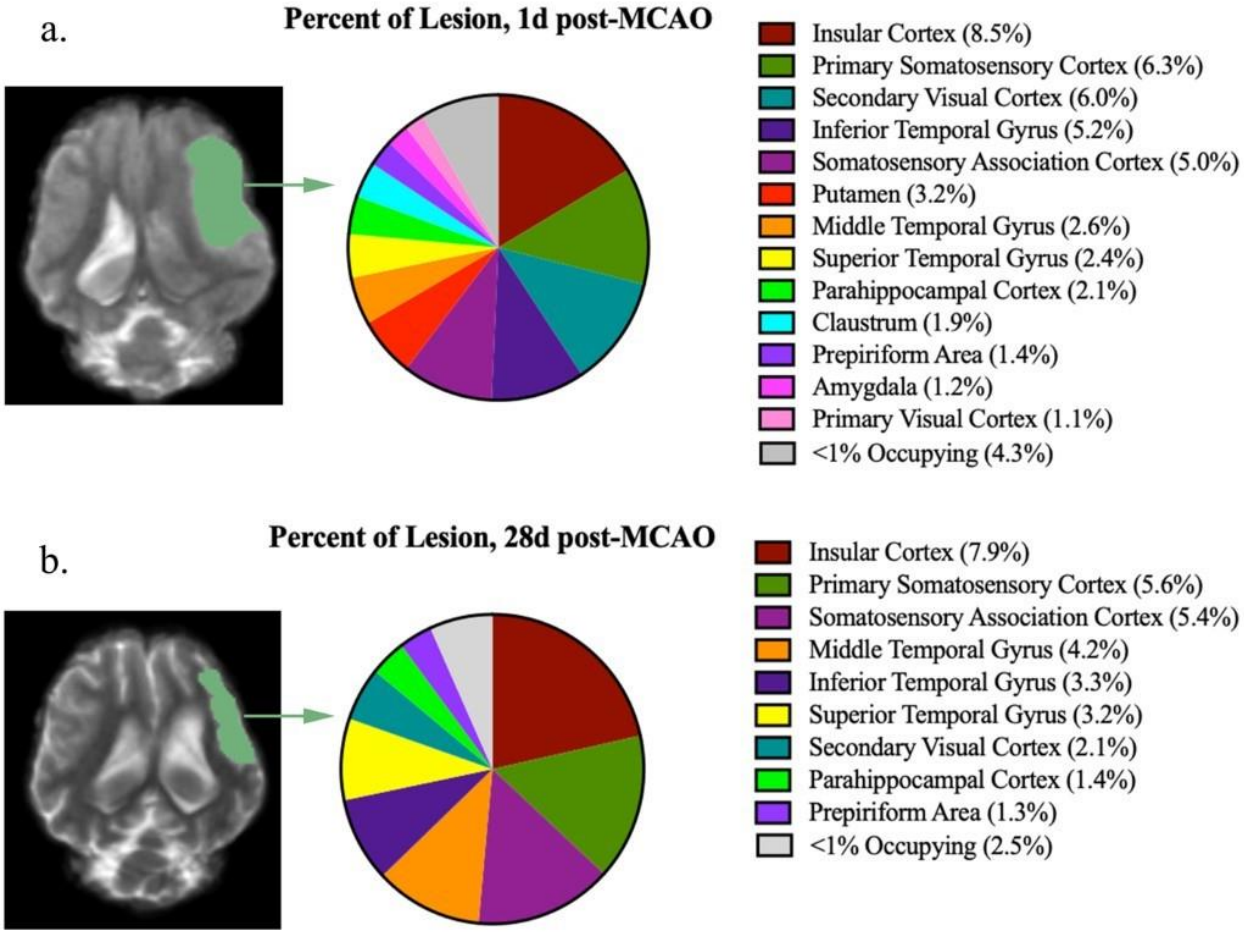

Supplementary Figure 4.3: Percent of identified lesion in effected brain structures. The percent of the identified lesion (PoL) in each structure was quantified to determine the percent of the identified lesion that affected specific brain structures. Summary of the structures occupying the highest percent of lesion measured at 1d post-MCAO (**a**) and at 28d post-MCAO (**b**).

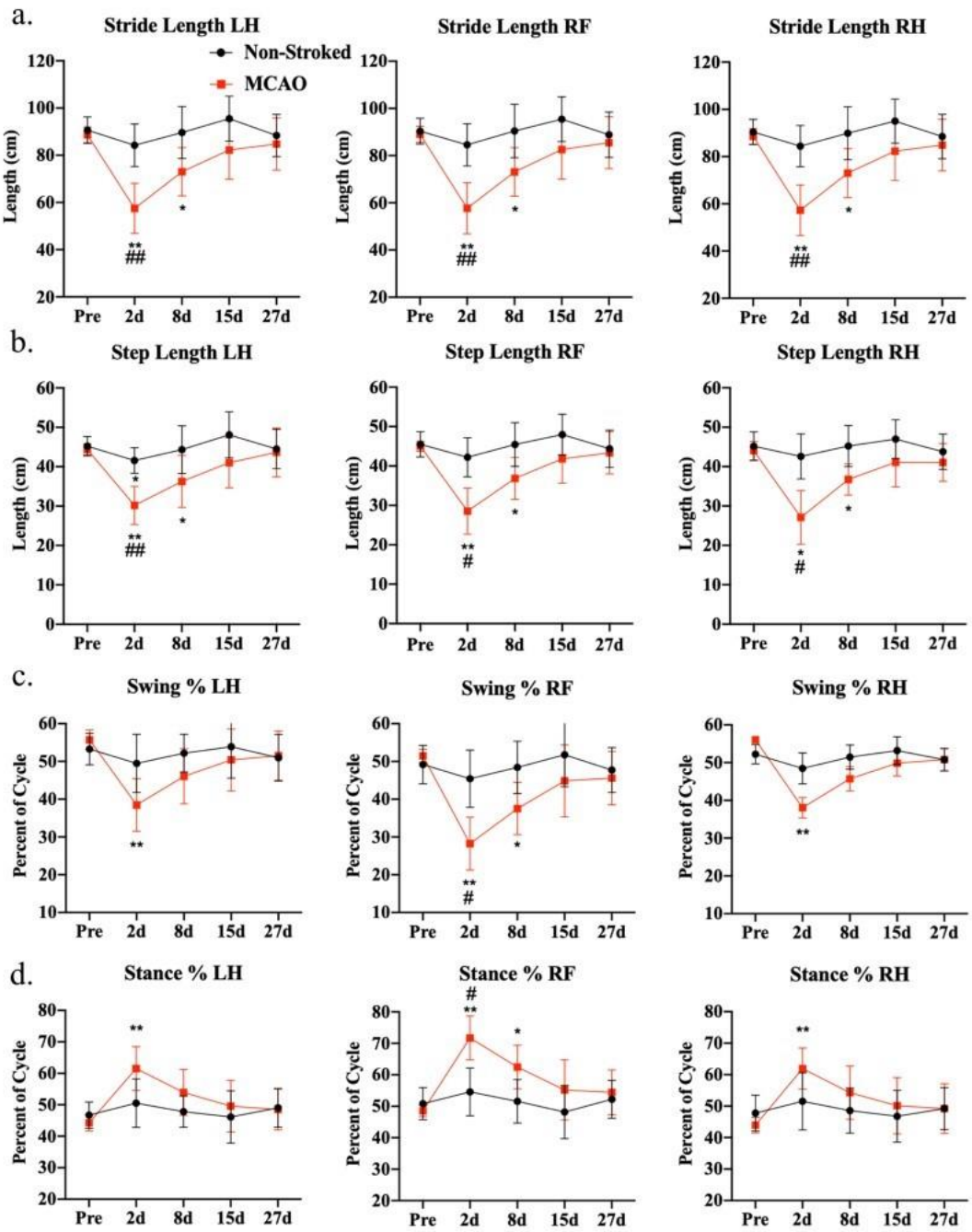

Supplementary Figure 4.4: MCAO resulted in acute deficits in right front, right hind, and left hind spatiotemporal gait parameters. Stride length of the left hind (LH), right front (RF), and right hind (RH), decreased at 2d (p=0.0038, p=0.0037, and p=0.0040, respectively) and 8d (p=0.0290, p=0.0277, and p=0.0325, respectively) post-MCAO compared to pre-MCAO

values (**a**). Stroked animals exhibited a decrease in stride length at 2d post-MCAO compared to non-stroked controls in LH (p=0.0075), RF (p=0.0073), and RH (p=0.0063). Step length of the LH, RF, and RH decreased at 2d (p=0.0017, p=0.0050, and p=0.0104, respectively) and 8d (p=0.0437, p=0.0332, and p=0.0238, respectively) post-MCAO compared to pre-MCAO values (**b**). Stroked animals exhibited a decrease in step length at 2d post-MCAO compared to non-stroked controls in LH (p=0.0067), RF (p=0.0117), and RH (p=0.0135). Swing percent decreased in the LH (p=0.0093), RF (p=0.0033), and RH (p=0.0091) at 2d post-MCAO and in the RF (p=0.0110) at 8d post-MCAO compared to pre-MCAO values (**c**). Stroked animals exhibited a decrease in swing percent at 2d post-MCAO compared to non-stroked controls in RF (p=0.0219). Stance percent increased in the LH (p=0.0093), RF (p=0.0033), and RH (p=0.0091) at 2d post-MCAO and in the RF (p=0.0110) at 8d post-MCAO compared to pre-MCAO values (**d**). Stroked animals exhibited an increase in stance percent at 2d post-MCAO compared to non-stroked controls in RF (p=0.0222). Non-stroked controls had no changes in the measured parameters for the duration of the study (p>0.05), except for step length LH compared to pre-MCAO values at 2d post-MCAO (p=0.0497). * and ** indicated statistical difference from pre-MCAO values. # and ## indicated statistically different between groups.

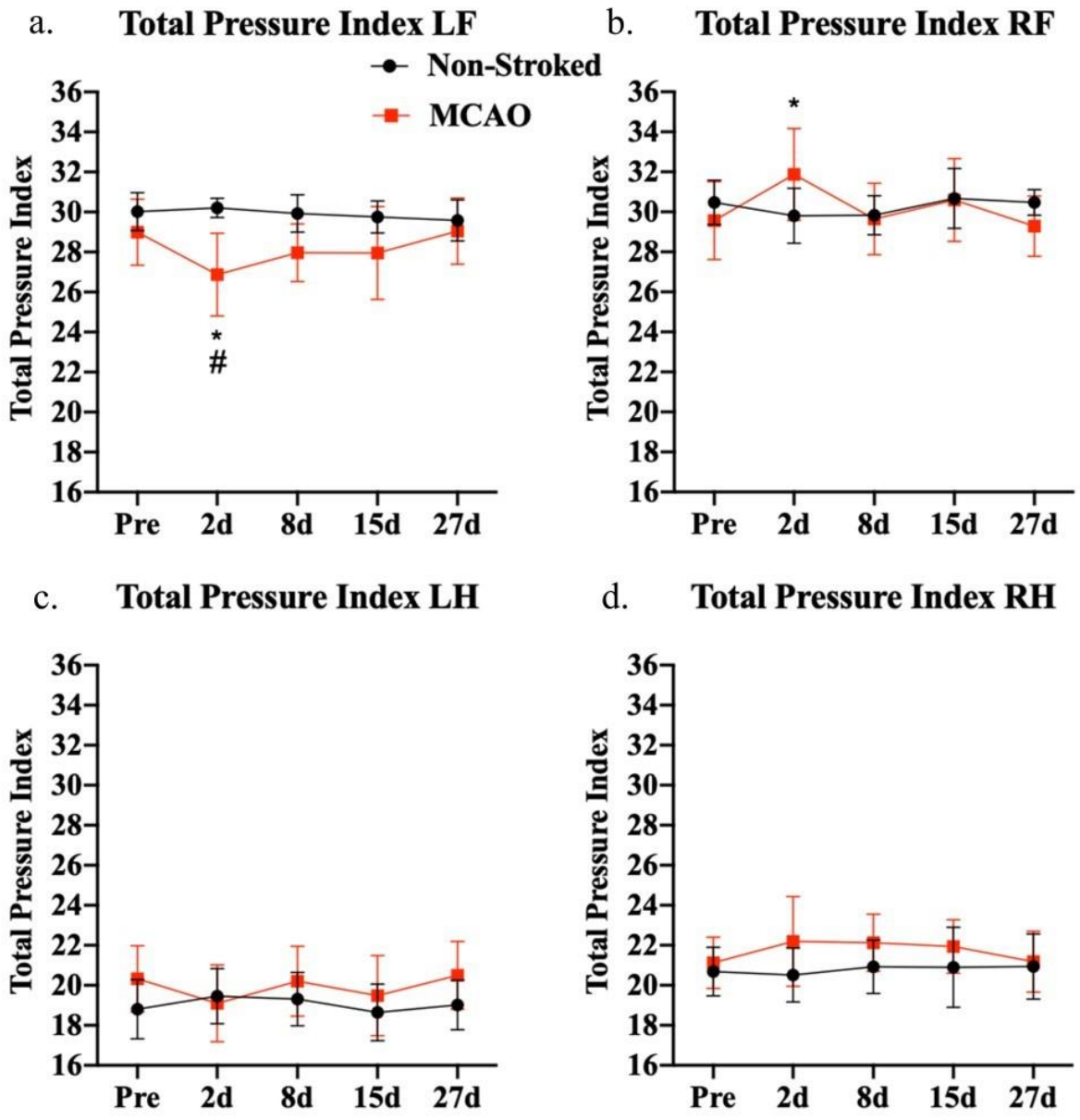

Supplementary Figure 4.5: MCAO induced limb weakness as measured by total pressure index. Total pressure index in the left front (LF) decreased compared to pre-MCAO and was significantly different than non-stroked controls at 2d post-MCAO (**a**). Total pressure index in the right front (RF) correspondingly increased at 2d post-MCAO compared to pre-MCAO (**b**) indicating weight and strength compensation. Hind limbs did not display any

significant observed weight distribution abnormalities (**c**, **d**). * indicated statistical difference from pre-MCAO values. # indicated statistical difference between groups. Page Break

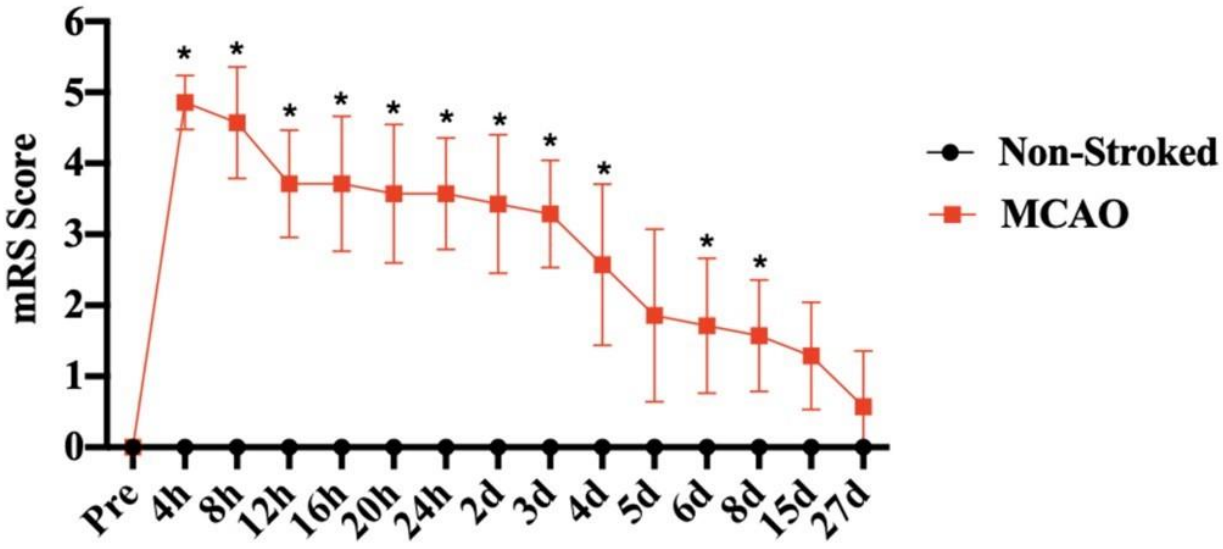

Supplementary Figure 4.6: Modified Rankin Scale score quantified behavioral deficits induced by stroke. Modified Rankin Scale (mRS) score is highest in the acute phase and statistically ($p<0.05$) different than pre-MCAO values through 8d post-MCAO. * indicated statistical difference from pre-MCAO values.

References

1 Spellicy, S. E. *et al.* Neural Stem Cell Extracellular Vesicles Disrupt Midline Shift Predictive Outcomes in Porcine Ischemic Stroke Model. *Transl Stroke Res*, doi:10.1007/s12975-019-00753-4 (2019).

CHAPTER 5

CONCLUSIONS AND FUTURE DIRECTIONS

5.1 IMAGING FLOW CYTOMETRY ELUCIDATED EV UPTAKE KINETICS AND SPECIFICITY

An imaging flow cytometry based platform was developed and optimized to characterize *in vitro* extracellular vesicle uptake. Despite their immense therapeutic potential as delivery vectors, quantifiable evidence for EV uptake is insufficient. Commonly, confocal microscopy has been utilized to evaluate *in vitro* uptake, but this technique is limited due to its low throughput, semi-quantitative nature, in addition to the need for high magnification or technical expertise [1–4]. We optimized the ImageStream^{x} Mark II, imaging flow cytometer, to quantitatively evaluate dose, time and specificity variables of HEK293T EVs. Imaging flow cytometry (IFC) combines individual cell information provided by standard microscopy through high resolution digital images of every cell with the statistical significance and quantifiable properties of standard flow cytometry [3–7]. We showed that EV uptake is an active dose and time dependent process. Furthermore, we assessed the selective uptake hypothesis showing that HEK293T EVs are taken up at higher quantities by HEK293T cells than other cell types. We found that neural stem cells internalized significantly more HEK293T EVs relative to mature neurons, suggesting that stem or progenitor cells may have higher rates of active EV internalization. This is especially encouraging for the study of CNS diseases. Chapter 2 supports the EV selectivity

hypothesis and provides a standardized platform to measure uptake characteristics to enhance translational efficacy of EVs.

The objective of this study was to assess the hypothesis that EVs display inherent tropism to cells of similar origin, where HEK293T EVs are specifically internalized by HEK293T cells [8–12]. Due to a lack of viable platforms to reproducibly quantify EV uptake and failed attempts using confocal and spatial light interference microscopy, IFC appeared to be most advantageous due to its high-throughput nature while providing qualitative images with quantifiable data [4]. An initial step in developing this platform was to verify that EVs were internalized by the recipient cells and not attached to the surface. Firstly, to suspend the cells, we used trypsin which has been shown to cleave off surface attached EVs [13]. Additionally, we created two inhibitory assays to assess if EVs are internalized via active processes. We showed that both a cold atmospheric environment and fixing the cells prior to EV co-culture, both decreased fluorescence on recipient cells, suggesting that the platform assessed internalized, not surface bound EVs Another obstacle was the auto-fluorescence of certain recipient cells. Since low fluorescence is emitted by the eGFP-EVs, laser powers had to be higher than standard flow cytometry. Therefore, we utilized numerous controls and developed a ratio of EV co-culture / control cells to compare the recipient cell types. Looking ahead, optimization of laser strength or further advancements of the IFC wizards would aid in mitigating these factors.

HEK293T EVs were selected due to their common use as EV delivery vectors, low *in vivo* toxicity, and their ability to be genetically modified to generate green fluorescent protein positive, GFP, EVs [14,15]. To advance the study's findings, the assays could be replicated using other common EV donor cell lines including neural stem cells, human mesenchymal stem cells, dendritic cells, U87 cancer cells, or others [8,16–19]. Another opportunity to further evaluate the

specificity hypothesis would be to select a wider range of recipient cells. Most comprehensive studies support the notion of EV specificity due to tetraspanins, heat shock proteins or other integrins on the EV surface [20–23]. However, there are discrepancies where uptake relates to the phagocytic or non-phagocytic activity of recipient cell [24]. In a microscopy assay, EVs were internalized more efficiently by phagocytes like macrophages and monocytes as compared to non-phagocytic cells including 293T cells [24]. Contrary to evidence found in literature, there was minimal EV uptake into HEK293T cells [15,24]. Thus, by inhibiting endocytosis with Dynamin or Heparan, and phagocytosis with Wortmannin, the mechanisms of EV uptake in each cell type could be quantified [13]. By using a variety of EV sources and recipient cell lines, we can further assess the specificity hypothesis *in vitro*. Blocking specific recipient cell receptors or tetraspanins relevant to EV interactions including Tspan8 with antibody blockers would elucidate the biological mechanisms of EV specificity [20]. *In vivo* biodistribution assays would provide more clarity on the specificity hypothesis in the future, but since biodistribution has been shown to be affected by dose and administration technique [8], a standardized system must be in place before providing conclusions.

Building upon our findings, an obvious utility of the IFC platform is to assess EV engineering and delivery of therapeutic cargo like fluorescently labelled siRNA, ASOs, and therapeutic peptides [25–27]. Comparing uptake kinetics and efficiency between EV mediated delivery and naked therapeutics in disease relevant cells like primary cells or patient derived induced pluripotent stem cell will provide quantifiable justification for harnessing EVs as a delivery vector. Commonly, EVs have been engineered with targeting ligands including rabies viral glycoprotein with LAMP2B, a common EV marker, and GE11 peptide to platelet derived growth factor [26,28]. We could further assess the engineering applicability and targeting

efficiencies of these targeting ligands in an *in vitro* controlled study. Similarly, CD47, the colloquial 'don't eat me signal' which has been engineered onto the EVs to avoid phagocytic breakdown, could be engineered into HEK293T cells to assess phagocytic uptake or potential alterations in endocytic uptake of EVs [29]. The development of this platform can be utilized in all EV targeting studies as a controlled *in vitro* study prior to *in vivo* modeling.

After the publication of this study, the ISx has been upgraded to include a 'high gain mode' that can more accurately quantify nanoparticles including EVs in the 100nm range [30]. This permits future users to quantify the percentage of fluorescent EVs used, but also in loading assays to better characterize amount of EVs containing the fluorescently tagged molecules (See Chapter 3). Although spot count provided a novel parameter to quantify EV uptake, the algorithm could be further trained and improved. Further, using high gain mode quantifications, EV fluorescence of one EV can be manually correlated to the fluorescence outputs of each spot in future uptake assays and later interpolated to quantify number of EVs per spot. Ultimately, IFC can be used across EV subtypes and recipient cells with wide ranging fluorescent molecules to advance the field of EV therapeutics.

With the 12-channel laser system, EV localization after internalization in recipient cells could be further assessed. EVs are mostly internalized by endocytosis and are therefore initially trapped in the endosomal system or shuttled to the lysosome [13,23,31,32]. In order to be therapeutically active, EV cargo must escape the endosome to reach its desired intracellular target (i.e. cytoplasm for siRNA) [33]. By administering GFP or dyed EVs to cells with a nuclei stain like DAPI or Hoechst and the lysosome, we could develop a high-throughput protocol using the localization features on IFC to image and quantify EV localization at various times points. Developing compensation matrices that account for spectral spillover between laser

activations and optimization of laser power due to the low fluorescence emission by the CD63-eGFP EVs is considered a challenge in this model. This understanding will potentially increase the fields knowledge of EV fate and provide a basis to possibly engineer and enhanced endosomal escape mechanism.

In Chapter 2, we transfected HEK293T donor cells with a CD63-eGFP plasmids to generate a fluorescent EV sample. In future studies, to standardize the fluorescent EV population, a lenti-viral stable cell line would provide more consistency fluorescent EV populations. Though fluorescently tagging CD63 is often used for EV uptake [8,13,34,35], there may be some confounding variables when using GFP. GFP is a large protein of 28kDa in weight that may affect EV uptake [36]. By transfecting additional CD63 into parent cells increasing CD63 on the EV surface may also impact cellular targeting [37]. In a recent study, it was shown transfecting HEK293T cells with CD63-GFP plasmids resulted in between 15-60 GFP molecules per EV [38]. Though no effects were reported in EV size and little noticeable differences in fluorescence intensity, the variable amounts GFP molecules may be a confounding variable. Moreover, our fluorescent population was limited to CD63 EVs which does not account for the entire heterogenous EV sample. Using a general EV membrane labelling like fluorescent proteins fused to farnesylation or palmitoylation signals may be preferred [39,40]. Other fluorescent alternatives have their own downfalls, where dyes like DiI and CFSE can alter the lipid profile of EVs form micelles leading to inaccurate concentration readings, or result in false positives due to the extended half-life of the dye [13,34,39]. In addition to tracking fluorescent EVs, we could also track labeled EV content. For instance, we could also label the endogenous RNA or protein in the EVs with the commercial product, ExoGlow to better track EV contents rather than a tagged protein or dyed lipid layer. Ultimately, CD63-eGFP was our optimal choice, but it would be

possible to transfect the N-Terminus of Lamp2B or the luminal side of CD63, CD81, or CD9 with other fluorophores like GFP or an mCherry [33]. By tagging the interior of the EV, we would limit interference on the external side to alter possible EV to cell interactions.

Chapter 2 advanced the field of EV biology by supporting the selective EV uptake hypothesis with HEK293T EVs and cells, and importantly standardized a high throughput platform that can help accelerate future development of EVs as therapeutics and drug delivery vectors.

5.2 EV-MEDIATED DELIVERY OF STAPLED PEPTIDES ENHANCED PEPTIDE UPTAKE AND DISRUPTION OF THE LRRK2-FADD INTERACTION OF PARKINSON'S DISEASE

Further investigation of the utility of extracellular vesicles is outlined in Chapter 3. We harnessed the inherent characteristics of HEK293T extracellular vesicles to enhance the delivery and translatability of a protein-protein inhibitor stapled peptide. To our knowledge, we are the first group to successfully load functional peptides into EVs to boost peptide serum stability, increase cellular uptake, and ultimately improve peptide efficacy by decreasing the required dose. To assess the efficacy of EVs as a delivery vector, we initiated a collaboration to deliver stapled peptides to disrupt the overactivated extrinsic death pathway caused by the G2019S missense mutation in the Leucine Rich Repeat Kinase 2 (LRRK2) gene, the most common genetic cause of Parkinson's Disease [41,42].

Our collaborators have identified the armadillo region of LRRK2 as the main binding site to FADD which in turn recruits and activates Caspase-8 leading to apoptotic neuronal cell death [43]. Co-expression of fragments of LRRK2 that contain the FADD binding motif or deletion of this motif block the interaction with FADD have shown to be neuroprotective [43]. In this study, we developed a peptide inhibitor (FARM5) that interrupted the FADD interaction with the

ARMadillo region of LRRK2 which leads to a downregulation of apoptotic signaling, while preserving the natural functions of LRRK2. However, peptide inhibitors have poor cellular penetrance or internalization and may still be susceptible to proteolytic breakdown [44,45]. Thus, we aimed to utilize the body's natural delivery messenger, extracellular vesicles to mitigate the challenges of peptide delivery and uptake. In Chapter 3, we optimized a high-throughput, passive, and scalable loading method of peptide into HEK293T EVs, enhanced peptide internalization into three separate cells lines as assessed using imaging flow cytometry platform developed in Chapter 2 and disrupted the LRRK2-FADD binding with low doses of peptide when delivered with HEK293T EVs. Though these results are encouraging, there remain opportunities to optimize our loading platform and efficiency, diversify the EV sources to include therapeutic EVs, and further assess the therapeutic efficacy in LRRK2 linked Parkinson's Disease preclinical models.

Our initial aim was to develop standardized and reproducible protocols for scalable, efficient, and passive EV loading to enhance the cellular internalization of the therapeutic peptides. Similar to previous chapter, we chose HEK293T EVs because of their frequent use in EV delivery studies [28,46–48], ability to be genetically modified, high production efficiency, and low reported toxicity [49]. Looking ahead, we could replicate our protocols with EVs that possess innate therapeutic or targeting characteristics including neural stem cell, mesenchymal stem cell or brain endothelial cell EVs, among others [18,19,50–52]. For example, in previous reports, we have shown that hNSC EVs decrease ischemic stroke related effects and are inflammatory modulators [18,19]. Furthermore, we could engineer our EVs with targeting ligands including the Rabies Viral Glycoprotein bound to LAMP2B, a common EV tetraspanin, to specifically target neurons [26,48].

Using these EVs as a delivery vector could then provide a synergistic effect as a multifaceted approach to treat LRRK2 linked Parkinson's Disease.

As noted in Chapter 3, the loading efficiencies of FARM5 peptides were around 5-20% efficient. This loading efficiency was based on the number of molecules inputted and compared to an interpolated value based on a standard curve of known concentrations of fluorescent peptides, based on previous reports [27]. Slightly higher than molecules of siRNA loaded per EV [27,53], we showed around 4,000-6,000 molecules of peptide per loaded EV. Our initial challenge was utilizing various concentrations of isolated EVs compared to a standardized manufacturing process. The inconsistent initial concentration of EVs resulted in non-reproducible results. We assayed multiple EV concentrations while maintaining a standard peptide concentration and found higher concentrations of EVs resulted in higher loading efficiencies with concentration $2*10^{10}$ EVs/mL as the ideal concentration. This was based off of the plateau effect of EV uptake seen in Chapter 2, where EV uptake becomes saturated around 10,000 EVs / cell.

To further increase loading efficiency in a high-throughput manner, there are multiple techniques we could apply. To advance passive association or loading with EVs, modification of the hydrophobicity of the peptide itself by tagging cholesterol or alpha-tocopherol would be a viable and seemingly straightforward. Increasing the hydrophobicity with cholesterol would enhance the membrane association as documented with cholesterol tagged siRNA as a passive and scalable method to enhance EV loading [27,51,55]. Though one drawback is that the peptides may be on the external leaflet of EV membrane [27] and further assays would to assess the protective efficacy should be pursued. Other loading options including electroporation, sonication, and even chemical transfection of the isolated EVs could be an explored path [25,26,56]. However, electroporation may result to false positive efficiencies due to siRNA aggregate

formation and disruption of the EV membrane or transfection in altered EV characteristics [56,57]. Lastly, the CP05 peptide, previously developed to anchor with CD63, could be synthesized to link with the FARM5 peptide [58]. The CP05-FARM5 conjugate mixed with EVs could result in a highly scalable and increasingly efficient association with the EV membrane. Despite attempts to increase efficiency, other challenges may persist that EVs become saturated with exogenous peptide and may increase in size or lose their intrinsic functionality. These methods may only become necessary if the downstream assays require larger concentrations of peptide in our EV samples. As seen in Chapter 3, the low concentration of peptide delivered by EVs is acceptable.

Another technical aspect to improve is the post-loading sample cleanup, in order to efficiently separate EV loaded peptides from naked peptides. We utilized ultracentrifugation as it has been the most prevalently cited method to separate free from loaded siRNAs or ASOs [26,27,51,59]. The rationale for ultracentrifugation is that EVs with higher molecular weight will pellet and free peptide remains in the supernatant [27]. There are pitfalls with this approach, most notably that UC may disrupt the EV membranes, result in EV loss, or isolate a subset of small EVs rather than the initial EV population [60,61]. In preliminary non-published data, we observed around 20% of EV retention after UC, but this should be replicated for all samples. Looking ahead, characterization of EVs via nanotracking software after loading and ultracentrifugation would provide more clarity on technical effects and possible EV loss during the loading procedures. However, even with post loading characterization, novel methods need to be explored to differentiate potential peptide/EV aggregation from loaded EVs. In preliminary studies, we have observed that UC separation of free peptide and loaded peptide can result in false positive data when the supernatant is not fully removed from the pellet. An alternative approach could be to utilize a technique similar to our ultrafiltration EV isolation using Amicon

filters [18,19], but with .5mL round filters. The smaller round filters are more suitable as a pellet can form in the center to decrease EV loss. Despite our reproducible outcomes in loading peptides into HEK293T EVs, the techniques above may aid in large scale manufacturing to maintain a high loading efficiency with a clean sample preparation for *in vivo* administration.

Though the loading and uptake assays provide optimism on the utility of EVs, additional *in vitro* assays to further analyze the protective capacity of EVs is a serum stability assay. The naked FARM5 peptide, though stapled, may still be susceptible to proteolytic breakdown [45]. A serum stability assay where co-culturing of naked and EV loaded peptide in mouse serum, assessed by mass spectrometry over time would elucidate the protective capacity of the HEK293T EVs [62]. We could also test the zeta-potential of the EV membrane before and after loading to assess if the loaded peptide is inside the lumen of the EV or attached to its surface [27]. Ultimately, the serum assay and zeta potential analysis would be highly translatable to an *in vivo* application of EV delivery.

Our primary endpoint was the disruption of the LRRK2-FADD binding via a co-immunoprecipitation assay. Though there is extensive literature supporting that overexpression of mutant LRRK2 increases the binding of FADD and increases apoptotic cell death, our study did not assess cell death in HEK293T cells [43,63,64]. The transfected HEK293T cells replicate the overexpression of G2019S LRRK2 and the overexpression of binding to FADD, but cell death was not assessed as they reportedly do not exhibit apoptotic cell death. Looking ahead, primary cortical neurons or a human iPS DA neuron model derived from control subjects or carriers of the G2019S-LRRK2 mutation [43,65] could be used. Similarly, dopaminergic neurons could be identified by immunofluorescence using MAP2, microtubule associated protein two, or Tuj1, class three beta-tubulin, antibodies, together with Tyrosine Hydroxylase or Vesicular

Monoamine transporter antibodies. In these assays, apoptotic cell death can be quantified through apoptotic phenotypes of nuclei and general cell viability assays [43]. Further, we could stain for active caspases involved in apoptosis or conduct immunoblotting to quantify their activation [43,66]. Another feasible *in vitro* assay to evaluate the intrinsic kinase activity of LRRK2, would be to purify over expressed Flag-tagged WT or G2019S mutant LRRK2 on Flag-coated ELISA plates [66]. From there, we could conduct an in-well *in vitro* kinase reaction using NICtide as a phosho-substrate [43,66].

To fully display the efficacy of EV delivery, *in vivo* modeling would be optimal. Our collaborators have identified an *in vivo* viral model of mutant LRRK2-PD that exhibits dopaminergic neuron loss [64]. After proof of principle *in vitro* studies, loaded EVs could be administered to the PD model mice intravenously, intranasally, or even intrastriatally. *In vivo*, outcome measures could include EV biodistribution, behavioral assays including open field tests, phenotypic assessments of dopaminergic neurons, inflammatory markers like GFAP, Iba-1, and even LRRK2 activation [67].

Ultimately, our study is the first to load functional peptides into EVs to increase peptide uptake into recipient cells and enhance its efficacy to decelerate the loss of neurons in LRRK2 Mutated Parkinson's Disease. Chapter 3 provides a foundation of scalable EV loading, two platforms to assess loading, a high-throughput quantitative method to measure EV uptake, and early evidence of enhanced therapeutic efficacy to disrupt the LRRK-2 FADD binding pathway in Parkinson's Disease.

5.3 LESION TOPOLOGY IN THE PORCINE BRAIN PROVIDES ALTERNATIVE BIOMARKER TO PREDICT STROKE OUTCOMES

In Chapters 2-3, preclinical *in vitro* assays were performed to assess the basic biology and translational potential of extracellular vesicles. In Chapter 4, the overall aim was to identify key structures lesioned by a middle cerebral artery occlusion (MCAO) and to evaluate the predictive capacity of neuroimaging techniques that characterize stroke outcomes in a translational porcine model. The further characterization of the porcine stroke model, specifically the understanding of lesion topology and its relation to functional outcome, provides an *in vivo* model with non-invasive biomarkers to assess therapeutic modalities including extracellular vesicles.

Previously our group has completed studies utilizing the permanent middle cerebral artery occlusion (MCAO) porcine stroke model [18,50]; Chapter 4 is the first study identifying lesion location to enhance our understanding of stroke etiology and possible recovery. Similar to previous studies, clinically relevant MRI measures showed significant lesion volumes, midline shifts, and decreased white matter integrity post-MCAO [18,50]. Through the optimization of a pig brain atlas, damaged brain structures included the insular cortex, somatosensory cortices, temporal gyri, claustrum, and visual cortices, among others. The lesioned MCAO territory in the pig model was anatomically similar to human ischemic stroke patients and resulted in comparable functional outcomes, supporting the pig as a robust ischemic stroke model. MCAO resulted in impaired gait parameters, decreased voluntary movement in open field testing, and poor modified Rankin Scale scores at acute timepoints with recovery after Day 8. Using a Pearson correlation analysis with a false discovery rate test at acute timepoints, we demonstrated that lesioning in specific brain structures had moderate-to-strong relationships with motor

function impairments as compared to commonly assessed clinical MRI stroke metrics at acute timepoints. For instance, an increased percentage of the globus pallidus lesioned strongly correlated with decreased gait measures at two and eight days post stroke. This correlation analysis approach helped characterize neuroanatomical structures predictive of stroke outcomes and may lead to the translation of this topological analysis approach from preclinical stroke assessment to a clinical biomarker. To our knowledge, we are the first group to characterize lesion topology and to explore the correlation of lesion location to functional outcomes in a porcine ischemic stroke model.

Since this study was exploratory in nature, our statistical analysis and main conclusions were limited due to a small sample size. The small sample size was a result of experimental constraints and confounding variables of porcine infection. By increasing our sample size, we could conduct a deeper statistical analysis based on the retrospective clinical models. However, human clinical studies are advantageous by being retrospective with hundreds of clinical patient data points [68,69]. To start, we could strengthen our system by at least increasing our sample to 12 pigs, which would allow stepwise regression analyzing up to 11 brain regions and thus would provide statistical support for which brain region has the highest impact on functional outcomes [70]. Though importantly, brain regions do not function in isolation and confounding variables still remain to be a challenge. Another option is to perform a classification and regression tree that could repeatedly split the sample into two sub-samples more homogenous with a defined outcome [69]. Ultimately, our statistical methods were sufficient and provide value to the field to begin to understand stroke etiology on a lesion location premise.

Often clinical studies assessing the predictive nature of lesion topology only compare against one output measure like the Rankin Score or the NIH Stroke Scale [71–74]. Initially we

attempted to conduct correlations across all functional measures, but this was not optimal due to the potential of false positive outcomes. This technique would be valid for an exceptionally large sample size of human patients, but not possible for a characterization study in the porcine model. We created a modified Rankin scale in a previous study [18], however the sensitivity of this model was also insufficient for the porcine model. Generating a sensitive gait score by combining the various spatiotemporal and pressure measures could be a novel translation outcome more closely relatable with human literature.

In our exploratory study, we successfully characterized lesion location, but were limited to the sensitivity of the brain atlas. We successfully identified approximately 50% of the lesion but were limited by the atlas. Our brain atlas, developed in 2010, was based on ex-vivo imaging and histological measures [75]. Similar to human studies, registration of larger structures revealed an acceptable level of atlas registration accuracy, with decreases in the registration of smaller structures like the contralateral ventricle. The atlas was originally developed using a healthy porcine brain, but in the injury model, ischemic swelling and midline shift may have contributed to alterations in the analytical plane. When compared with human literature, voxel based mapping approaches provide more resolution and detailed delineation between specific neuroanatomical regions, but are still imperfect [71]. Similarly, progress in rodent literature has been made by developing an enhanced framework to correct for edema in evaluating lesion size to improve atlas registration [76]. Thus, a follow-up study of healthy and MCAO pigs to improve the porcine brain atlas with higher resolution could be relevant, though we are confident with the existing model.

The MRI analysis and brain atlas that was used in Chapter 4 primarily focuses on large grey matter structures affected by the MCAO lesion. Although identification of lesioned

structures is beneficial and correlative to functional outcomes, further progress could be made by assessing structural connectivity [77,78]. In numerous retrospective human clinical papers, voxel-based lesion symptom mapping and classification and regression tree approaches revealed areas with high influence on higher modified Rankin Scale in regions involving the corona radiata, internal capsule, insular cortex, uncinate fasciculus, parietal lobe, among others [6971]. Additionally, disruptions in the white matter tracts descending from primary motor cortex and dorsal premotor cortex have been implicated in stroke recovery in humans [79]. Similarly, in a non-human primate study, functional changes correlated with behavioral outcomes involving sensorimotor cortices that were not restricted to the affected hemisphere [80]. In our model, diffusion tensor images with fractional anisotropy would allow for the depiction of white matter tracts, specifically the corona-radiata or fibers from the cortico-spinal tract, to gain a deeper picture of global lesion effects. As done by collaborators, tractography would also provide more information on white matter connections, structure, and function in both control and lesioned pigs. However, the images from the coil used in this study did not provide enough resolution to do so. Thus, improving the accuracy of the atlas with the inclusion of white matter structures could strengthen future studies and improve the influence of lesion location on functional outcomes.

An ideal study merging the premise of EV uptake specificity in Chapter 2 and the advancements of Chapter 4, would be to assess EV biodistribution in the porcine brain. EVs can be loaded with superparamagnetic iron oxide (SPIO) nanoparticles to create magneto EVs that can be tracked via magnetic resonance imaging [81,82]. Though not yet standardized, loading can occur by adding the SPIO to parent cells or directly electroporating isolated EVs [83]. SPIO EVs could be visualized on the T2-weighted imaging of a healthy and stroked porcine brain and

matched to the brain atlas allowing us to assess EV biodistribution in the brain based on dose, administration method, administration location, EV subtype, and even possibly engineered EVs with targeting peptides, similar to that in rodent studies [8]. Although this process would require significant standardization in our hands, it would provide valuable *in vivo* data regarding EV tropism and selectivity to brain regions and to the lesion site in a stroke model.

Preclinical models often report traditional MRI metrics like lesion volume to predict functional outcomes. Using stroke volume can Increase the frequency of the identifying stroke lesion topology to correlate to functional outcomes in preclinical animal models. The ability to predict injury volumes, lesion regions, and functional outcomes increases the translational benefit of this model. In the future, using this characterized model and analytical framework would allow us to better assess therapeutic modalities including extracellular vesicles. Though we have shown that EVs are neuroprotective in a porcine stroke model [18,50], we could better understand the EV targeting efficiency to specific neuronal cells and structures and further understand the underlying neuroanatomical effects preserved by extracellular vesicles.

Chapter 4 supports the premise of including lesion topology in acute MRI assessments in to improve preclinical predictive capacity and to advance translatability of stroke therapeutics.

5.4 REFERENCES

1. Ofir-Birin, Y. *et al.* Monitoring extracellular vesicle cargo active uptake by imaging flow cytometry. *Front. Immunol.* **9**, 1011 (2018).
2. Franzen, C. A. *et al.* Characterization of uptake and internalization of exosomes by bladder cancer cells. *Biomed Res. Int.* **2014**, (2014).
3. Mastoridis, S. *et al.* Multiparametric analysis of circulating exosomes and other small extracellular vesicles by advanced imaging flow cytometry. *Front. Immunol.* **9**, 1583 (2018).
4. Lannigan, J. & Erdbruegger, U. Imaging flow cytometry for the characterization of extracellular vesicles. *Methods* **112**, 55–67 (2017).
5. Görgens, A. *et al.* Optimisation of imaging flow cytometry for the analysis of single extracellular vesicles by using fluorescence-tagged vesicles as biological reference material. *J. Extracell. Vesicles* **8**, (2019).
6. Ricklefs, F. L. *et al.* Imaging flow cytometry facilitates multiparametric characterization of extracellular vesicles in malignant brain tumours. *J. Extracell. Vesicles* **8**, (2019).
7. Tertel, T. *et al.* <scp>High-Resolution</scp> Imaging Flow Cytometry Reveals Impact of Incubation Temperature on Labeling of Extracellular Vesicles with Antibodies. *Cytom. Part A* cyto.a.24034 (2020) doi:10.1002/cyto.a.24034.
8. Wiklander, O. P. B. *et al.* Extracellular vesicle in vivo biodistribution is determined by cell source, route of administration and targeting. *J. Extracell. vesicles* **4**, 26316 (2015).
9. Smyth, T. *et al.* Biodistribution and delivery efficiency of unmodified tumor-derived exosomes. *J. Control. Release* **199**, 145–55 (2015).
10. Kim, S. M. *et al.* Cancer-derived exosomes as a delivery platform of CRISPR/Cas9 confer

cancer cell tropism-dependent targeting. *J. Control. Release* **266**, 8–16 (2017).

11. Sancho-Albero, M. *et al.* Exosome origin determines cell targeting and the transfer of therapeutic nanoparticles towards target cells. *J. Nanobiotechnology* **17**, 16 (2019).
12. Sancho-Albero, M., Ana Medel-MartínezMartínez ac, ab & MartínMartín-Duque, P. Use of exosomes as vectors to carry advanced therapies. (2020) doi:10.1038/s41929-019-0333-4.
13. Mulcahy, L. A. *et al.* Routes and mechanisms of extracellular vesicle uptake. *J. Extracell. Vesicles* **3**, (2014).
14. Zhu, X. *et al.* Comprehensive toxicity and immunogenicity studies reveal minimal effects in mice following sustained dosing of extracellular vesicles derived from HEK293T cells. *J. Extracell. Vesicles* **6**, 1324730 (2017).
15. Lamichhane, T. N. & Jay, S. M. Production of extracellular vesicles loaded with therapeutic cargo. *Methods Mol. Biol.* **1831**, 37–47 (2018).
16. Zhu, L. *et al.* Targeting and Therapy of Glioblastoma in a Mouse Model Using Exosomes Derived From Natural Killer Cells. *Front. Immunol.* **9**, 824 (2018).
17. Katakowski, M. *et al.* Exosomes from marrow stromal cells expressing miR-146b inhibit glioma growth. *Cancer Lett.* **335**, 201–204 (2013).
18. Webb, R. L. *et al.* Human Neural Stem Cell Extracellular Vesicles Improve Recovery in a Porcine Model of Ischemic Stroke. *Stroke* **49**, 00–00 (2018).
19. Webb, R. L. *et al.* Human Neural Stem Cell Extracellular Vesicles Improve Tissue and Functional Recovery in the Murine Thromboembolic Stroke Model. *Transl. Stroke Res.* **9**, 530–539 (2018).
20. Rana, S. & Zoller, M. The functional importance of tetraspanins in exosomes. in

Emerging Concepts of Tumor Exosome-Mediated Cell-Cell Communication 69–91 (Springer New York, 2013). doi:10.1007/978-1-4614-3697-3_4.

21. Nazarenko, I. *et al.* Cell Surface Tetraspanin Tspan8 Contributes to Molecular Pathways of Exosome-Induced Endothelial Cell Activation. *Cancer Res.* **70**, 1668–1678 (2010).
22. Svensson, K. J. *et al.* Exosome Uptake Depends on ERK1/2-Heat Shock Protein 27 Signaling and Lipid Raft-mediated Endocytosis Negatively Regulated by Caveolin-1 * □ S. (2013) doi:10.1074/jbc.M112.445403.
23. Horibe, S., Tanahashi, T., Kawauchi, S., Murakami, Y. & Rikitake, Y. Mechanism of recipient cell-dependent differences in exosome uptake. *BMC Cancer* **18**, 47 (2018).
24. Feng, D. *et al.* Cellular internalization of exosomes occurs through phagocytosis. *Traffic* **11**, 675–687 (2010).
25. Usman, W. M. *et al.* Efficient RNA drug delivery using red blood cell extracellular vesicles. *Nat. Commun.* **9**, 2359 (2018).
26. Alvarez-Erviti, L. *et al.* Delivery of siRNA to the mouse brain by systemic injection of targeted exosomes. *Nat. Biotechnol.* **29**, 341–345 (2011).
27. Didiot, M. C. *et al.* Exosome-mediated delivery of hydrophobically modified siRNA for huntingtin mRNA silencing. *Mol. Ther.* **24**, 1836–1847 (2016).
28. Ohno, S. I. *et al.* Systemically injected exosomes targeted to EGFR deliver antitumor microrna to breast cancer cells. *Mol. Ther.* **21**, 185–191 (2013).
29. You, B., Xu, W. & Zhang, B. Engineering exosomes: a new direction for anticancer treatment. *Am. J. Cancer Res.* **8**, 1332–1342 (2018).
30. Pugsley, H. R., García-mendoza, M. G. & Davidson, B. R. High Gain Mode for Increased Sensitivity in the Detection of Small Particles. *Appl. Note* 1–5 (2020).

31. McKelvey, K. J., Powell, K. L., Ashton, A. W., Morris, J. M. & McCracken, S. A. Exosomes: Mechanisms of Uptake. *J. Circ. biomarkers* **4**, 7 (2015).

32. Delenclos, M. *et al.* Investigation of Endocytic Pathways for the Internalization of Exosome-Associated Oligomeric Alpha-Synuclein. *Front. Neurosci.* **11**, 172 (2017).

33. Joshi, B. S., de Beer, M. A., Giepmans, B. N. G. & Zuhorn, I. S. Endocytosis of Extracellular Vesicles and Release of Their Cargo from Endosomes. *ACS Nano* **14**, 4444–4455 (2020).

34. Russell, A. E. *et al.* Biological membranes in EV biogenesis, stability, uptake, and cargo transfer: an ISEV position paper arising from the ISEV membranes and EVs workshop. in *Journal of Extracellular Vesicles* vol. 8 1684862 (2019).

35. Wiklander, O. P. B. *et al.* Systematic methodological evaluation of a multiplex bead-based flow cytometry assay for detection of extracellular vesicle surface signatures. *Front. Immunol.* **9**, 1326 (2018).

36. Hink, M. A. *et al.* Structural dynamics of green fluorescent protein alone and fused with a single chain Fv protein. *J. Biol. Chem.* **275**, 17556–17560 (2000).

37. Rana, S., Yue, S., Stadel, D. & Zöller, M. Toward tailored exosomes: The exosomal tetraspanin web contributes to target cell selection. *Int. J. Biochem. Cell Biol.* **44**, 1574–1584 (2012).

38. Corso, G. *et al.* Systematic characterization of extracellular vesicles sorting domains and quantification at the single molecule–single vesicle level by fluorescence correlation spectroscopy and single particle imaging. *J. Extracell. Vesicles* **8**, (2019).

39. Lai, C. P. *et al.* Visualization and tracking of tumour extracellular vesicle delivery and RNA translation using multiplexed reporters. *Nat. Commun.* **6**, (2015).

40. Gabrielli, M. *et al.* Active endocannabinoids are secreted on extracellular membrane vesicles. *EMBO Rep.* **16**, 213–220 (2015).

41. Rideout, H. J. & Stefanis, L. The neurobiology of LRRK2 and its role in the pathogenesis of Parkinson's disease. *Neurochemical Research* vol. 39 576–592 (2014).

42. Rui, Q., Ni, H., Li, D., Gao, R. & Chen, G. The Role of LRRK2 in Neurodegeneration of Parkinson Disease. *Curr. Neuropharmacol.* **16**, 1348–1357 (2018).

43. Antoniou, N. *et al.* A motif within the armadillo repeat of Parkinson's-linked LRRK2 interacts with FADD to hijack the extrinsic death pathway. *Sci. Rep.* **8**, 1–17 (2018).

44. Ali, A. M., Atmaj, J., Van Oosterwijk, N., Groves, M. R. & Dömling, A. Stapled Peptides Inhibitors: A New Window for Target Drug Discovery. *Computational and Structural Biotechnology Journal* vol. 17 263–281 (2019).

45. Bruno, B. J., Miller, G. D. & Lim, C. S. Basics and recent advances in peptide and protein drug delivery. *Therapeutic Delivery* vol. 4 1443–1467 (2013).

46. Bai, J. *et al.* Engineered targeting tLyp-1 exosomes as gene therapy vectors for efficient delivery of siRNA into lung cancer cells. *Asian J. Pharm. Sci.* (2019) doi:10.1016/j.ajps.2019.04.002.

47. Faruqu, F. N., Xu, L. & Al-Jamal, K. T. Preparation of exosomes for siRNA delivery to cancer cells. *J. Vis. Exp.* **2018**, 58814 (2018).

48. Liu, Y. *et al.* Targeted exosome-mediated delivery of opioid receptor Mu siRNA for the treatment of morphine relapse. *Sci. Rep.* **5**, 17543 (2015).

49. Massaro, C. *et al.* Extracellular vesicle-based nucleic acid delivery: Current advances and future perspectives in cancer therapeutic strategies. *Pharmaceutics* vol. 12 1–19 (2020).

50. Spellicy, S. E. *et al.* Neural Stem Cell Extracellular Vesicles Disrupt Midline Shift

Predictive Outcomes in Porcine Ischemic Stroke Model. *Transl. Stroke Res.* (2019) doi:10.1007/s12975-019-00753-4.

51. Biscans, A. *et al.* Hydrophobicity of Lipid-Conjugated siRNAs Predicts Productive Loading to Small Extracellular Vesicles. *Mol. Ther.* **26**, 1520–1528 (2018).

52. Yang, T. *et al.* Delivery of Small Interfering RNA to Inhibit Vascular Endothelial Growth Factor in Zebrafish Using Natural Brain Endothelia Cell-Secreted Exosome Nanovesicles for the Treatment of Brain Cancer. *AAPS J.* **19**, 475–486 (2017).

53. Haraszti, R., Coles, A., Aronin, N., Khvorova, A. & Didiot, M.-C. Loading of Extracellular Vesicles with Chemically Stabilized Hydrophobic siRNAs for the Treatment of Disease in the Central Nervous System. *BIO-PROTOCOL* **7**, (2017).

54. Chu, Q. *et al.* Towards understanding cell penetration by stapled peptides. *Medchemcomm* **6**, 111–119 (2015).

55. Osborn, M. *et al.* Hydrophobicity drives the systemic distribution of lipid-conjugated siRNAs via lipid transport pathways. *bioRxiv* 288092 (2018) doi:10.1101/288092.

56. Shtam, T. A. *et al.* Exosomes are natural carriers of exogenous siRNA to human cells in vitro. *Cell Commun. Signal.* **11**, 88 (2013).

57. Kooijmans, S. A. A. *et al.* Electroporation-induced siRNA precipitation obscures the efficiency of siRNA loading into extracellular vesicles. *J. Control. Release* **172**, 229–238 (2013).

58. Gao, X. *et al.* Anchor peptide captures, targets, and loads exosomes of diverse origins for diagnostics and therapy. *Sci. Transl. Med.* **10**, 195 (2018).

59. Haraszti, R. A. *et al.* Optimized Cholesterol-siRNA Chemistry Improves Productive Loading onto Extracellular Vesicles. *Mol. Ther.* **26**, 1973–1982 (2018).

60. Bobrie, A., Colombo, M., Krumeich, S., Raposo, G. & Théry, C. Diverse subpopulations of vesicles secreted by different intracellular mechanisms are present in exosome preparations obtained by differential ultracentrifugation. *J. Extracell. Vesicles* **1**, (2012).

61. Konoshenko, M. Y., Lekchnov, E. A., Vlassov, A. V & Laktionov, P. P. Isolation of Extracellular Vesicles: General Methodologies and Latest Trends. (2018) doi:10.1155/2018/8545347.

62. Hanold, L. E. *et al.* Design of a selenylsulfide-bridged EGFR dimerization arm mimic. *Bioorganic Med. Chem.* **23**, 2761–2766 (2015).

63. Melachroinou, K. *et al.* Elevated In Vitro Kinase Activity in Peripheral Blood Mononuclear Cells of Leucine-Rich Repeat Kinase 2 G2019S Carriers: A Novel Enzyme-Linked Immunosorbent Assay–Based Method. *Mov. Disord.* **35**, 2095–2100 (2020).

64. Nguyen, A. P. T. *et al.* Dopaminergic neurodegeneration induced by Parkinson's disease-linked G2019S LRRK2 is dependent on kinase and GTPase activity. *Proc. Natl. Acad. Sci. U. S. A.* **117**, 17296–17307 (2020).

65. Kouroupi, G. *et al.* Defective synaptic connectivity and axonal neuropathology in a human iPSC-based model of familial Parkinson's disease. doi:10.1073/pnas.1617259114.

66. Melachroinou, K. *et al.* Activation of FADD-Dependent neuronal death pathways as a predictor of pathogenicity for LRRK2 mutations. *PLoS One* **11**, e0166053 (2016).

67. Lai, C. P. *et al.* Dynamic biodistribution of extracellular vesicles in vivo using a multimodal imaging reporter. *ACS Nano* **8**, 483–494 (2014).

68. Cheng, B. *et al.* Influence of stroke infarct location on functional outcome measured by the modified rankin scale. *Stroke* **45**, 1695–1702 (2014).

69. Yassi, N. *et al.* The association between lesion location and functional outcome after

ischemic stroke. *Int. J. Stroke* **10**, 1270–1276 (2015).

70. Timpone, V. M. *et al.* Percentage insula ribbon infarction of>50% identifies patients likely to have poor clinical outcome despite small dwi infarct volume. *Am. J. Neuroradiol.* **36**, 40–45 (2015).

71. Cheng, B. Influence of Stroke Infarct Location on Functional Outcome Measured by the Modified Rankin Scale. *Stroke* **44**, 1695–1702 (2013).

72. Lin, C., Chatterjee, N., Lee, J., Harvey, R. & Prabhakaran, S. Predictive value of the combination of lesion location and volume of ischemic infarction with rehabilitation outcomes. *Neuroradiology* **61**, 1131–1136 (2019).

73. Ernst, M. *et al.* Association of Computed Tomography Ischemic Lesion Location with Functional Outcome in Acute Large Vessel Occlusion Ischemic Stroke. *Stroke* **48**, 2426–2433 (2017).

74. Payabvash, S., Taleb, S., Benson, J. C. & McKinney, A. M. Acute ischemic stroke infarct topology: Association with lesion volume and severity of symptoms at admission and discharge. in *American Journal of Neuroradiology* vol. 38 58–63 (2017).

75. Saikali, S. *et al.* A three-dimensional digital segmented and deformable brain atlas of the domestic pig. *J. Neurosci. Methods* **192**, 102–109 (2010).

76. Koch, S. *et al.* Atlas registration for edema-corrected MRI lesion volume in mouse stroke models. doi:10.1177/0271678X17726635.

77. Ktena, S. I. *et al.* Brain connectivity measures improve modeling of functional outcome after acute ischemic stroke. *Stroke* **50**, 2761–2767 (2019).

78. Etherton, M. R. *et al.* Integrity of normal-appearing white matter and functional outcomes after acute ischemic stroke. 1701–1708 (2017) doi:10.1212/WNL.0000000000003890.

79. Riley, J. D. *et al.* Anatomy of stroke injury predicts gains from therapy. *Stroke* **42**, 421–426 (2011).

80. Hernandez-Castillo, C. R. *et al.* Increased functional connectivity after stroke correlates with behavioral scores in non-human primate model OPEN. (2017) doi:10.1038/s41598-017-07175-y.

81. Chuo, S. T.-Y., Chien, J. C.-Y. & Lai, C. P.-K. Imaging extracellular vesicles: current and emerging methods. *J. Biomed. Sci.* **25**, 91 (2018).

82. Tada, Y. & C. Yang, P. Iron Oxide Labeling and Tracking of Extracellular Vesicles. *Magnetochemistry* **5**, 60 (2019).

83. Hu, L., Wickline, S. A. & Hood, J. L. Magnetic resonance imaging of melanoma exosomes in lymph nodes. *Magn. Reson. Med.* **74**, 266–271 (2015).